A UNIFIED CONSTITUTIVE MATERIAL MODEL WITH APPLICATION TO MACHINING

A Thesis
Presented to
The Academic Faculty

by

Rui Liu

In Partial Fulfillment
of the Requirements for the Degree
Doctor of Philosophy in the
George W. Woodruff School of Mechanical Engineering

Georgia Institute of Technology
December 2014

A UNIFIED CONSTITUTIVE MATERIAL MODEL WITH APPLICATION TO MACHINING

Approved by:

Dr. Shreyes Melkote, Advisor
School of Mechanical Engineering
Georgia Institute of Technology

Dr. Steven Danyluk
School of Mechanical Engineering
Georgia Institute of Technology

Dr. Richard Neu
School of Mechanical Engineering
Georgia Institute of Technology

Dr. Naresh Thadhani
School of Materials Science & Engineering
Georgia Institute of Technology

Dr. Roshan Vengazhiyil
School of Industrial & System Engineering
Georgia Institute of Technology

Date Approved: November 17, 2014

This thesis is dedicated to

My parents

My wife

For their love, endless support and encouragement

ACKNOWLEDGEMENTS

I would like to express the deepest appreciation to my advisor, Dr. Shreyes Melkote, for his continuous mentorship, encouragement, and support during these four years, which I will cherish in the years to come. I am confident that everything I have learnt from him will serve me well in the future. I would also like to extend my sincere appreciation to Dr. Steven Danyluk, Dr. Naresh Thadhani, Dr. Richard Neu and Dr. Roshan Vengazhiyil, for serving on my disseration committee and providing valuable feedback on my work.

I want to acknowledge my former office mate and friend, Dr. Meisam Salahshoor, for his help, guidance and his notable contributions to my research work. I will never forget the days when we worked together.

Friends are an extremely important part of my life. My special thanks go to my best friends, Dr. Xi Liu, Dr. Lei Ma, Dr. Hao Wu, Dr. George Mathai and Dr. Buddhika Jayasena for being there when I needed a hand. I find myself lucky to have them as friends in my life.

My appreciation also goes to all the members of Prof. Melkote's group in the PMRC, Lejun Cen, Andrea Marcon, Arkadeep Kumar, Craig Woodin, and Pushparghya Kuila. In particular, I want to thank Patxi Fernandez-Zelaia for generating the experimental data for my thesis work.

I am grateful to Third Wave Systems LLC for providing the financial and technical support. I would also like to thank Dr. Raghuram Pucha and John Morehouse for their assistance.

Finally, I would like to give my appreciation to the people who mean the whole world to me, namely my parents and my wife. I hereby dedicate this thesis to them for their love and endless support.

TABLE OF CONTENTS

CHAPTER

LIST OF TABLES

LIST OF FIGURES

Page

LIST OF SYMBOLS AND ABBREVIATIONS

A	Hardening parameter (m^{-1})
$\bar{A}$	Material constant (MPa)
Al	Aluminum
a	Material constant of shear modulus (GPa)
B	Recovery parameter
$\bar{B}$	Material constant (MPa)
$\bar{B}_0$	Material constant (MPa)
b	Magnitude of the Burgers vector (m)
bcc	Body centered cubic
$\bar{C}$	Material constant
CA	Cellular Automaton
CDRX	Continuous Dynamic Recrystallization
CP	Commercially pure
CRSS	Critical Resolved Shear Stress
Cu	Copper
C_z	Fitting parameter of final recrystallized grain size
D	Grain size (μm)
D_f	Final recrystallized grain size (μm)
D_{IHPE}	Critical grain size for initiating the IHPE (μm)
D_o	Initial grain size (μm)
$\bar{D}$	Material constant
DRV	Dynamic Recovery
DRX	Dynamic Recrystallization

d	Parameter controlling the critical grain size of IHPE
E	Young's modulus (GPa)
ECAP	Equal Channel Angular Pressing
ET	Estrin-Tóth
f	Shear band frequency (kHz)
FEM	Finite Element Method
F_c	Cutting force (N)
F_t	Thrust force (N)
fcc	Face centered cubic
G_0	Total free energy necessary to overcome the obstacle
GDRX	Geometric Dynamic Recrystallization
g_o	Normalized activation energy at 0 K (μm)
H	Hardening
$\overline{H}$	Material constant
HAB	High angle boundary
HPE	Hall-Petch Effect
hcp	Hexagonal close packed
IHPE	Inverse Hall-Petch Effect
ISV	Internal State Variable
JC	Johnson-Cook
K	Proportionality parameter defining the saturation stress level (m^{-1})
K_{IC}	Toughness
$\overline{K}$	Material constant (MPa)
KM	Kocks-Mecking
k	Boltzmann’s constant ($J \cdot K^{-1}$)

k_d	Fitting parameter of d (K^{-1})
k_v	Fitting parameter of v (K^{-1})
L	Length of cut (mm)
$\bar{l}$	Critical distance representing the spacing of grain boundary carbides
LAB	Low Angle Boundary
MTS	Mechanical Threshold Stress
m	Fitting parameter of final recrystallized grain size
$\bar{m}$	Material constant
$\bar{n}$	Material constant
OFHC	Oxygen-free high thermal conductivity
PSZ	Primary Shear Zone
p	Parameter defining the shape of energy barriers associated with short range obstacles
$\bar{p}$	Hydrostatic pressure
Q	Activation energy for lattice self-diffusion ($kJ \cdot mol^{-1}$)
q	Parameter defining the shape of energy barriers associated with short range obstacles
R	Gas constant ($\mu m^{-0.5}$)
$\bar{r}$	Material constant
S	Parameter inversely proportional to the average grain size (μm^{--1})
S_1	Peak thickness of segmented chip (μm)
S_2	Valley thickness of segmented chip (μm)
S_3	Banding distance of segmented chip (μm)
$\bar{S}$	Material constant
SHPB	Split Hopkinson Pressure Bar
SS	Stainless steel

SSZ	Secondary Shear Zone
T	Temperature (K)
Ti	Titanium
$T_{melting}$	Melting temperature (K)
T_{room}	Room temperature (K)
T_r	Material constant of shear modulus (K)
t_u	Cutting feed (mm)
u	Fitting parameter controlling the DRX rate
V	Vanadium
v	Parameter controlling the softening rate of IHPE
v_c	Cutting speed (m·min^{-1})
Z	Zener-Hollomon parameter (s^{-1})
ZA	Zerilli-Armstrong
α	Rake angle (˚)
α_o	Numerical constant of order unity
α_d	Dislocation (viscous) drag coefficient (kPa·s)
α_G	Parameter related to the strength of dislocation-grain boundary interaction
α_ρ	Parameter related to the strength of dislocation-dislocation forest interaction
$\bar{\alpha}_0$	Material constant
$\bar{\alpha}_1$	Material constant
β	Coefficient of friction
$\bar{\beta}_0$	Material constant
$\bar{\beta}_1$	Material constant
γ	Shear strain
ε	Strain

ε_f	Strain value at which dynamic recrystallization effect saturates
ε_r	Critical strain at which DRX occurs
$d\bar{\varepsilon}$	Equivalent plastic strain rate
$\Delta\bar{\varepsilon}$	Increment of equivalent plastic strain during an integration cycle
$\bar{\varepsilon}_0$	Material constant
$\bar{\varepsilon}^f$	Equivalent strain to fracture
$\bar{\varepsilon}_f$	Critical plastic strain
$\dot{\varepsilon}$	Strain rate (s^{-1})
$\dot{\varepsilon}_o$	Reference strain rate (s^{-1})
κ_G	Hall-Petch constant ($MPa \cdot \mu m^{0.5}$)
μ	Shear modulus (GPa)
μ_o	Shear modulus at 0 K (GPa)
v	Poisson's ratio
ρ	Dislocation density (m^{-2})
$\rho_{H\&DRV}$	Intermediate dislocation density determined by the competing dislocation production and annihilation processes (m^{-2})
ρ_m	Material density ($kg \cdot m^{-3}$)
ρ_o	Initial dislocation density (m^{-2})
ρ_R	Dislocation density with fully recrystallized grain structure (m^{-2})
$\Delta\rho_{DRX}$	DRX-induced change in dislocation density (m^{-2})
σ	Flow stress (MPa)
$\sigma*$	Principal stress (MPa)
σ_o	Stress required to overcome short range obstacles at 0 K (MPa)
σ_a	Athermal component of flow stress (MPa)
σ_d	Dislocation drag component of flow stress (MPa)

σ_G	Stress required to overcome far-field strain field of grain boundaries (MPa)
σ_ρ	Stress required to overcome far-field strain field of dislocation forests (MPa)
σ_{th}	Thermal component of flow stress (MPa)
$\bar{\sigma}$	Effective Mises stress (MPa)
$\bar{\sigma}_0$	Material constant (MPa)
$\bar{\sigma}_a$	Material constant (MPa)
$\bar{\sigma}_S$	Material constant (MPa)
$\bar{\sigma}_f$	Critical stress (MPa)
$\hat{\sigma}$	Mechanical threshold stress (MPa)
$\hat{\sigma}_a$	Parameter characterizing the rate independent interactions of dislocations with long-range barriers such as grain boundaries at 0 K (MPa)
ϕ	Shear plane angle (˚)

SUMMARY

Finite element simulation of metal cutting processes offers a cost-effective method to optimize the cutting conditions and to select the right tool material and geometry. A key input to such simulations is a constitutive model that describes material behavior during severe plastic deformation. However, the vast majority of material models used in prior work are phenomenological in nature and are usually obtained by fitting a non-physically based mathematical equation to the macro-scale stress-strain response of the material. Moreover, the deformation range covered by the stress-strain response used in the model calibration process usually falls short of the ranges typically observed in metal cutting.

This thesis seeks to develop a unified material model that explicitly incorporates microstructure evolution into the constitutive law to describe the macro-scale plastic deformation response of the material valid over the range of strains, strain rates and temperatures experienced in machining. The proposed unified model is based on the underlying physics of interactions of mobile dislocations with different short and long range barriers and accounts for various physical mechanisms such as dynamic recovery and dynamic recrystallization. In addition, the inclusion of microstructure evolution into the constitutive model enables the prediction of microstructure in the chip and the machined surface. In this study, the unified material model is calibrated and validated in the severe plastic deformation regime characteristic of metal machining and is then implemented in finite element simulations to evaluate its ability to predict continuous and segmented chip formation in machining of pure metals such as OHFC copper and commercially-pure titanium (CP-Ti).

Due to the physical basis of the proposed unified material model, the continuous chip formation observed in orthogonal cutting of OFHC copper is shown to be successfully predicted by the finite element model utilizing a version of the unified material model that explicitly accounts for microstructure evolution as well as dislocation drag as a plausible deformation mechanism applicable at the high strain rates common in metal cutting operations. The segmented or shear localized chip formation in orthogonal cutting of CP-Ti is also shown to be successfully simulated by the unified model after incorporating the inverse Hall-Petch effect arising from the ultrafine grain structure within the shear band. For both metals, the model is experimentally validated using flow stress data as well as machining data including cutting and thrust forces and relevant chip morphology parameters. Machining simulations carried out using the unified material model also yield useful insights into the microstructure evolution during the machining process, which is shown to be consistent with the available experimental data and the known physical understanding of severe plastic deformation behavior of the metals.

CHAPTER 1

INTRODUCTION

1.1 Motivation and Problem Statement

Numerical modeling and simulation of machining is a very effective approach for gaining fundamental insight into the complex material behavior during the metal cutting process and for optimizing the cutting conditions and tool geometry without performing costly experiments. Due to the complexity of the machining process, a reliable numerical modeling and simulation approach needs to consider all aspects including material deformation behavior, contact friction, heat generation and transfer. The development of a constitutive material model that accurately describes the deformation behavior of the material during machining is the main research focus of this thesis.

The constitutive material model provides a mathematical description of how the material responds to various strains, strain rates and temperatures under different deformation conditions. Most of the earlier constitutive models used to describe the material plastic stress-strain response in machining macroscopically describe the flow stress as a phenomenological function of strain, strain rate and temperature. A good example of such a material model is the Johnson-Cook (JC) flow stress model [1]. In the last few decades, more and more physical mechanisms have been taken into consideration in developing constitutive models, such as the Zerilli-Armstrong (ZA) model [2] and the Nemat-Nasser model [3].

Although refined constitutive models increasingly tend to be established on physical foundations, they continue to rely on phenomenological relationships to describe various aspects of the stress-strain response of the material. These models are often calibrated using stress-strain data over a limited range of strains, strain rates, and temperatures and cannot accurately describe the flow stress response of the material when extrapolated to a deformation regime that goes beyond the model calibration regime. Considering that a metallic workpiece material experiences severe plastic deformation in a very short time interval during machining, and is characterized by strains (>> 1) and strain rates (10^4~10^6 s^{-1}) that are well beyond the conditions that established dynamic compression (e.g. Split Hopkinson Pressure Bar) tests can achieve, extrapolation of the calibrated constitutive model is unavoidable. Therefore, in order to improve the accuracy of machining simulations, a material model that explicitly accounts for more of the underlying micro-scale physical mechanisms responsible for the observed macro-scale deformation behavior is required.

An aspect of machining process modeling and simulation that has received limited attention over the years is prediction of the microstructure in the machined chip and workpiece surface. Traditional finite element modeling of machining operations is often limited to simulation of the machining forces, temperatures, strain distributions, etc. [4]. However, eventually, it is the microstructure (e.g. grain size) of the machined part that is of interest since it determines the functional properties of the surface. Consequently, an important motivation of this thesis is to investigate the development of a constitutive material model for machining that explicitly (and in a unified manner) accounts for microstructure evolution due to various micro-scale physical mechanisms active during plastic deformation and their effect on the flow stress. In doing so, the model will enable simulation of the resulting microstructure in the machined chip and workpiece surface. While such unified constitutive models have been reported in the literature for simple plastic deformation processes (e.g. uniaxial compression/tension), their development and use in severe plastic deformation processes such as machining are very limited.

Another aspect of finite element modeling of the machining process that has received limited attention in the literature is the extent of model validation. For instance, prior machining process models have largely focused on prediction of the cutting forces and paid limited attention to quantitative validation of the resulting chip morphology. Due to the different properties of the workpiece material under different cutting conditions, the chip formed could be continuous or segmented. Several constitutive models have been shown to successfully predict continuous chip formation in machining. For instance, the JC model was used by Guo [5] to characterize the mechanical behavior of 6061-T6 aluminum during machining. However, the actual mechanisms for segmented chip formation have not been fully understood so far.

For materials with low thermal conductivity such as Ti-6Al-4V, material removal is characterized by a chip with alternating regions of high and low strains (segmented chip with shear bands). Since the strain rates in machining are generally very high (10^4~10^6 s^{-1}), the time available for thermal diffusion is very short. When the latter is coupled with low thermal conductivity of the work material, the heat generated by plastic deformation accumulates in the primary shear zone leading to shear localization or shear banding and chip segmentation. Chip segmentation is undesirable because it can cause large variations in the cutting force and associated vibration that can severely inhibit tool life and yield poor dimensional accuracy of the machined part feature. Consequently, it is critical that the unified material model be able to accurately predict the onset of shear localization and chip segmentation in machining of such metals and permit the investigation of material microstructure in and around the shear bands.

1.2 Research Goals and Objectives

In light of the problems and motivations discussed in the previous section, the goal of this thesis is to develop a physics-based unified constitutive material model that is applicable in the severe plastic deformation regime characteristic of machining and accurately describes the flow stress of the material in terms of the strengthening and/or softening effects that arise from the evolution of internal microstructure parameters, i.e. grain size and dislocation density, during deformation.

The model developed in the thesis incorporates the effects of common material strengthening and/or softening mechanisms such as work hardening, dynamic recovery (DRV), and dynamic recrystallization (DRX). Additional deformation mechanisms such as dislocation drag (active at high strain rates) and strain softening due to the inverse Hall-Petch effect are considered in the model to permit accurate prediction of the machining response for certain metals. These physical mechanisms not only increase the fidelity of model extrapolations for the machining application but also enhance our understanding of the underlying cutting mechanics at the microstructure level.

In addition, the explicit incorporation of a microstructure evolution law into the constitutive model enables seamless assessment of microstructure evolution in machining and to eventually predict the mechanical properties of the product without performing costly experimental studies.

In combination with the finite element method, the developed unified model is used to simulate the machining of single phase ductile metals that are characterized by continuous and segmented chip formation. In order to investigate the performance of the developed unified model in simulating continuous chip formation in orthogonal cutting of a ductile metal (e.g. OFHC Copper), the predicted cutting and thrust forces, and the strain, strain rate, and temperature distributions, and microstructure evolution in the machined chip are evaluated and compared against orthogonal cutting data.

Segmented chip formation in metals such as commercially-pure titanium (CP-Ti) is often attributed to the low thermal conductivity of the material. The modeling of segmented chip formation remains a challenge due to limited understanding of the responsible micro-scale mechanisms in the constitutive description of the material behavior. This thesis investigates the modeling and simulation of segmented chip formation via the developed unified model. The contributions of the different microstructure mechanisms to the material response under different cutting conditions are also analyzed.

The research objectives of this thesis can be summarized as follows:

1. Develop, calibrate, and validate a unified constitutive material model for plastic flow valid in the severe plastic deformation regime characteristic of metal machining.
2. Implement the unified model in a finite element model of orthogonal cutting to simulate the cutting forces, chip morphology, and microstructure (e.g. grain size, dislocation density) of the machined chip and workpiece surface when cutting ductile metals such as OFHC Copper that yield a continuous chip.

3. Enhance the unified material model to capture segmented chip formation and shear localization in machining of low thermal conductivity metals such as commercially-pure titanium.

The research objectives of this thesis are accomplished through a comprehensive literature review of the prior work followed by scientific studies and rigorous analysis.

1.3 Thesis Outline

The following parts of this thesis are organized as follows:

Chapter 2 presents a comprehensive review of prior work relevant to this thesis.

Chapter 3 describes the effective deformation mechanisms considered in this study. The influence of each mechanism on the flow stress is modeled based on the interaction of dislocations with various short and long range barriers. The microstructure evolution laws for grain size and dislocation density are also integrated into the unified material model to describe microstructure evolution with plastic deformation. The calibration and validation procedures for the unified model are explained through application of the model to predict the flow stress curves for AISI 304 stainless steel.

Chapter 4 describes the implementation of the unified model in orthogonal cutting simulations to predict the cutting forces and the strain, strain rate, and temperature distributions along with microstructure evolution in a continuous chip formation process obtained when machining OFHC copper. The predicted results are compared with experimental data to evaluate the effectiveness of the calibrated unified model.

Chapter 5 presents an enhanced unified model that incorporates strain softening due to the inverse Hall-Petch effect in order to accurately simulate segmented chip formation and shear banding observed in machining of low thermal conductivity metals, such as commercially-pure titanium. The chapter also presents experimental validation of the enhanced model.

Chapter 6 includes the summary, major conclusions, and deficiencies of this work, and provides recommendations for potential future work.

CHAPTER 2

LITERATURE REVIEW

This chapter contains a review of prior work in the following areas relevant to the proposed research work: (1) phenomenological and physics-based constitutive models, (2) microstructure evolution, (3) dislocation drag, (4) inverse Hall-Petch effect (IHPE), (5) machining simulation, and (6) shear banding and chip segmentation.

2.1 Constitutive Models: Phenomenological vs. Physics-based

A classical tenet of materials science describes the inelastic behavior of materials as a collective effect of two mechanistic phenomena: dependence of flow stress on microstructure and evolution of microstructure with strain [6]. A constitutive description of inelastic behavior is considered to be phenomenological when the microstructure and its evolution are not included in modeling the observed flow stress-strain response. In contrast, a physics-based unified model considers the microstructure and describes the full strain-microstructure-flow stress relationship. As such, a physics-based unified model provides a mechanistic tool to analyze the observed inelastic behavior and understand the effects of the underlying micro-scale mechanisms. This fundamental understanding is the key to successfully designing and developing different metals and alloys for enhanced performance and manufacturability.

Phenomenological models are commonly represented by mathematical equations which are calibrated by a data fitting procedure and as such replicate the observed flow stress-strain behavior. Stout and Follansbee [7] applied four phenomenological models, as shown in Table 2.1, to describe the strain hardening behavior of 304L stainless steel (SS) and noticed that the accuracy of the strain hardening models depended on the strain range. The Voce law [8] was the most accurate at large strains ($\varepsilon > 0.40$), whereas the Swift [9] and Ludwik [10] laws were found to be the most accurate at small strains ($\varepsilon < 0.01$) in the vicinity of yield. The simple power law of Hollomon [11] for strain hardening was inadequate at all levels of strain. Moreover, the Voce model was the only one that was able to predict the saturation of work hardening. As a metal is deformed to large strains, it is expected that dynamic recovery will attenuate strain hardening and lead to saturation of the flow stress. Kocks [12] provided a physical foundation for saturation based on dislocation storage and dynamic recovery rates and postulated a work hardening law which is similar to that of Voce. The phenomenological models may even capture strain rate hardening and thermal softening; however, one cannot rely on these models outside their calibration range.

Table 2.1: Work hardening laws.*

Hollomon [11]	$\sigma = \bar{K}\varepsilon^{\bar{n}}$ (2.1)
Ludwik [10]	$\sigma = \bar{\sigma}_0 + \bar{K}\varepsilon^{\bar{n}}$ (2.2)
Swift [9]	$\sigma = \bar{K}(\varepsilon + \bar{\varepsilon}_0)^{\bar{n}}$ (2.3)
Voce [8]	$\sigma = \bar{\sigma}_s - (\bar{\sigma}_s - \bar{\sigma}_0)exp\left(\frac{\bar{K}\varepsilon}{\bar{\sigma}_s - \bar{\sigma}_0}\right)$ (2.4)

* In Table 2.1, σ is the flow stress, ε is the plastic strain, $\bar{K}$, $\bar{n}$, $\bar{\varepsilon}_0$, $\bar{\sigma}_0$ and $\bar{\sigma}_S$ are material constants.

The popular Johnson and Cook (JC) model [1] is an example of a widely used phenomenological model:

$$\sigma = (\bar{A} + \bar{B}\varepsilon^{\bar{n}})\left(1 + \bar{C}ln\frac{\dot{\varepsilon}}{\dot{\varepsilon}_0}\right)\left[1 - \left(\frac{T - T_{room}}{T_{melting} - T_{room}}\right)^{\bar{m}}\right] \tag{2.5}$$

where σ is the flow stress, ε is the plastic strain, $\dot{\varepsilon}$ is the plastic strain rate, $\dot{\varepsilon}_0$ is the reference plastic strain rate, T is the temperature, T_{room} and $T_{melting}$ are the room and melting temperatures, respectively, and $\bar{A}$, $\bar{B}$, $\bar{C}$, $\bar{m}$ and $\bar{n}$ are material constants.

Due to the very few parameters and its high efficiency and convenience in programming, the JC model is widely used. However, this model simply considers the strain hardening, strain-rate hardening and thermal softening factors in a multiplicative manner and does not account for possible higher order coupling of strain, strain-rate, and temperature. More importantly however, the JC model is heavily dependent on the experimental data used for calibration and consequently, there is no justification for relying on the model outside the calibration range.

Physics-based models for metals and alloys describe the constitutive behavior based on dislocation mechanics principles. In these models, the macro-scale flow stress depends on the density of mobile dislocations and their velocity. Johnston and Gilman [13] found that the dislocation velocity in a Lithium Fluoride (LiF) crystal depends on the applied stress and that the velocity or dynamic resistance to motion encountered by a moving glide dislocation is affected by temperature, impurities, and radiation damage. Using the Orowan equation and an experimentally-derived proportional relation between plastic strain and dislocation density, they calculated the dislocation velocity for a given plastic strain and strain rate. The dislocation velocity was then used to determine the flow stress from the relation between the dislocation velocity and flow stress, as a first physics-based attempt to describe the inelastic behavior of the material.

Following Johnston and Gilman, considerable research has been done to develop physics-based models. On the basis of experimental observations in pure mono- and polycrystals, Mecking and Kocks [6] found that the rate and thermal sensitivity of flow stress (or flow stress kinetics) as well as the strain hardening rate (or microstructure evolution rate) deviate from the Cottrell-Stokes law at large strains or high temperatures where dynamic recovery becomes significant. Subsequently, they proposed a phenomenological model by modifying the classical Arrhenius equation for glide kinetics using a factor of order unity, which decreases with increase in the dynamic recovery rate to quantitatively describe the observed departure from classical behavior. Estrin and Mecking [14] modified the Voce law and gave it physical significance by modeling the competition between dislocation accumulation and dynamic recovery. It was assumed that dislocations become immobilized and are stored after traveling a distance proportional to the average distance between dislocations.

Noticing that the strain rate and temperature dependences of flow stress are different in body centered cubic (bcc), face centered cubic (fcc), and hexagonal close packed (hcp) crystal structures, Zerilli and Armstrong [2, 15] proposed different dislocation-mechanics-based constitutive descriptions for the different material structures as follows:

$$\text{bcc:} \qquad \sigma = \bar{\sigma}_a + \bar{B} e^{-(\bar{\beta}_0 - \bar{\beta}_1 ln \dot{\varepsilon})T} + \bar{K} \varepsilon^{\bar{n}} \tag{2.6}$$

$$\text{fcc:} \qquad \sigma = \bar{\sigma}_a + \bar{B}_0 \varepsilon^{1/2} e^{-(\bar{\beta}_0 - \bar{\beta}_1 ln \dot{\varepsilon})T} \tag{2.7}$$

$$\text{hcp:} \qquad \sigma = \bar{\sigma}_a + \bar{B} e^{-(\bar{\beta}_0 - \bar{\beta}_1 ln \dot{\varepsilon})T} + \bar{B}_0 \varepsilon^{1/2} e^{-(\bar{\alpha}_0 - \bar{\alpha}_1 ln \dot{\varepsilon})T} \tag{2.8}$$

where σ is the flow stress, ε is the plastic strain, $\dot{\varepsilon}$ is the plastic strain rate, T is the temperature, $\bar{\sigma}_a$, $\bar{B}$, $\bar{B}_0$, $\bar{K}$, $\bar{n}$, $\bar{\alpha}_0$, $\bar{\alpha}_1$, $\bar{\beta}_0$ and $\bar{\beta}_1$ are material constants.

They also included dynamic recovery and subsequent saturation of the stress-strain curve at large strains [16]. However, Voyiadjis and Abed [17] pointed out that the ZA model is not valid at high strain rates and temperatures due to the approximation used in deriving the model. In the same study, Voyiadjis and Abed also developed similarly separate constitutive models for bcc and fcc metals using the concept of thermal activation energy and dislocation interaction mechanisms. Meyers et al. [18] also described the high strain rate deformation behavior of metals through physics-based mechanisms with thermal activation being central to the captured phenomena and effects.

Based on arguments that strain is not a valid state parameter and that the thermally activated interaction of dislocations with obstacles is governed by a rate controlling deformation mechanism only up to strain rates as high as 10^4 s^{-1} in fcc metals, Follansbee and Kocks [19] developed the Mechanical Threshold Stress (MTS) model as follows:

$$\sigma = \hat{\sigma}_a + (\hat{\sigma} - \hat{\sigma}_a)\left[1 - \left(\frac{kT}{g_0 \mu b^3} ln\left(\frac{\dot{\varepsilon}_0}{\dot{\varepsilon}}\right)\right)^{1/q}\right]^{1/p} \tag{2.9}$$

where σ is the flow stress, $\dot{\varepsilon}$ is the plastic strain rate, T is the temperature, k is the Boltzmann's constant, g_0 is the normalized activation energy at 0 K, μ is the shear modulus, b is the magnitude of the Burgers vector, $\dot{\varepsilon}_0$ is the reference strain rate, $\hat{\sigma}_a$ is the parameter characterizing the rate independent interactions of dislocations with long-range barriers such as grain boundaries at 0 K, and p and q are parameters defining the shape of energy barriers associated with short range obstacles. The MTS model used the mechanical threshold stress $\hat{\sigma}$ (or flow stress at 0 K) as an internal state variable (ISV) (or structure parameter) and extended the application of Kocks [12] and Mecking and Kocks [6] models to the high strain rate regime; however, in the Kocks-Mecking (KM) model, the average dislocation density ρ was considered as the structure parameter. These two internal state variables, ρ and $\hat{\sigma}$, and are equivalent since $\hat{\sigma}$ is a measure of the mechanical strength of obstacles to dislocations and is related to ρ via $\hat{\sigma} = \alpha_o \mu b \sqrt{\rho}$ where α_o is a numerical constant of order unity. As such, the constitutive (or kinetic) equation was written as an additive decomposition of athermal (interaction of dislocations with long range barriers) and thermal (interaction of dislocations with short range barriers) stress components and the evolution of the internal state variable was modeled using a physics-based expression for dynamic recovery and a phenomenological term for strain hardening.

To examine the applicability of the KM model (also called Mechanical Threshold Stress or MTS model) to more complex material systems such as alloys where strengthening is the result of multiple deformation mechanisms, Follansbee and Gray [20] applied the single parameter KM model to analyze the deformation behavior of Ti-6Al-4V alloy at low temperatures, and low and high strain rates. Here again, the mechanical threshold stress was used as an internal state variable and the effects of various strengthening mechanisms present in the alloy were captured as separate contributions to the mechanical threshold stress. In another instance, Follansbee et al. [21] used the MTS model to propose a lower-bound temperature and strain rate dependent constitutive model for AISI 304 stainless steel alloy. The lower-bound model predicted the maximum deformation anticipated for the lowest possible strength condition. Later, Follansbee [22] applied the MTS model to replicate the temperature and strain rate dependence of the yield stress of *annealed* austenitic stainless steel by defining two mechanical threshold stress terms representing the interactions of dislocations with nitrogen and other solute and interstitial atoms. A third MTS/ISV characterizing the evolving stored dislocation density was added subsequently to predict the entire stress-strain curve in the work hardened state. However, the MTS model tends to overlook those interactions which are not affected by thermal activation such as the interaction of dislocations with grain boundaries and forest dislocations.

Nemat-Nasser and Isaacs [23] described the flow stress of tantalum (a bcc polycrystal) and tantalum-tungsten alloys as the sum of athermal (σ_a) and thermally (σ_{th}) activated stress components based on dislocation kinematics and kinetics as follows:

$$\sigma = \sigma_a + \sigma_{th} = \bar{\sigma}_0 \varepsilon^{\bar{n}} + \hat{\sigma}\left[1 - \left(\frac{kT}{G_0} ln\left(\frac{\dot{\varepsilon}_0}{\dot{\varepsilon}}\right)\right)^{1/q}\right]^{1/p} \tag{2.10}$$

where $\bar{\sigma}_0$, $\bar{n}$ are constants, $\hat{\sigma}$ is the threshold stress due to the Peierls barrier to dislocation motion, and G_0 is the corresponding energy. The athermal component described the resistance to dislocation motion arising from long range, strain dependent barriers such as grain boundaries and far-field dislocation forests and was modeled by a phenomenological power law equation. The thermally activated component represents the resistance to dislocation motion from short range, temperature and strain rate dependent Peierls (lattice) barriers and was modeled using the phenomenological expression proposed by Kocks et al. [24]. Nemat-Nasser and Li [3] used a similar approach to model the flow stress of oxygen-free high thermal conductivity (OFHC) copper (an fcc polycrystal). Kocks [12], Estrin and Mecking [14], and Mecking and Kocks [6] considered the evolution of dislocation density due to hardening and dynamic recovery; however, the majority of previously mentioned models did not consider the evolution of microstructure features, such as the grain size, especially due to dynamic recrystallization.

2.2 Microstructure Evolution

Luton and Sellars [25] were among the first to include the effect of DRX on the flow stress. In their study, the flow stress of material after experiencing partial DRX was described as a combination of unrecrystallized and fully recrystallized flow stress components via the rule of mixtures and the volume fraction of recrystallized material. Later, Sah et al [26] modified their model to include the effect of different pre-strain values. However, both models gave only a phenomenological description of the effect of DRX on the flow stress and lacked a quantitative description of the underlying microstructure evolution. To address this shortcoming, Rollett et al. [27] and Peczak and Luton [28] employed the Monte Carlo method to describe the microstructure evolution during the DRX process. However, they were not able to capture grain growth kinetics during DRX due to limitations of the Monte Carlo method. Recently, a combination of the cellular automaton (CA) method and the KM model [6, 14] was used by Ding and Guo [29] and Yazdipour et al. [30] to simulate the microstructure evolution due to DRX and inelastic flow during thermomechanical processing. Although they were able to successfully predict the final microstructure and volume fraction of recrystallized material, the explicit formulation of a constitutive law in terms of microstructural ISVs was missing. Additionally, extensive use of their approach in practical applications is limited due to the complexity of the CA method. Despite all of the prior work, there is still a pressing need for a unified physics-based material model which explicitly integrates the microstructure evolution (particularly due to DRX) into the constitutive description of flow stress. The unified approach is expected to provide advantages with regard to the ease of physical interpretation for the model parameters and the ability to predict the evolution of microstructure with strain. The latter is imperative in predicting the material behavior throughout the stages of a thermomechanical deformation process.

Realizing this need, Hallberg et al. [31] proposed a constitutive law describing the flow stress as an explicit function of average dislocation density and grain size. Following the thermal activation energy theory for inelastic deformation, the flow stress was defined as the sum of thermal and athermal components. The thermal component represented only the Peierl’s stress needed to overcome lattice friction and was taken as a constant and equal to the virgin yield stress. The athermal component was formulated as a superposition of a grain size dependent term (Hall-Petch relation) and a dislocation density dependent term (Taylor’s equation [32]). The grain size evolution resulting from continuous dynamic recrystallization (CDRX) was modeled as a function of only inelastic strain as follows:

$$D = D_0 - \left(D_0 - D_f\right)\{1 - exp(-\bar{K}[\varepsilon - \bar{\varepsilon}_c]^{\bar{n}})\} \tag{2.11}$$

where D is the grain size, D_0 and D_f are the initial grain size and the saturation grain size, respectively, $\bar{\varepsilon}_c$ is the critical strain, $\bar{K}$ and n̄ are the parameters that define how fast the recrystallization proceeds with increasing plastic deformation. Based on this evolution law, CDRX cannot occur until a critical strain, $\bar{\varepsilon}_c$, is accumulated in the microstructure. Thereafter, the grain size exponentially decreases until a saturation level, D_f, is reached. The dislocation density evolution law was basically that of Estrin and Mecking [14] modified to include a grain size dependent term that captured the effect of CDRX on dislocation density.

Picu and Majorell [33] essentially used a similar formulation for athermal stress; however, due to the absence of dynamic recrystallization in their model the grain size did not evolve and was kept constant. A modified form of the Mecking and Kocks [6] model for the evolution of dislocation density was used to capture the effects of strain hardening and dynamic recovery. Fan and Yang [34] used the inverse stereological relation between the grain size and grain boundary area per unit volume to derive an evolution law for grain size. They also modified the Mecking and Kocks [6] evolution law for dislocation density so that it captured the effects of dynamic recrystallization on dislocation density evolution. However, their model produced a large error at room to moderate temperatures assuming the same critical resolved shear stress (CRSS) for all the slip systems, which is true at high temperatures, and characterizing the flow stress of a polycrystal using one CRSS.

Tóth et al [35] presented a model which was based on the presence of a cellular structure of dislocations as the fundamental microstructural feature. Cell walls and interiors were treated as separate hard and soft phases, respectively, forming together a composite two-phase structure. Dislocation densities in the cell walls and interior, cell size, and volume fraction of the cell walls were taken as evolving microstructure parameters with strain. The constitutive law was formulated as a combination of the contributions from the cell walls and interiors using the rule of mixtures. A power law type relation describing the flow stress as an explicit function of dislocation density was applied to describe each contribution. On limitations of the model, it was stated that “A tacit assumption in this model is the existence of an established dislocation cell structure. Strictly speaking, this means that this approach is only valid for dislocation cell forming materials which have already undergone a sufficient amount of straining for a cell structure to develop” [36]. Moreover, it was estimated that the temperature could rise up to 680 ~ 690 K due to adiabatic heat generation in dynamic loading of copper; however, the dynamic recrystallization possible at those temperatures was not accounted for in the model. Considering this dislocation structure as a precursor for developing grain structure, Estrin and Kim [37] traced the evolution of cell size in the Equal Channel Angular Pressing (ECAP) process to simulate the corresponding grain refinement.

2.3 Dislocation Drag

It is noted that, depending on the cutting speed, strain rates of up to 10^6/s can be generated in machining [38]. At such high deformation rates, an intensified strain rate sensitivity is often observed in the form of a sharp upturn in the flow stress versus strain rate plot, as shown in Figure 2.1. While an enhanced rate of accumulation of dislocations is reported [39, 40] as the primary microstructural cause for the increased strain rate sensitivity in the elbow region (10^3~10^4/s) in Figure 2.1, dislocation drag is considered as the plausible microstructural cause for the increased strain rate sensitivity at higher strain rates. Dislocations can experience a drag force due to their interaction with lattice phonons and electrons when moving in the crystal lattice. This drag force may become significant at large strain rates where dislocations need to move quickly to accommodate the macroscale inelastic deformation imposed on a metal. Follansbee and Weertman [41] estimated that the strain rate should be as high as 10^5/s to 10^6/s in a metal before dislocation drag can have a significant influence on the flow stress. The strain rate at which transition from thermal activation to drag-controlled deformation occurs is sensitive to the mobile dislocation density [42]. Nemat-Nasser and Guo [43] and Guo and Nemat-Nasser [44] included the effect of dislocation drag in their physics-based material model by adding a third term to the constitutive formulation derived from thermal activation theory in order to describe the high strain rate response of commercially pure vanadium and nitronic-50 stainless steel.

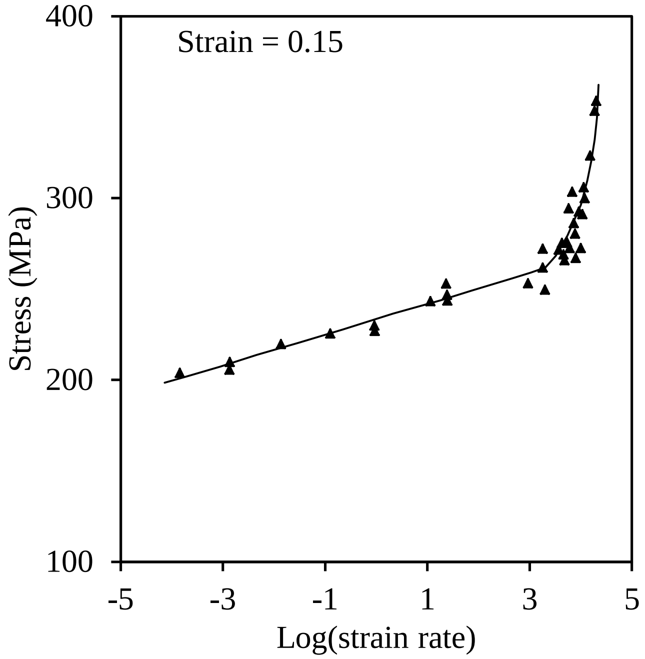

Figure 2.1: Strain rate sensitivity of OFHC Copper at room temperature and 15% strain [42].

Under the premise that the inclusion of dislocation drag in the constitutive law will yield a more accurate description of deformation physics prevalent in metal cutting, Wedberg and Svoboda [45] modified the Lindgren model [46] by adding an extra term representing the dislocation drag effect to the constitutive law derived from thermal activation theory and used the modified model to simulate orthogonal cutting of 316L stainless steel. However, it still demonstrated poor predictive capability when extrapolated to strain rates higher than those common in dynamic loading experiments such as split Hopkinson pressure bar (SHPB) test. This deficiency was attributed to the inability of the Lindgren model to capture strain softening due to dynamic recrystallization at large strains.

2.4 Inverse Hall-Petch Effect (IHPE)

Grain boundaries act as barriers to dislocation motion since the neighboring grains and the corresponding active slip planes have different crystallographic orientations. Therefore, dislocations cannot move easily from one grain to another. Instead, the dislocations pile up at grain boundaries and build up a driving force for the creation of a new dislocation source in the adjacent grain. Grain boundary strengthening is often described by the well-known Hall-Petch effect (HPE) [47, 48].

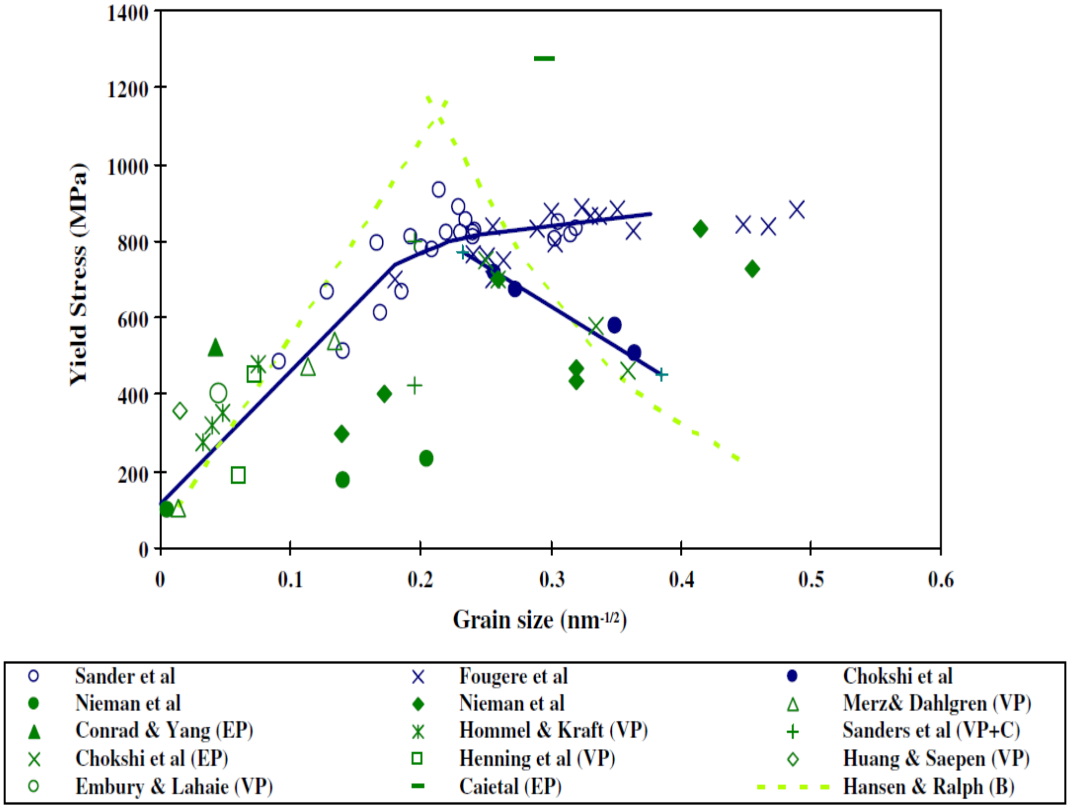

Figure 2.2: Compiled yield stress versus grain size plot for Cu from various sources ranging from coarse to nano-size grains. The plots show different trends as the grain size falls below a critical value [49].

As grains are refined progressively, the high strength normally expected by the HPE has been questioned by several investigations [50, 51], which claim that the material strength either remains constant or decreases with decreasing grain size below a critical value. The phenomenon is commonly referred to the inverse Hall-Petch effect (IHPE) (see Figure 2.2). Different physical explanations for the IHPE have been proposed as follows:

Dislocation based interpretation: Based on Li's study [52], Scattergood and Koch [53] combined the dislocation size-scale dependent dislocation line tension with dislocation-network strengthening [54] to obtain a theoretical description of the grain size softening transition observed in certain nanocrystalline materials. But based on the high resolution electron microscopic observations reported by Thomas et al. [55] and Wunderlich et al. [56], the presence of network dislocations within nano-size grains is questionable.

Triple junction disclination effect: In considering the correlation between the increasing triple junction volume and the material softening in crystalline materials reported by Rabukhin [57], Palumbo et al. [58] and Suryanarayana et al. [59] adopted this mechanism to interpret the IHPE. However, there is no detailed quantitative model developed for the triple junction disclination effect in these studies.

Diffusion creep: The phenomenon, which occurs by the transport of vacancies along the grain boundaries, termed Coble creep, has been used by Chokshi et al. [50] to explain the IHPE at room temperature using a simple phenomenological model. This model was improved by Masumura et al. [60] to extend its application scope to a wider range of grain sizes.

Grain boundary sliding: Rao et al.'s [61] experiments on Cr-Mn-N austenitic steel from 300 to 1300 K showed that the Hall-Petch relationship with a positive slope is valid up to 873 K. At higher temperatures (> 873 K), the slope becomes negative (see Figure 2.3), which indicates the inverse Hall-Petch effect. Chokshi et al. [50] attributed this phenomenon to the occurrence of grain boundary sliding at high temperatures. This mechanism was also adopted by Swygenhoven and Caro [62, 63] to simulate grain boundary sliding and motion, as well as grain rotation using a molecular dynamics computer simulation. However, their study lacks the simulation details and validation against experiment data. Also, there are many analytical models that use grain boundary sliding to interpret the IHPE, which have been documented by Hahn and Padmanabhan [64]. They proposed a phenomenological model to describe the IHPE as a competition between the grain boundary sliding controlled process and crystallographic slip dominated deformation. In this model, the grain size is the only variable, and the effects of strain rate and temperature on the IHPE have not been considered.

Two phase based model: In this method [65, 66], a crystalline material is modeled as two phases with different properties for the grain boundary region and the grain interior region, as shown in Figure 2.4. Different phases behave differently but their effects can be combined using the rule of mixtures. However, it is very challenging to accurately model the material behavior of the different phases. Therefore, although this model gives a more fundamental interpretation for the IHPE, it needs further investigation.

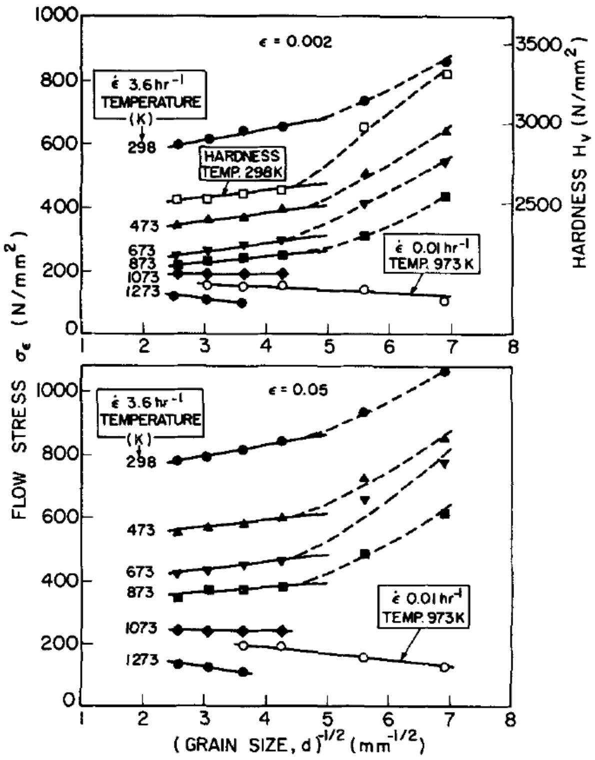

Figure 2.3: Hall-Petch plots showing variation of flow stress and hardness with grain size for Cr-Mn-N austenitic steel [61].

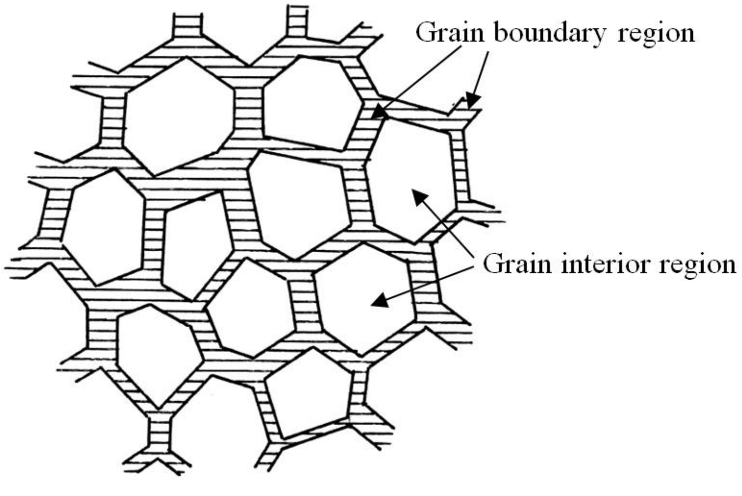

Figure 2.4: Schematic drawing of the structure along a shear plane in a nanocrystal. Shaded bands correspond to the boundary region [65].

In addition to the previous physical mechanisms, there exist other explanations for the IHPE (e.g. grain boundaries as sources and sinks for dislocations [67] and dislocation motion through multiple grains [68]), which have not been reviewed here. However, due to limited experimental results and the difficulty in obtaining artifact-free samples of nanocrystalline materials [66], the actual mechanisms for the IHPE have not been completely understood so far. Most of the studies adopt phenomenological models to describe the IHPE based on experimental observations. While more and more physical mechanisms have been incorporated into models recently, they still rely heavily on data fitting methods.

The majority of earlier studies investigate the IHPE at room temperature. Therefore, the IHPE is modeled as a function of grain size only in these studies. Meanwhile, the influence of temperature on the IHPE has been investigated in several studies [61, 69]. Carlton and Ferreira [69] pointed out that the inverse Hall-Petch effect is very sensitive to several influences, e.g. strain rate, temperature, and specific activation energy, which was also confirmed by experimental studies performed by Li et al. [70] and Blum et al. [71]. According to Blum et al. [71]'s study, the trend of flow stress as a function of grain size at room temperature, which followed the Hall-Petch relation, was reversed as the flow stress decreased with grain size at an elevated temperature. This phenomenon has also been observed by Rao et al. [61] (see Figure 2.3), which was discussed previously. Such experimental observations provide solid evidence for the influence of temperature on the critical grain size for initiating the IHPE.

Considering the severely refined grain structure due to DRX and the elevated temperature within the primary shear zone, it is necessary to incorporate the IHPE into the constitutive material model to accurately describe the material behavior during machining.

2.5 Machining Simulation

Numerical simulation of machining processes using the finite element method (FEM), as shown in Figure 2.5, offers a cost-effective alternative to optimize the cutting conditions and select the right material and geometry for the cutting tool without conducting costly experiments.

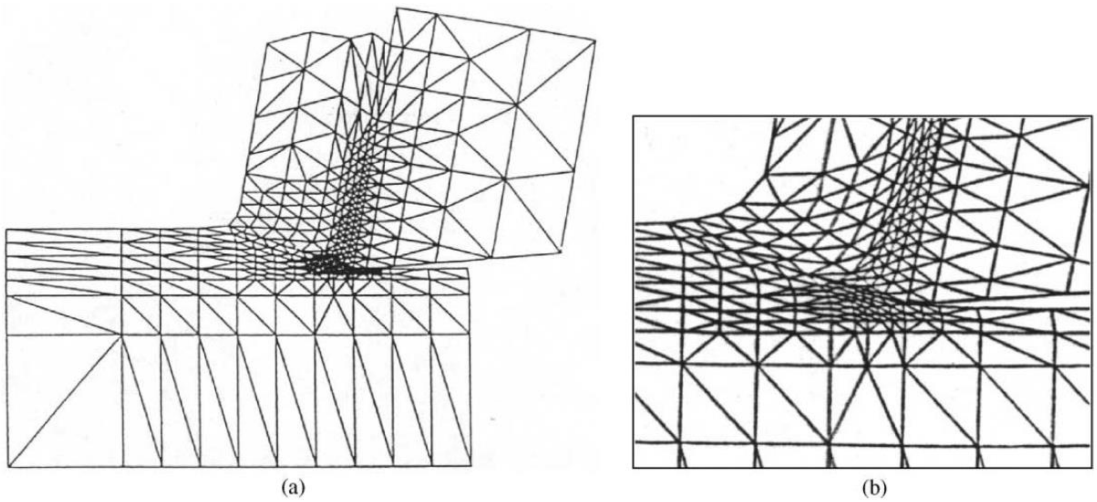

Figure 2.5: (a) Finite element meshing scheme; (b) magnified mesh detail around the cutting edge [72].

Considering that the workpiece material experiences severe plastic deformations accompanied by thermal and frictional phenomena during machining, finite element simulation provides an ideal approach to model the material behavior in machining. In order to comprehensively describe the cutting process, the machining simulation must consider the material flow properties, material thermal properties, friction, a chip separation/formation criterion, algorithms for mesh type, boundary conditions, and convergence criteria. Finite element modeling and simulation of machining has been reported by a number of studies and is quite well-established [4, 72-76]. For example, Childs and his co-workers reported on the modeling of the machining process [72], constitutive material modeling [77], tool wear modeling [78], tool-chip interace friction characterization and modeling [79], and the effect of coolants [80] using the finite element method.

The constitutive material model which describes the complex thermo-mechanical behavior of the material during the cutting operation is central to FEM-based machining simulation. In combination with the finite element method, phenomenological constitutive models have been widely used to predict the cutting forces, strain, strain rate and temperature distributions in the machined surface layer and chip, and to analyze the deformation mechanisms during machining, due to their simplicity. The power law model, a popular phenomenological model, has been used in machining simulation by many researchers. Using a temperature dependent friction law, Moufki et al. [81] adopted the power law model to simulate the orthogonal cutting process for 1018 steel. Lei et al. [82, 83] applied a power law model with a modified thermal function to simulate the orthogonal cutting of 1020 steel. The JC model is another kind of phenomenological model which has been widely used in machining simulations. Shatla et al. [84, 85] calibrated the JC model and applied it in machining simulations for three different metals. Their simulation results showed reasonable agreement with experimental results. Furthermore, in Shi and Liu's study [86], four phenomenological constitutive models, the

Litonski-Batra model [87, 88], the power law model, the JC model, and the Bodner-Partom model [89], have been implemented and cross-referenced to predict the cutting forces, chip geometry, stress and temperature distributions, and residual stress in machining of HY-100 steel using the finite element method.

From the previous discussion, it can be learned that phenomenological constitutive models show good performance in prediction of the machining processes that yield continuous chips. However, due to the lack of physical mechanisms considered by phenomenological models, the fidelity of simulations relies heavily on the calibration procedure. Furthermore, except the chip geometry and cutting forces, very limited information can be derived from machining simulations with phenomenological constitutive models. In order to address these limitations, physically based models with microstructure evolution laws have been proposed in recent studies.

Ding and Shin adopted the dislocation based material model developed by Estrin et al. [90] and Tóth et al. [35] (ET model) to simulate chip formation and grain refinement in orthogonal cutting of aluminum and copper [91] and commercially pure titanium (CP-Ti) [92], as shown in Figure 2.6. Considering the dislocation cell structure as a precursor for the developing grain structure, Ding and Shin [92] traced the evolution of cell size during orthogonal cutting of CP-Ti to simulate grain refinement, similar to Estrin and Kim’s [37] work on the ECAP process. However, a key limitation of the ET model is that it assumes the existence of an established dislocation cell structure prior to deformation and consequently is strictly only valid for dislocation cell forming materials that have undergone sufficient straining for a cell structure to develop [36]. This limitation therefore also extends to Ding and Shin’s model for orthogonal cutting.

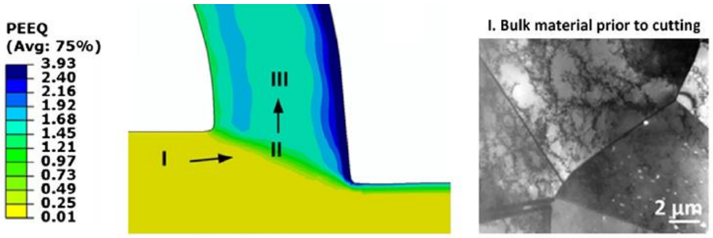

(a) Equivalent strain

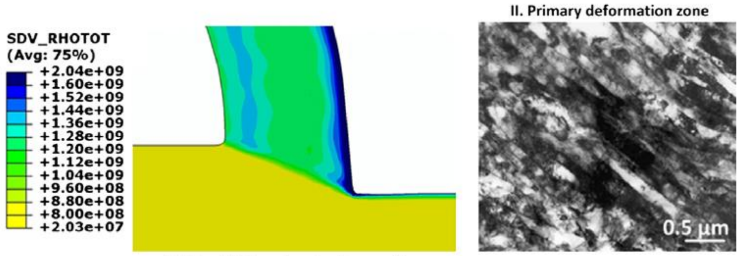

(b) Total dislocation density, mm^{-2}

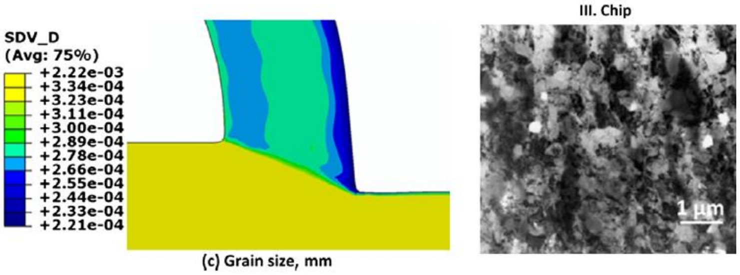

(c) Grain size, mm

Figure 2.6: Predicted microstructure evolution in cutting of OFHC Cu [91].

Ding et al. [91] also applied the ET model to predict the chip formation and grain refinement in orthogonal cutting of OFHC Cu under different cutting conditions. Similarly, Ding and Shin [93] and Ding et al. [94] used the ET model and associated dislocation density and grain size evolution laws to predict the microstructure evolution in machining of bearing steels and Al 6061-T6 alloy.

Svoboda et al. [95] adopted the physically based plasticity model developed by Lindgren et al. [46] to simulate the orthogonal cutting of 316L stainless steel alloy. This model was based on the dislocation glide mechanism and the flow stress was formulated as the summation of resistance to dislocation motion imposed by short- (thermal stress) and long- (athermal stress) range obstacles. The dislocation density and vacancy concentration were taken as ISVs and the flow stress was expressed as an explicit function of these microstructure-based internal state variables (ISVs) in the Lindgren model. In addition, the evolution of ISVs with inelastic deformation was captured via two evolution equations. However, no evolution equation was derived for the grain size indicating the absence of dynamic recrystallization (DRX), which is a limitation of the Lindgren model. Moreover, Svoboda et al. [95] compared the predictive capability of their physically based dislocation density model with the phenomenological JC model in machining of SS316L. They concluded that the former model yielded better predictions than the JC model, because the physically based plasticity model captured more mechanisms operating in the extrapolated range.

The constitutive models described in the previous section have been adopted in successfully simulating continuous chip formation. However, as shown in Figure 2.7, they are limited in their ability to accurately simulate more complex chip formation, such as segmented chips in machining of titanium and its alloys. This is largely because of their lack of physical micro-scale mechanisms responsible for such chip formation.

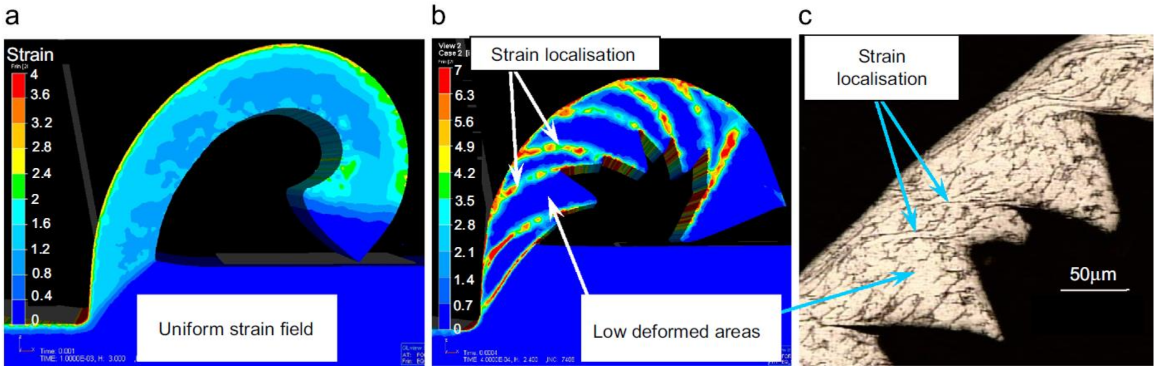

Figure 2.7: Strain field of (a), (c) predicted and (b) experimental chip using: (a) JC and (c) TANH models for a cutting speed of 180 m/min and a feed of 0.1 mm [96].

2.6 Shear Banding and Chip Segmentation

The segmented chip, as shown in Figure 2.8 (b) is commonly observed in machining materials with low thermal conductivity (e.g. titanium and its alloys). The low thermal conductivity of these materials gives rise to heat accumulation in the primary shear zone, which contributes to shear localization and chip segmentation, which in turn can cause harmful tool/workpiece vibrations. Due to the extremely high deformation rate within a very localized area, the complicated physical mechanisms responsible for chip segmentation are still not well understood. However, there is broad agreement in the machining literature that chip segmentation can be attributed to the material losing its load bearing capacity inside the shear band.

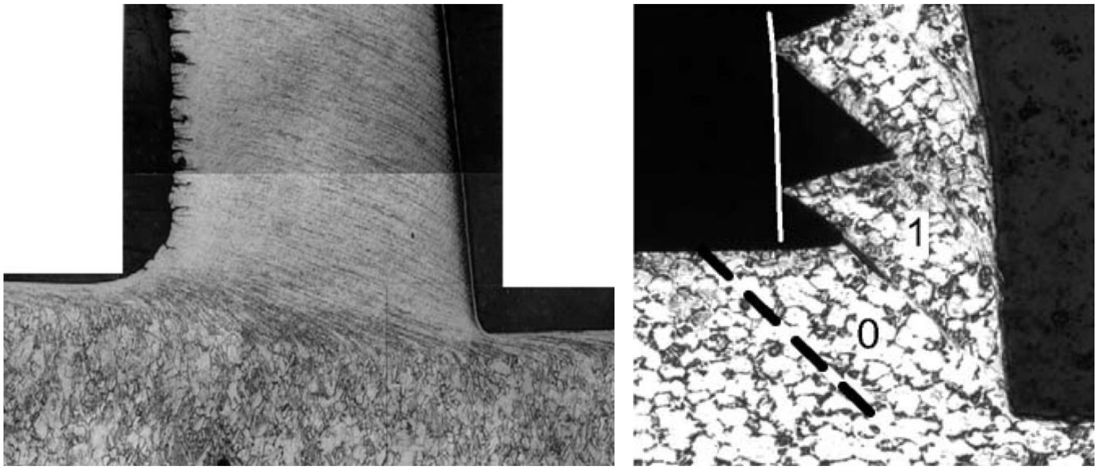

(a) (b)

Figure 2.8: Comparison of (a) continuous chip in machining of copper [97], and (b) segmented chip in machining of Ti-6Al-4V [98].

Based on the observations of voids and microcracks [99, 100] within the shear band, chip segmentation can be predicted by considering the fracture mechanism with suitable fracture criteria to characterize the initiation and propagation of voids and cracks inside the shear band. In previous work, various fracture criteria have been proposed.

Marusich and Ortiz [74] classified the fracture accompanying segmented chip formation as brittle and ductile fracture. A critical crack opening stress criterion was employed to detect brittle fracture through the small-scale yielding relation:

$$\bar{\sigma}_f = \frac{K_{IC}}{\sqrt{2\pi\bar{l}}} \tag{2.12}$$

where $\bar{\sigma}_f$ is the critical stress, K_{IC} is the fracture toughness, and $\bar{l}$ is the critical distance that is correlated with the spacing of grain boundary carbides. For ductile fracture, the critical strain criterion given below and derived from the crack tip opening displacement theory was adopted:

$$\bar{\varepsilon}_f = 2.48e^{-1.5\bar{p}/\bar{\sigma}} \tag{2.13}$$

where $\bar{\varepsilon}_f$ is the critical plastic strain, $\bar{p}$ is the hydrostatic pressure, and $\bar{\sigma}$ is the effective Mises stress.

The deformation energy-based criterion (see Equation 2.14) proposed by Cockroft and Latham [101] was employed by Hua and Shivpuri [102]’s study to simulate segmented chip formation in machining of Ti-6Al-4V. This criterion has also been employed by Umbrello et al. [103, 104] in simulating the cutting of AISI 316L and Ceretti et al. [105] in simulating the cutting of AISI 1045:

$$\overline{D} = \int_0^{\bar{\varepsilon}} \sigma^* d\varepsilon \tag{2.14}$$

where $\overline{D}$ is a material constant, $\bar{\varepsilon}$ is the equivalent plastic strain, and σ^* is the principal stress.

The Johnson-Cook damage model, which was first presented by Johnson [106], is another material failure criterion used to simulate shear banding as in the work of Guo and Yen [107] and Barge et al. [108]:

$$\overline{D} = \sum \frac{\Delta\bar{\varepsilon}}{\bar{\varepsilon}^f} \tag{2.15}$$

where $\overline{D}$ is a material constant, $\Delta\bar{\varepsilon}$ is the increment of equivalent plastic strain during an integration cycle, $\bar{\varepsilon}^f$ is the equivalent strain to fracture under the current conditions of strain rate, temperature, pressure and equivalent stress.

Obikawa and Usui [109] also adopted a fracture mechanism with a strain-based criterion to simulate segmented chip formation in machining of Ti-6Al-4V. In their study, crack initiation and propagation is realized by separating an element node when the effective plastic strain reaches a predetermined critical value as follows:

$$\begin{gathered} \bar{\varepsilon} > \bar{\varepsilon}_f \\ \bar{\varepsilon}_f = -MAX\left[0.075\, ln\left(\frac{d\bar{\varepsilon}}{100}\right), 0\right] - \frac{\bar{p}}{37.8} + 0.09exp\left(\frac{T}{293}\right) \end{gathered} \tag{2.16}$$

where $\bar{\varepsilon}_f$ is the critical plastic strain, $\bar{\varepsilon}$ is the equivalent plastic strain, $d\bar{\varepsilon}$ is the equivalent plastic strain rate, $\bar{p}$ is the hydrostatic pressure, and T is the absolute temperature.

In addition, the effect of the fracture mechanism was also phenomenologically accounted for by Liu et al. [110] in their modified JC model to predict chip segmentation, as shown in Figure 2.9.

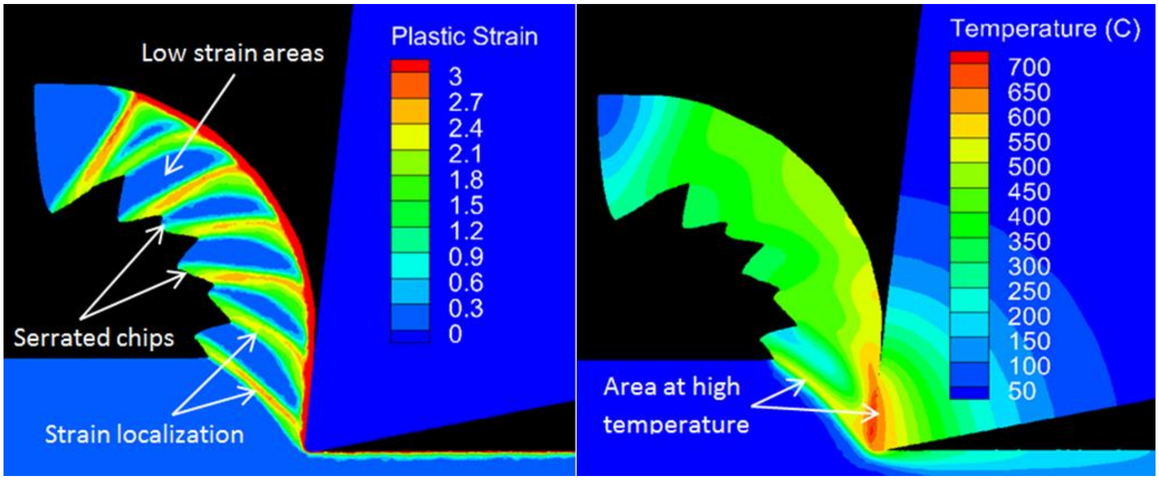

Figure 2.9: (a) Strain field and (b) temperature distribution in simulated chips at a cutting speed of 120 m/min and a feed of 0.1 mm in machining of Ti-6Al-4V [110].

According to the above studies, the segmented chip can be successfully simulated via the fracture mechanism. However, Chichili et al. [111] pointed out that the normal compressive stress inside the shear band can prevent void or crack formation. Besides the fracture mechanism, a strain softening phenomenon has been used to explain segmented chip formation by Hua and Shivpuri [112]. In their work, the strain softening phenomenon described the softening in stress with increasing strain when the strain is larger than a critical value. Later, this strain softening phenomenon was modeled phenomenologically by Calamaz et al. [96]:

$$\sigma = (\bar{A} + \bar{B}\varepsilon^{\bar{n}})\left(1 + \bar{C}ln\frac{\dot{\varepsilon}}{\dot{\varepsilon}_r}\right)\left[1 - \left(\frac{T - T_{room}}{T_{melting} - T_{room}}\right)^{\bar{m}}\right] \times \left[\bar{H} + (1 - \bar{H})tanh\left(\frac{1}{(\varepsilon + \bar{S})^{\bar{r}}}\right)\right] \tag{2.17}$$

where $\bar{H}$, $\bar{S}$, $\bar{r}$ are material constants. Similar methods have been used to predict chip segmentation by Calamaz et al. [96, 113, 114] and Sima and Özel [115] as shown in Figure 2.7. However, these studies loosely attributed the strain softening phenomenon to microstructure evolution without providing any justification.

2.7 Conclusions

As a key component of the machining simulation, the constitutive model has been well established in numerous studies. In order to improve the accuracy of constitutive model extrapolation beyond the calibration range, more and more physics-based constitutive models incorporating micro-scale physical mechanisms, such as dynamic recovery, dynamic recrystallization, have been developed. However, during machining, additional mechanisms such as dislocation drag and severe grain refinement induced softening (e.g. inverse Hall-Petch effect) can be active and need to be considered. Moreover, in order to realize the need for predicting the machined surface microstructure, a unified constitutive material model explicitly incorporating the effect of microstructure and its evolution due to plastic straining is needed.

In conjunction with the finite element method, constitutive models have been widely used to simulate the machining process, particularly in terms of the cutting forces, chip geometry, and deformation parameters such as strain, strain rate, and temperature. Continuous chip formation has been successfully simulated by a number of investigators. However, limited work has been reported on physics-based constitutive models capable of accurately simulating segmented/shear localized chip formation in machining of low thermal conductivity metals, such as titanium and its alloys. These limitations of prior work provide the motivation for the work reported in the following chapters of this thesis.

CHAPTER 3

DEVELOPMENT OF A UNIFIED CONSTITUTIVE MODEL

3.1 Introduction

The objective of this chapter is to develop a unified constitutive model, which describes the material response to various thermo-mechanical loadings common in metal cutting by integrating microstructure evolution into the macroscopic constitutive description of material behavior. The developed unified model is calibrated and validated through flow stress curves for AISI 304 stainless steel. Then, the validated model is utilized to assess and discuss the ability of the model to reproduce various features of inelastic deformation including thermal softening and sensitivity, rate hardening and sensitivity, and strain hardening rate. Additionally, the unified constitutive model is used to investigate the effects of strain, strain rate, and temperature on different components of the constitutive law. The average grain size and dislocation density evolution are also analyzed and discussed. The proposed unified model is expected to provide an insight into the microstructure evolution and corresponding impact on the macro-scale plastic flow in severe plastic deformation processes such as machining and metal forming.

3.2 The Unified Constitutive Model

The unified constitutive model introduced here seeks to describe the inelastic behavior as an explicit function of microstructure where the flow stress, σ, depends on the current microstructure and its evolution with strain, ε. It is assumed that the microstructure can be represented by two parameters, i.e. dislocation density, ρ, and average grain size, *D*; and that not only the flow stress but also microstructure evolution depends on the strain rate, $\dot{\varepsilon}$, and temperature, *T*. The general form of the unified model is written as follows:

$$\sigma = \sigma(\rho, D; \dot{\varepsilon}, T) \tag{3.1a}$$

$$\frac{d\rho}{d\varepsilon} = F_1(\rho, D; \dot{\varepsilon}, T) \tag{3.1b}$$

$$\frac{dD}{d\varepsilon} = F_2(\rho, D; \dot{\varepsilon}, T) \tag{3.1c}$$

where Equation 3.1a is the constitutive law and Equations 3.1b and 3.1c are microstructure evolution laws. As such, the macro-scale inelastic behavior is described explicitly as a function of the current microstructure of the material represented by two internal state variables dislocation density, ρ, and average grain size, *D*. In the sequel, a special form of the general formulation for the unified model in Equation 3.1 is derived using the thermal activation theory [24]. A more rigorous definition of the unified constitutive model has been provided by Krausz and Krausz [116]. Nes and his co-workers [117, 118] have also proposed the concept of a unified constitutive model incorporating microstructure evolution during plastic deformation.

According to the thermal activation theory, the flow stress can be formulated as the superposition of an athermal (σ_a) and a thermal (σ_{th}) component as follows:

$$\sigma = \sigma_a + \sigma_{th} \tag{3.2}$$

3.2.1 Thermal component of flow stress

In general, this component of flow stress is a product of a rate and temperature dependent term, $s(\dot{\varepsilon}, T)$, and a structure dependent term σ_0 as follows:

$$\sigma_{th} = s(\dot{\varepsilon}, T)\sigma_0 \tag{3.3}$$

where s approaches 1 as T goes to 0. The magnitude of σ_{th} depends on the strength of interactions between dislocations and short-range barriers (e.g. interstitial impurities, substitutional alloying elements, precipitates, other dislocations, and even lattice friction). The higher the temperature, the smaller the magnitude of thermal stress needed to overcome the short-range barriers. This stress component is formulated using the KM model [6, 12] as follows:

$$\sigma_{th} = \left[1 - \left(\frac{kT}{g_0 \mu b^3} ln\left(\frac{\dot{\varepsilon}_0}{\dot{\varepsilon}}\right)\right)^{1/q}\right]^{1/p} \sigma_0 \tag{3.4}$$

where, k is the Boltzmann's constant, T is the temperature, g_0 is the normalized activation energy at 0 K, μ is the shear modulus, b is the magnitude of the Burgers vector, $\dot{\varepsilon}_0$ is the reference strain rate, σ_0 is the stress required to overcome short range obstacles at 0 K, and p and q are parameters defining the shape of energy barriers associated with short range obstacles. Follansbee [22], Follansbee and Gray [20] and Picu and Majorell [33] separated the effects of different short range obstacles on the thermal stress and defined it as a superposition of all contributions by short range obstacles as follows:

$$\sigma_{th} = \sum_{i=1}^{r} \left[1 - \left(\frac{kT}{g_{0i} \mu b^3} ln \left(\frac{\dot{\varepsilon}_{0i}}{\dot{\varepsilon}} \right) \right)^{1/q_i} \right]^{1/p_i} \sigma_{0i} \tag{3.5}$$

where subscript i refers to different types of short range obstacles and r is the total number of such obstacle types.

Follansbee and Gray [20] also showed that the parameters of the KM model in Equation 3.4 could be identified in a manner that this equation would be equivalent to the summation in Equation 3.5. In other words, the effects of all types of short range obstacles could be combined and represented by only one term of the KM model. This equivalent form is used here for the sake of simplicity and because it has fewer parameters. The variation of the shear modulus μ with temperature is modeled using Equation 3.6 [119] as follows:

$$\mu = \mu_0 - \frac{a}{e^{(T_r/T)} - 1} \tag{3.6}$$

where μ_0 is the shear modulus at $0\ K$ and a and T_r are material constants.

3.2.2 Athermal component of flow stress

This component of flow stress comes from the interaction of dislocations with long range obstacles such as grain boundaries and dislocation forests. It is believed that within the operating range of common thermomechanical processes (~T < $0.5T_{melting}$), the temperature effect on this component of flow stress is negligible and as such it is called athermal stress. Historically, strain hardening has been associated with the athermal stress while the temperature and strain rate sensitivities have been associated with the thermal stress. This component of flow stress is formulated in Equation 3.7 as the sum of stresses required to overcome far-field strain fields of dislocation forests, σ_ρ, and grain boundaries, σ_G, by an individual dislocation:

$$\sigma_a = \sigma_\rho + \sigma_G = \alpha_\rho \, \mu(T) \, b \sqrt{\rho} + \frac{\kappa_G}{\sqrt{D}} \tag{3.7}$$

Here α_ρ is a temperature and rate dependent parameter related to the strength of dislocation-dislocation forest interactions, b is the Burgers vector magnitude, μ is the temperature dependent shear modulus defined in Equation 3.6, and finally κ_G is the Hall-Petch constant. The ISVs, ρ and D, evolve during inelastic deformation and knowing their values at each strain increment, the flow stress can be calculated by superposing the thermal and athermal components as indicated by Equation 3.2. The evolution of the ISVs and their corresponding formulations are addressed in the following two sections.

3.3 Microstructure Evolution Scheme

The microstructure evolves during inelastic deformation through DRX under favorable conditions. Currently, it is widely believed that DRX occurs via two micro-scale mechanisms called continuous DRX and geometric DRX [120]. In Continuous DRX or CDRX [121], low angle boundaries (LABs) are formed inside grains due to dislocation accumulation. As inelastic deformation proceeds, new LABs are formed and misorientation angles of existing LABs grow larger. When the misorientation angle becomes larger than a critical value, the corresponding LAB transforms into a high angle boundary (HAB). HABs are much like original grain boundaries and divide each grain into subgrains. This refinement or recrystallization happens in a continuous manner since new LABs are continuously formed and converted into HABs as described above. It is also dynamic due to the fact that mechanical straining both triggers and feeds the process. In geometric DRX or GDRX [122, 123], grains elongate during deformation and beyond a certain level of strain, grain boundaries experience a serration which brings certain points on the boundaries closer to each other and ultimately grains pinch off at those locations and thereby a grain divides into multiple new grains. Regardless of which mechanism is the source of DRX, dislocation density and grain size evolutions are by-products of the process and will be modeled as follows.

3.3.1 Dislocation density evolution law

Estrin and Mecking [14] proposed the evolution law for dislocation density shown in Equation 3.8. Here, the first term on the right hand side is the dislocation production (hardening) term and the second term is the strain rate- and temperature-dependent dislocation annihilation (recovery) term:

$$\frac{d\rho}{d\varepsilon} = A\sqrt{\rho} - B(\dot{\varepsilon}, T)\rho \qquad (3.8)$$

In the above equation, A and B are hardening and recovery parameters, respectively. The closed-form solution of Equation 3.8 is as follows:

$$\rho_{H\,\&\,DRV} = \left[\frac{A}{B} + \left(\sqrt{\rho_0} - \frac{A}{B}\right) exp\left(-\frac{B\varepsilon}{2}\right)\right]^2 \tag{3.9}$$

where ρ_o is the initial dislocation density and $\rho_{H\&DRV}$ is an intermediate dislocation density determined by the competing dislocation production (hardening) and annihilation (dynamic recovery) processes.

3.3.2 Grain size evolution law

DRX, on the other hand, leads to the evolution of average grain size during inelastic deformation. It is also thought to be responsible for further softening observed at high strains. The following phenomenological model is introduced in this study to capture the grain size evolution during inelastic deformation:

$$D = D_f + \left(D_0 - D_f\right)\tanh\left(\frac{\varepsilon_r}{\varepsilon}\right)^u \tag{3.10}$$

where ε_r is the critical strain at which DRX occurs, u is a temperature and strain rate dependent fitting parameter controlling the DRX rate, D_o is the initial grain size, and D_f is the final recrystallized grain size defined as a function of the Zener-Hollomon parameter (Z):

$$D_f = C_z Z^{-m} \tag{3.11}$$

where C_z and m are fitting parameters. DRX affects the grain boundary strengthening component (σ_G) of the athermal stress in Equation 3.7 via the resultant grain refinement. However, the effect of DRX on microstructure and flow stress is not limited only to grain refinement and grain boundary strengthening. Dislocations are also consumed during DRX to form new grain boundaries and, therefore, dislocation density and associated strengthening component (σ_ρ) of the athermal stress are also affected. In this study, the DRX-induced change in dislocation density is assumed to be proportional to the change in grain surface area per unit volume (S) as follows:

$$\Delta\rho_{DRX} = -K(\dot{\varepsilon},T)\Delta S = K(\dot{\varepsilon},T)\left[\frac{2}{D_0} - \frac{2}{D}\right] \tag{3.12}$$

where K is a strain rate and temperature dependent constant. The minus sign is due to the opposite evolution trends for dislocation density and grain surface area per unit volume. Moreover, S is inversely proportional to the average grain size (D) according to the stereological relation $D=2/S$. The proposed unified framework which integrates the evolution of microstructure into the constitutive description of material behavior is illustrated in Figure 3.1. Moreover, the macro-scale effect of DRX on the flow stress is shown schematically in Figure 3.2. The proposed unified material will be calibrated in the next section using the experimental data for AISI 304 stainless steel.

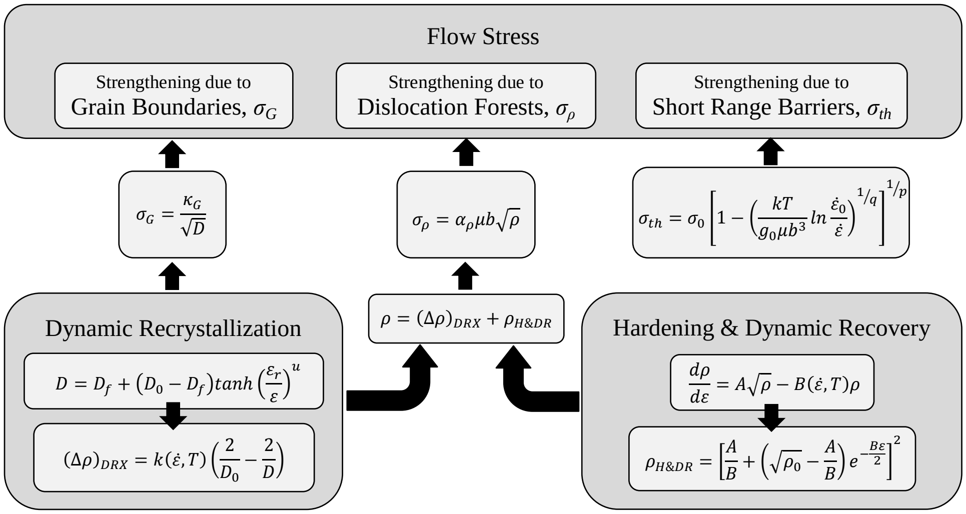

Figure 3.1: Flow diagram representation of the proposed unified constitutive modeling framework.

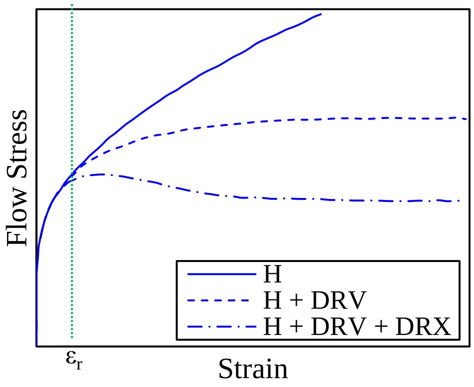

Figure 3.2: Schematic representation of dynamic recrystallization (DRX) effect on a flow curve with hardening (H) and dynamic recovery (DRV).

3.4 Model Calibration and Validation

Although a core idea in the development of physics-based models is to alleviate the need for calibration and dealing with material constants rather than model parameters, very often one needs to implement phenomenological descriptions for some parameters, e.g. hardening or recovery terms, arising during the model derivation. Therefore, partial calibration seems to be inevitable even for physics-based models. In this section, the proposed model was calibrated for AISI 304 stainless steel due to wide industrial application of austenitic stainless steels. However, it is anticipated that the calibration procedure introduced in this section is applicable to other metals and alloys as well. The initial grain size, D_0, and dislocation density, ρ_0, were taken to be 35 μm and 10^{12} m^{-2}, respectively [30]. The temperature dependent shear modulus for this alloy is as follows:

$$\mu(T) = 81.82 - \frac{22.27}{e^{(592/T)} - 1} \ GPa \quad \left(0 < T < T_{melting}\right) \tag{3.13}$$

The Hall-Petch coefficient, κ_G, in Equation 3.7 was taken to be temperature dependent as follows [124]

$$\kappa_G = \alpha_G \mu(T) \sqrt{b} \tag{3.14}$$

where the Burgers vector magnitude (b) is 2.56×10^{-10} m. According to Di Schino and Kenny [125] κ_G is equal to 490 MPa.$\sqrt{\mu\mathrm{m}}$ at room temperature. Replacing κ_G, μ, and b in Equation 3.14 with appropriate values, α_G was calculated as 0.39 and was assumed to be temperature independent. The Zener-Hollomon parameter (Z) in Equation 3.11 is defined as follows:

$$Z = \dot{\varepsilon} e^{\left(\frac{Q}{RT}\right)} \tag{3.15}$$

where Q is the activation energy for lattice self-diffusion (400 kJ/mol [126]) and R is the gas constant (8.314 J K^{-1} mol^{-1}). The variation of final recrystallized grain size, D_f, with temperature and strain rate in Equation 3.11 was calibrated by fitting Equation 3.11 to experimental data reported by Yazdipour et al. [30] and shown in Figure 3.3. Equation 3.11, after calibration, is given by:

$$D_f = 9080.3\, Z^{-0.18} \quad \mu m \qquad (Z > 10^{13.5}\ s^{-1})$$

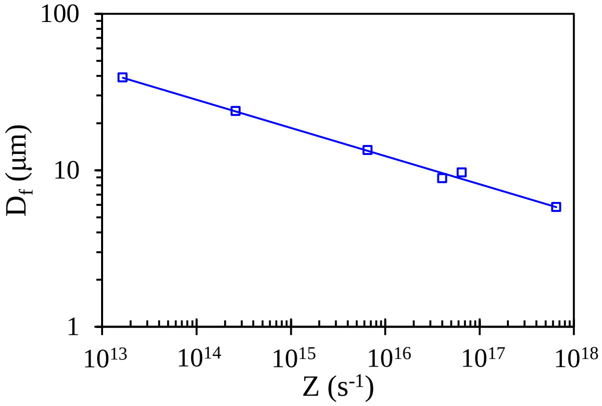

Figure 3.3: Variation of final grain size versus Zener-Hollomon parameter (symbols-measurements; solid line-model).

To calibrate the grain size evolution law, Equation 3.10 was rearranged (shown schematically in Figure 3.4) into a form matching the reported experimental data by Yazdipour et al. [30]. After fitting the rearranged form of Equation 3.10 to experimental data in Figure 3.5, the critical strain and rate controlling parameter were obtained as $\varepsilon_r = 0.33\, log_{10}^{Z} - 4.1, (Z > 10^{12.5}\ s^{-1})$ and $u = 0.84\, log_{10}^{Z} - 10.2, (Z > 10^{12.2}\ s^{-1})$, respectively.

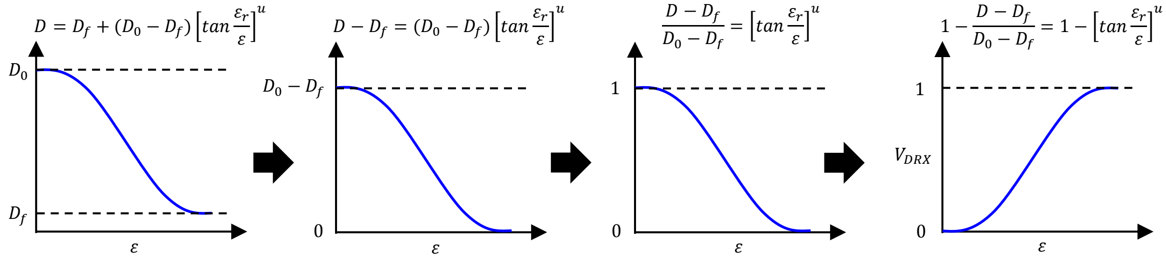

Figure 3.4: Schematic representation of rearrangement of Equation 3.10 to match the format of experimental data reported in Ref. [30].

The thermal component of flow stress in Equation 3.4 brings five extra parameters (i.e. $\dot{\varepsilon}_0$, p, q, g_0, and σ_0) into the calibration process. The values for reference strain rate ($\dot{\varepsilon}_0$) and the parameters defining the shape of energy barriers (p and q) were taken to be equal to those reported in Ref. [22] for austenitic stainless steels as follows: $\dot{\varepsilon}_0 = 10^8/s$, $p = 0.5$, and $q = 1.5$. To calibrate the mechanical threshold stress (σ_0) and normalized activation energy (g_0), the yield stress (i.e. the flow stress when the inelastic deformation ε is zero) was written as follows using Equations 3.2, 3.4, 3.7 and 3.14:

$$\sigma_Y = \frac{\alpha_G \mu \sqrt{b}}{\sqrt{D_0}} + \alpha_\rho \mu b \sqrt{\rho_0} + \sigma_0 \left[1 - \left(\frac{kT}{g_0 \mu b^3} ln \frac{\dot{\varepsilon}_0}{\dot{\varepsilon}}\right)^{1/q}\right]^{1/p} \tag{3.16}$$

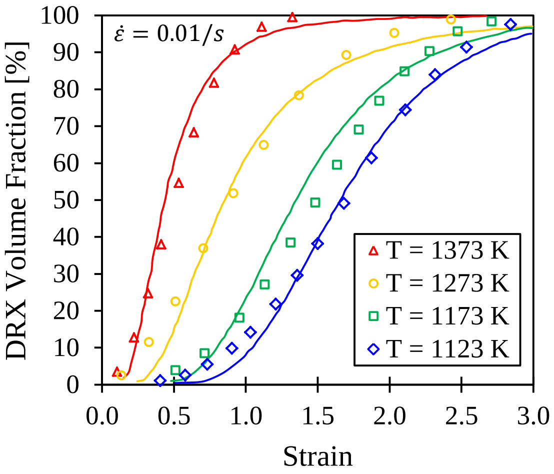

Figure 3.5: Illustration of rearranged form of Equation 3.10 fitted to experimental data (symbols) reported in Ref. [30]

Here, α_ρ is a temperature and rate dependent parameter and is less than unity (i.e. $0 < \alpha_\rho < 1$). However, the temperature and rate dependency of α_ρ was assumed to be negligible at this stage of the calibration process and initialized at 0.5. A rearrangement of Equation 3.16 results in Equation 3.17 as follows:

$$\left(\frac{\sigma_Y - \alpha_G \mu \sqrt{b}/\sqrt{D_0} - \alpha_\rho \mu b \sqrt{\rho_0}}{\sigma_0}\right)^p = 1 - \frac{1}{g^{1/q}}\left(\frac{kT}{\mu b^3} ln \frac{\dot{\varepsilon}_0}{\dot{\varepsilon}}\right)^{1/q} \tag{3.17}$$

The left hand side of Equation 3.17 versus $(kT/\mu b^3 \, ln \, \dot{\varepsilon}_0/\dot{\varepsilon})^{1/q}$ represents a straight line. σ_0 = 545 MPa and g = 0.213 were obtained by rearranging the experimental yield stress data [127] into the particular format shown in Equation 3.17 and fitting a straight line to the rearranged data (see Figure 3.6).

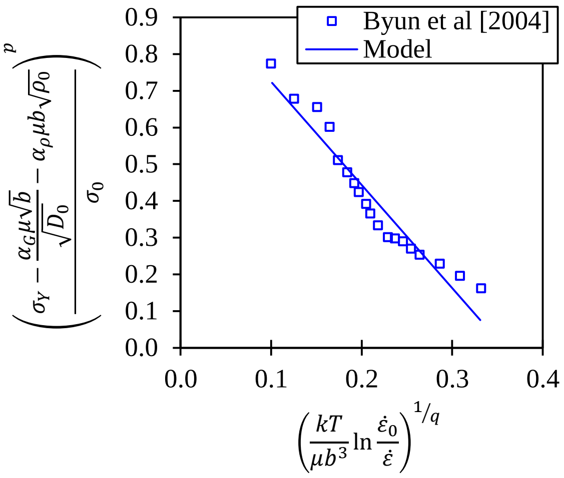

Figure 3.6: Fitting a straight line to rearranged experimental data [127] in order to calibrate σ_0 and g_0

The next step is to calibrate the hardening (*A*) and recovery (*B*) parameters of the dislocation density evolution law in Equation 3.8. This portion of dislocation density evolution stems from the dislocation production (storage) and annihilation mechanisms in the absence of dynamic recrystallization. The latter is synonymous with $D = D_0$, $\Delta\rho_{DRX}$ =0., and σ_G = *Const.* To eliminate the effect of DRX on the evolution of dislocation density, only the portions of experimental stress-strain curves [30] where the inelastic strain is less than the critical strain (ε_r) were used. Additionally, since thermal stress is not strain dependent, σ_{th} = *Const* and σ_ρ was the only varying stress component. Following Estrin & Mecking [14], *A* was considered to be a constant and *B* a temperature and strain rate dependent term as follows:

$$A = Const. \tag{3.18}$$

$$B = B_1(T) \times B_2(\dot{\varepsilon}) \tag{3.19}$$

Equation 3.19 decouples the temperature and strain rate dependencies. This representation was selected for its convenience during the calibration process. The following are the particular forms identified for B_1 and B_2:

$$B_1 = b_0 \, e^{\frac{b_1}{b_2 - T}} \tag{3.20}$$

$$B_2 = b_3 \left[\log_{10} \frac{\dot{\varepsilon}}{b_4}\right]^{b_5} \tag{3.21}$$

To calibrate A and the temperature dependent term B_1, three stress-strain curves at T = 650 ^{o}C, 900 ^{o}C, and 1000 ^{o}C, constant strain rate of $\dot{\varepsilon}$ = 0.01/s, and $\varepsilon < \varepsilon_r$ were used to obtain the best fit to experimental data resulting in $A = 568 \times 10^6$, $b_0 = 5.025$, $b_1 = 457.6$, and $b_2 = 1538.67$. Next, to calibrate the strain rate dependent term B_2, three stress-strain curves at $\dot{\varepsilon}$ = 0.001/s, 0.01/s, and 10/s, constant temperature of T = 900 ^{o}C, and $\varepsilon < \varepsilon_r$ in addition to the constraint that B_2 (0.01/s) = 1.0 were used to obtain the best fit to experimental data resulting in $b_3 = 1.289$, $b_4 = 10^{-4}$, and $b_5 = -0.3658$. Besides the calibration of hardening and recovery parameters, the temperature and strain rate dependency of α_ρ was revived at this point and simultaneously calibrated (with A and B) by assuming a decoupled form for α_ρ as follows:

$$\alpha_\rho = \alpha_{\rho 1}(T) \times \alpha_{\rho 2}(\dot{\varepsilon}) \tag{3.22}$$

$$\alpha_{\rho 1}(T) = \alpha_0 e^{\frac{\alpha_1}{T - \alpha_2}} \tag{3.23}$$

$$\alpha_{\rho 2}(\dot{\varepsilon}) = \alpha_3 \dot{\varepsilon}^{\alpha_4} \tag{3.24}$$

To calibrate the temperature ($\alpha_{\rho 1}$) and strain rate ($\alpha_{\rho 2}$) dependent terms, the same stress-strain curves used in the calibration of A and B were used in addition to a new constraint that $\alpha_{\rho 2}$ (0.01/s) = 1.0 resulting in $\alpha_0 = 1.617$, $\alpha_1 = 886$, $\alpha_2 = 1673$, $\alpha_3 = 1.408$, and $\alpha_4 = 0.074$. After this, the calibrated form of Equation 3.22 was applied rather than the previously used constant value of 0.5 to complete the model calibration.

The plot shown in Figure 3.6 was regenerated using the fully calibrated model and compared to experimental data. The root mean square error between the model prediction and experimental data was calculated and if it was larger than a pre-specified threshold value, another iteration with a new constant value for α_ρ would be carried out until the root mean square error was less than or equal to the pre-specified threshold value (see flow chart of calibration procedure in Figure 3.7).

Finally, to calibrate the DRX-induced evolution of dislocation density in Equation 3.12, the temperature and strain rate dependent proportionality parameter K was written in a decoupled form as follows:

$$K = K_1(T) \times K_2(\dot{\varepsilon}) \tag{3.25}$$

$$K_1(T) = c_0 T^{c_1} \tag{3.26}$$

$$K_2(\dot{\varepsilon}) = c_2 \left[\log_{10} \frac{\dot{\varepsilon}}{c_3}\right]^{c_4} \tag{3.27}$$

As mentioned earlier, this portion of the dislocation density evolution is caused by dynamic recrystallization, which is synonymous with $D \neq D_0$, $\Delta\rho_{DRX} \neq 0.$, and $\sigma_G \neq Const.$ To include the effect of DRX on the evolution of dislocation density, the same set of experimental stress-strain curves [30] applied in the calibration of the hardening and dynamic recovery parameters were used except that the inelastic strain was allowed to be larger than the critical strain (ε_r) so that the effect of dynamic recrystallization present in the experimental data would be captured.

For $\varepsilon > \varepsilon_r$, the match between model and measurements was obtained through the calibration of Equations 3.26 and 3.27. To calibrate the temperature dependent term K_1, three stress-strain curves at T = 650 ^{o}C, 900 ^{o}C, and 1000 ^{o}C, constant strain rate of $\dot{\varepsilon}$ = 0.01/s, and $\varepsilon > \varepsilon_r$ were used to obtain the best fit to experimental data resulting in c_0 = 124.52 and c_1 = 4.52. Next, to calibrate the strain rate dependent term K_2, three stress-strain curves at $\dot{\varepsilon}$ = 0.001/s, 0.01/s, and 10/s, constant temperature of T = 900 ^{o}C, and $\varepsilon > \varepsilon_r$ in addition to the constraint that K_2 (0.01/s) = 1.0 were used to obtain the best fit to experimental data resulting in c_2 = 1.50, c_3 = 10^{-4}, and c_4 = -0.552. A flow chart of the calibration procedure and the calibrated model are shown in Figures 3.7 and 3.8, respectively. Figure 3.9 shows the unified model predictions for deformation conditions different from those used to calibrate the model yet within the calibration range. As can be seen, the predictions compare reasonably well with the experimental data.

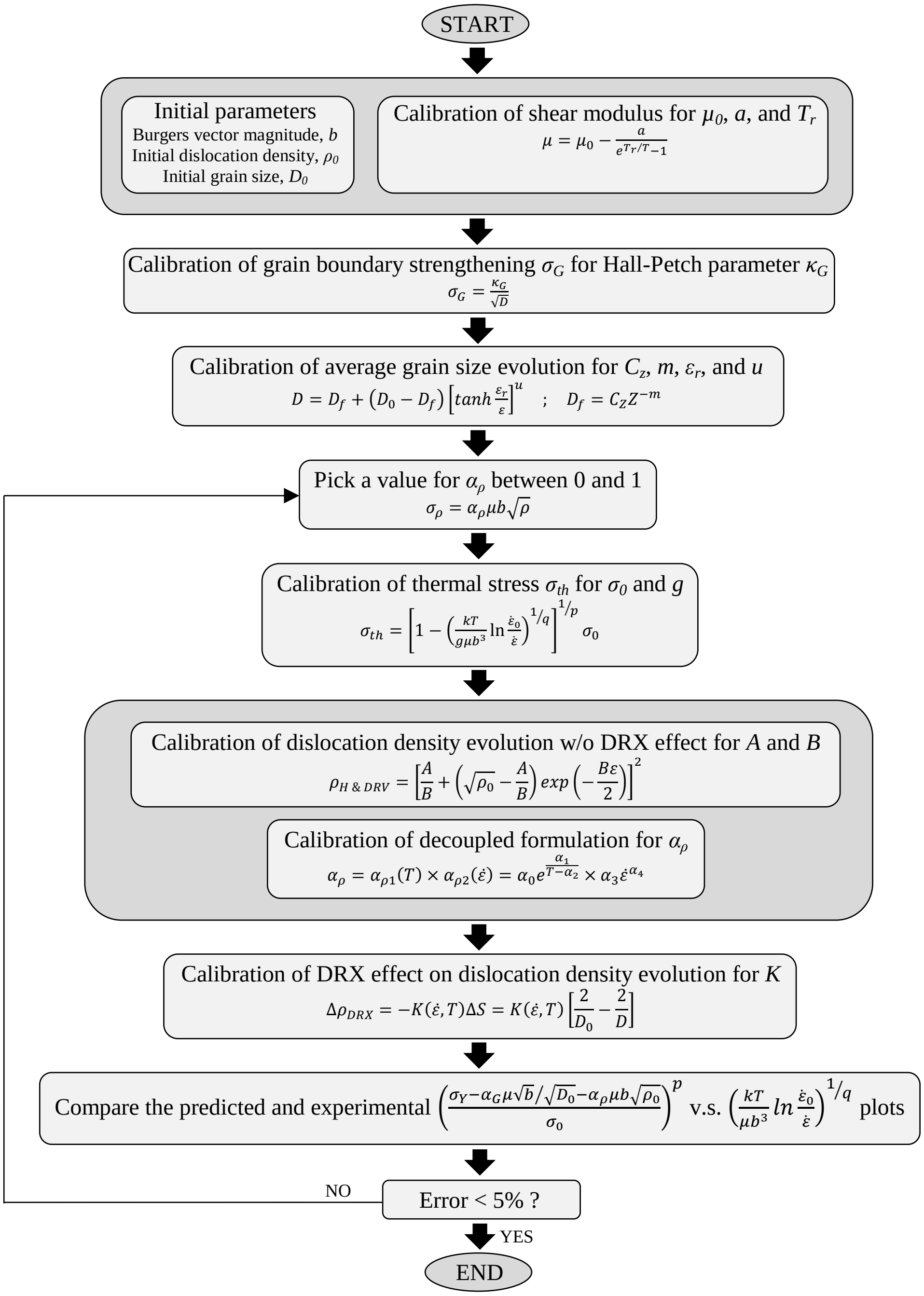

Figure 3.7: Flow chart of calibration procedure.

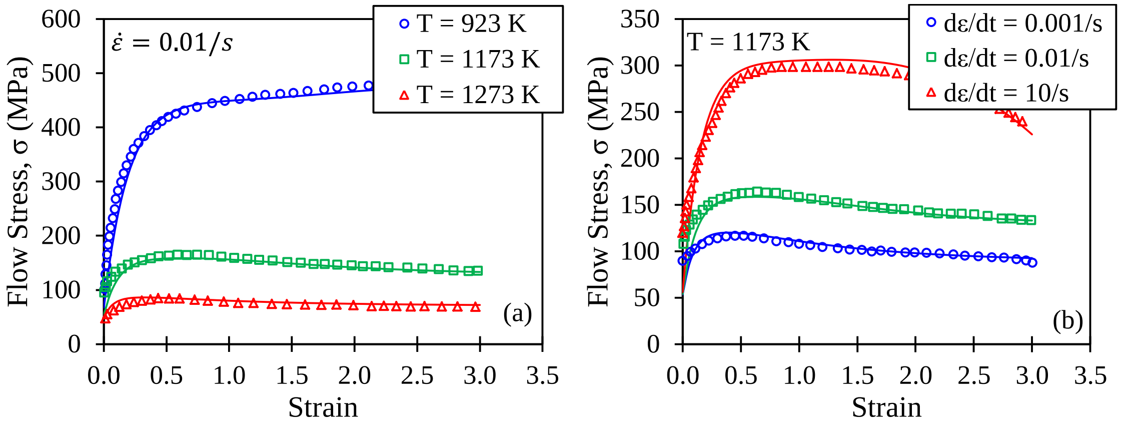

Figure 3.8: Calibrated model (solid lines) compared with experimental data (symbols).

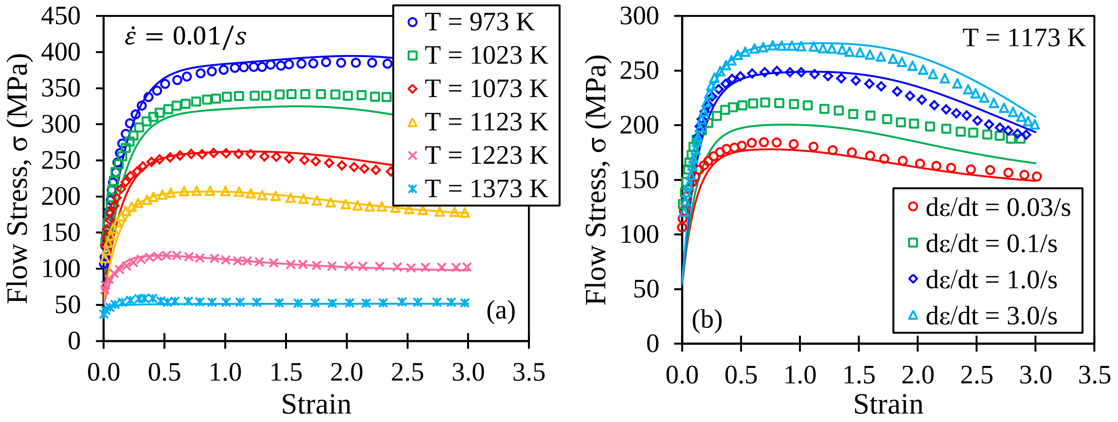

Figure 3.9: Unified model predictions (solid lines) compared with experimental data (symbols) within the calibration range.

3.5 Results and Discussion

3.5.1 Thermal softening and sensitivity of flow stress

Figure 3.10a illustrates the expected decreasing trend in flow stress with increasing deformation temperature (thermal softening) at a constant strain rate. As was seen in Figure 3.9a, the flow stress reaches a plateau for deformation levels above ε = 0.5 and hence the similar thermal softening behavior for different strains shown in Figure 3.10a is reasonable. The unified model reproduces the thermal softening aspect of inelastic deformation quite well as is evident from Figure 3.10a. The thermal sensitivity of flow stress or the thermal softening rate is another feature of the inelastic deformation shown in Figure 3.10b. Here, the variation of thermal sensitivity (essentially the slope of σ vs. T plot in Figure 3.10a or $(\partial\sigma/\partial T)_{\dot{\varepsilon};\varepsilon}$) is shown versus the normalized flow stress rather than the inelastic strain since reliable information on deformation history and pre-strains is usually not available when experimental data are extracted from published literature, which is the case in this investigation. Moreover, the flow stress and the thermal sensitivity on the ordinate were normalized by the shear modulus μ in Figure 3.10b to remove the influence of the temperature dependence of the shear modulus. As seen in Figure 3.10b, the flow stress becomes more sensitive to temperature variations at larger flow stress values. The unified model demonstrates this trend more clearly for σ/μ ratios larger than 4.0 where experimental data show considerable scatter. This scatter is captured in an average sense by the unified model where the thermal sensitivity is more pronounced at larger strains. A likely source for the observed scatter is discussed in the next section. The other observation of significance in Figure 3.10b is the strain independence of thermal sensitivity for small flow stress values, which is evident in the unified model and experimental data.

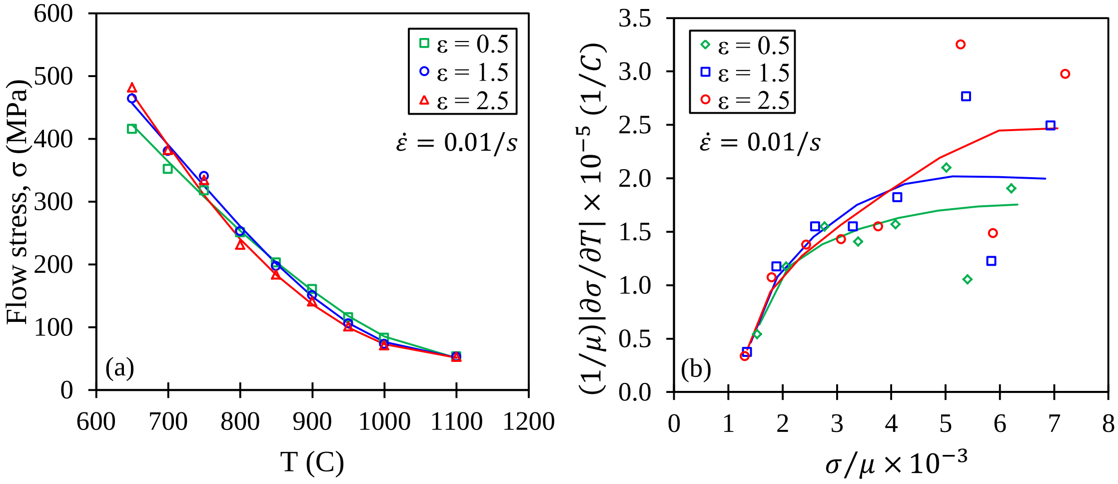

Figure 3.10: Thermal softening (a) and sensitivity (b) of flow stress (symbols-measurements; solid lines-predictions).

3.5.2 Strain rate hardening and sensitivity of flow stress

Figure 3.11a illustrates the expected increasing trend in flow stress with increasing deformation rate (rate hardening) at a constant temperature. As seen in the Figure, the unified model accurately reproduces the rate hardening aspect of inelastic deformation. The slope of σ vs. $\dot{\varepsilon}$ in Figure 3.11a represents the rate sensitivity of flow stress; however, it is often preferred to use $(\partial\sigma/\partial \ln \dot{\varepsilon})_{T,\varepsilon}$ as shown in Figure 3.11b given that the strain rate usually spans several decades. In general, Figure 3.11b suggests that the flow stress will exhibit more pronounced sensitivity to strain rate at larger stress values. While model predictions demonstrate a smooth and more stable trend, a considerable deviation from predictions and especially scatter at large flow stress values is observed in the experimental data. The latter is mainly caused by the inherent uncertainty of experimental data in conjunction with the calculation method used to obtain $(\partial\sigma/\partial \ln \dot{\varepsilon})_{T,\varepsilon}$. The uncertainty in experimental data causes the small deviations in the predictions as shown in Figure 3.11a. Additionally, the instantaneous rate sensitivity or $(\partial\sigma/\partial\ln\dot{\varepsilon})_{T,\varepsilon}$ is approximated by $(\Delta\sigma/\Delta\ln\dot{\varepsilon})_{T,\varepsilon}$ because the stress-strain data are usually measured for a limited number of temperatures and strain rates due to time and cost concerns. The latter is equivalent to replacing model predictions with piecewise linear curves as well as connecting the experimental data points with straight lines in Figure 3.11a. The slope of linear segments like *AB* changes smoothly with strain rate; however, the slope of linear segments like $A^{'}B^{'}$ does not behave similarly due to the uncertainty inherent in the experimental data. When this uncertainty is coupled with the approximation in calculating rate sensitivity, it results in the observed deviations and scatter in Figure 3.11b (this also explains the observed scatter in Figure 3.10b). This is justified noticing that Figure 3.11b was obtained using data that are a decade apart in Figure 3.11a and the deviation and scatter in the rate sensitivity is considerably less wherever there is less deviation between the prediction and experiment in Figure 3.11a.

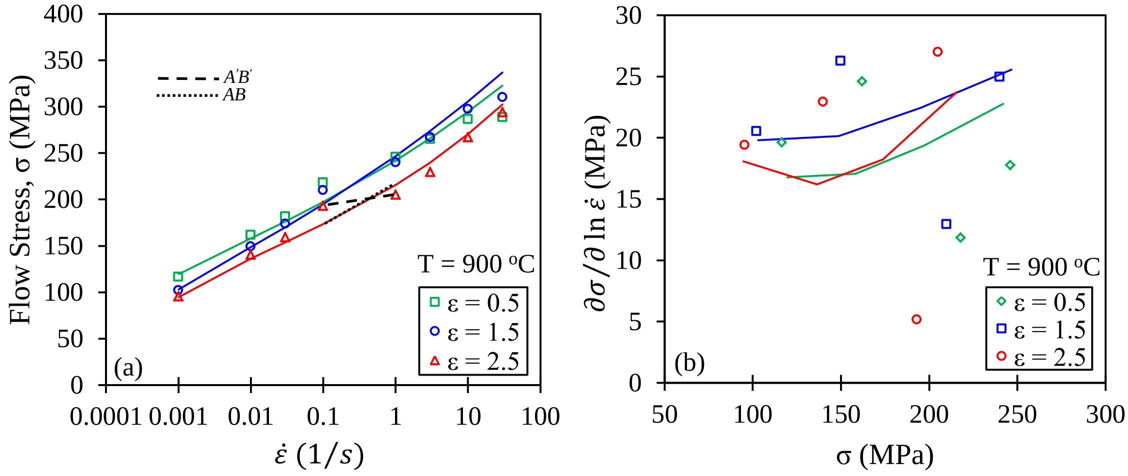

Figure 3.11: Rate hardening (a) and sensitivity (b) of flow stress (symbols-measurements; solid lines-predictions).

3.5.3 Strain hardening rate of flow stress

Figure 3.12a illustrates the anticipated evolution of strain hardening rate during inelastic deformation at a constant temperature and strain rate. The strain hardening rate is defined as the slope (θ) of $\sigma - \varepsilon$ plot; however, it is often represented by $\sigma \times \theta$ [6, 14] for convenience particularly at low strains, i.e. $\varepsilon \in [0. \quad \sim 0.2]$. Moving from region *A* to *B* and ultimately *C* on the $\sigma - \varepsilon$ plot in Figure 3.12b, the slope varies from a large positive value to zero and then an almost constant and comparatively small negative value, respectively. This trend is clearly demonstrated by both the unified model prediction and measurements in Figure 3.12a. The unified model reproduces the strain hardening rate aspect of inelastic deformation reasonably well as is evident from Figure 3.12a.

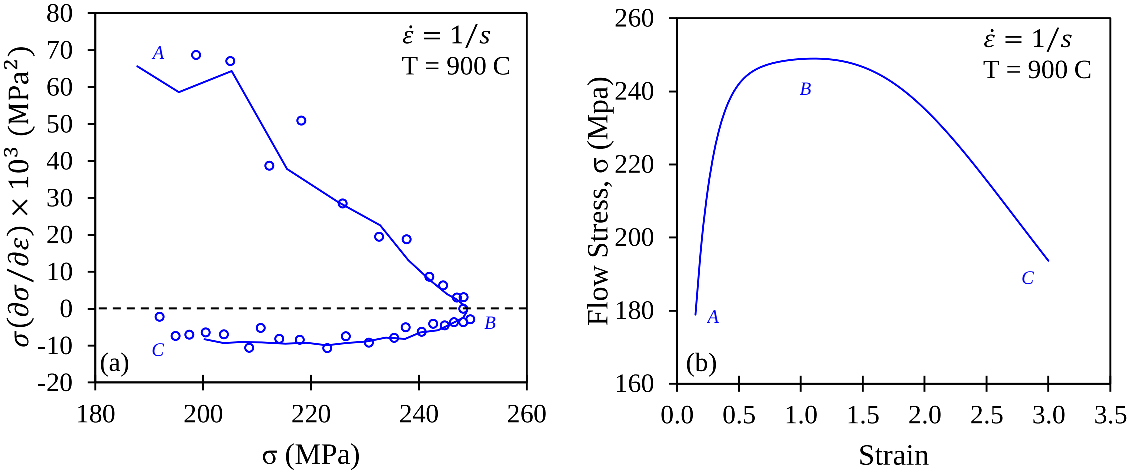

Figure 3.12: Strain hardening rate of flow stress (symbols-measurements; solid line-prediction).

3.5.4 Evolution of microstructure with strain and Zener-Hollomon parameter

Figure 3.13a shows the predictions of average dislocation density and grain size with strain at a constant temperature and strain rate. For $\varepsilon < \varepsilon_r$, the average dislocation density increases with inelastic deformation while the average grain size remains unchanged and equal to the initial value (D_0) of 35 μm in the absence of DRX. Here, it is worth mentioning that although the initial average dislocation density (ρ_0) seems to be zero in Figure 3.13a, it is actually non-zero and equal to 10^{12} m^{-2} which is still a small number relative to the order of numbers on the ordinate. For $\varepsilon \geq \varepsilon_r$, DRX kicks in and produces grain refinement in addition to the decline in the average dislocation density. It should be pointed out that DRV also contributes to dislocation annihilation and attenuation of hardening. The decreasing slope of the $\rho - \varepsilon$ plot shown in Figure 3.13a between ε_r and where the peak density occurs is caused mainly by DRV noting that DRX is still in the infancy in this strain range. For higher strains, DRV would cause leveling off of the $\rho - \varepsilon$ plot if DRX was absent, analogous to the effect of DRV and DRX on the schematic flow stress-strain plot in Figure 3.2.

Figure 3.13b illustrates the effect of the Zener-Hollomon parameter on the average dislocation density and grain size at a constant strain. The temperature increases while the strain rate decreases by moving from right to left on the abscissa in Figure 3.13b. For $Z > Z^*$, the average dislocation density decreases with decreasing Z, i.e. increasing temperature and decreasing strain rate, while the average grain size stays unchanged and is equal to the initial grain size. With $Z \leq Z^*$, the average dislocation density keeps decreasing and grain refinement occurs. The latter implies that for $\varepsilon \geq \varepsilon_r$ only certain combinations of temperature and strain rate (for which $Z \leq Z^*$) will lead to DRX. Although the unified model predictions for the deformed microstructure comply with intuition, they remain to be validated through experiments.

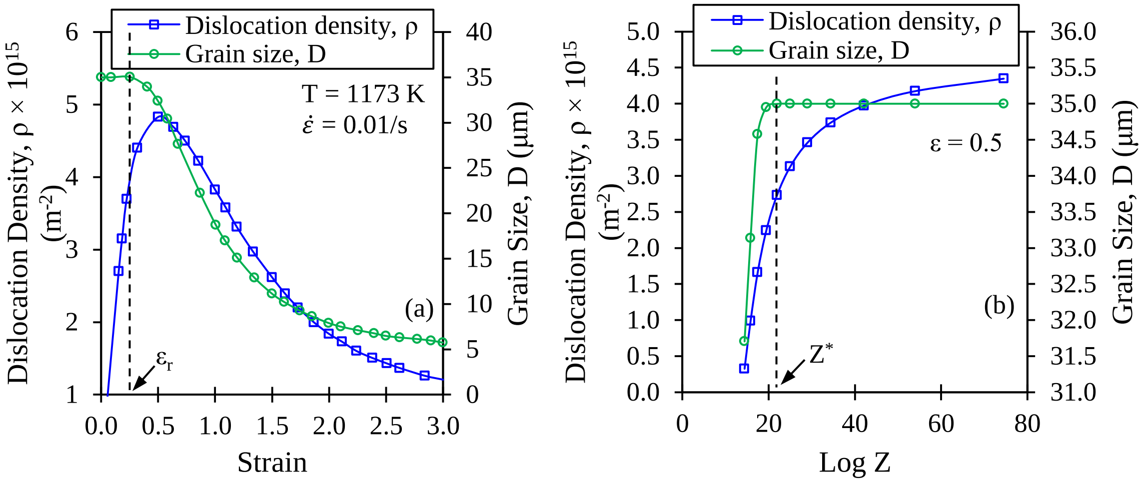

Figure 3.13: The unified model predictions for variations of average dislocation density and grain size with (a) strain and (b) Zener-Hollomon parameter.

3.5.5 Variation of flow stress components with strain and Zener-Hollomon parameter

Figure 3.14a shows the variations of flow stress components versus strain at a constant temperature and strain rate. The dislocation density strengthening component, σ_ρ, shows a similar trend as the average dislocation density (see Figure 3.13a) reflecting the proportional relationship between σ_ρ and $\sqrt{\rho}$ in Equation 3.7. Comparing the trends of average grain size and grain boundary strengthening component, σ_G, it is seen that grain refinement leads to an expected increase in σ_G (reflecting the inverse relationship between σ_G and D in Equation 3.7) due to the fact that finer grain structure is synonymous with higher grain boundary area and ultimately larger contribution from σ_G. The strengthening component caused by short range barriers or thermal stress, σ_{th}, on the other hand, does not change with inelastic strain as was anticipated from Equation 3.4 and the general consensus that strain hardening is mainly associated with the interactions of dislocations and long range barriers.

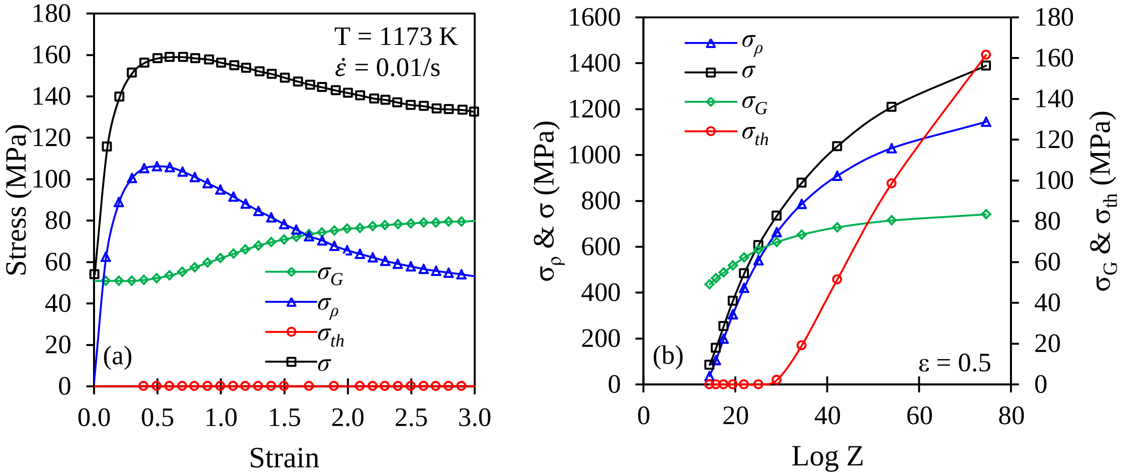

Figure 3.14: Variations of flow stress components with (a) strain and (b) Zener-Hollomon parameter.

The constant strengthening contribution of short range barriers, σ_{th}, is usually non-zero, depending on the deformation temperature or Zener-Hollomon parameter value (see Figure 3.14b), which is not the case in Figure 3.14a due to high deformation temperature. This stems from the principles of activation energy theory, which predicts negligible mechanical contribution by external forces when the thermal contribution is high enough to enable dislocations to overcome short range barriers. Additionally, all three components of flow stress decline with decreasing Zener-Hollomon parameter, i.e. increasing temperature and decreasing strain rate, moving from right to left on the abscissa in Figure 3.14b. It is also evident that dislocation density strengthening is the major component determining the overall flow stress comparing the stress magnitudes on the two ordinates.

3.6 Conclusions

A unified material model explicitly integrating the grain size and dislocation density evolution in the constitutive description was developed based on the dislocation scale kinematics and kinetics of inelastic deformation in conjunction with thermal activation theory. The effects of hardening, dynamic recovery and dynamic recrystallization were collectively captured by developed evolution laws for dislocation density and grain size. The unified model compared reasonably well with experimental data. Different aspects of inelastic deformation including thermal softening and sensitivity, rate hardening and sensitivity, and strain hardening rate were reproduced quite accurately by the unified model. Additionally, the unified model was utilized to analyze the isolated contribution of long and short range barriers on overall flow stress and variation of corresponding stress components with strain, temperature, and strain rate. It turned out that the stress component representing the interaction of individual dislocations with dislocation forests has the major contribution to overall flow stress. The thermal stress did not vary with strain while the athermal stress traced the microstructure evolution with straining. Moreover, both thermal and athermal stresses declined with decreasing Zener-Hollomon parameter, i.e. increasing temperature and decreasing strain rate. Indeed, the thermal stress vanished entirely below a critical value of Zener-Hollomon parameter. The unified model was also used to trace the average dislocation density and grain size evolution with strain and Zener-Hollomon parameter. While the model predictions for microstructure evolution align well with scientific intuition, they remain to be verified through rigorous measurements.

CHAPTER 4

SIMULATION OF CONTINUOUS CHIP FORMATION IN MACHINING OF OFHC COPPER

4.1 Introduction

The objective of this chapter is to implement the unified material model that explicitly accounts for dislocation and microstructure evolution processes as well as dislocation drag as a plausible deformation mechanism applicable at the high strain rates common in orthogonal cutting simulations and to evaluate the performance of the model in predicting the continuous chip formation in machining of OFHC copper.

The proposed unified material model is calibrated and implemented as a user-defined subroutine in AdvantEdge^{TM}, a commercial finite element based machining process modeling and simulation software, and the orthogonal cutting of copper will be simulated. OFHC copper (Cu) has a relatively low yield strength and high thermal conductivity leading to continuous chips in contrast to low thermal conductivity material, such as pure titanium, with yields segmented chip formation (subject of the Chapter 5). The predicted cutting forces are compared with measurements to evaluate its effectiveness. The model is also used to analyze the cutting induced evolution of microstructure and deformation field parameters via microstructure-deformation maps.

4.2 The Unified Model with Dislocation Drag Effect

According to the thermal activation theory [128], the flow stress can be formulated as a superposition of an athermal (σ_a) and a thermal (σ_{th}) stress as shown in

Figure 3.2. The thermal activation controlled deformation is expected to be dominant so long as the deformation rate in the spatial domain of deformation is of the order of 10^3/s or less. However, in machining at high cutting speeds, strain rates of the order of 10^4-10^6/s can occur in the primary shear zone. Therefore, a transition from thermal activation to drag-controlled deformation is expected as the deforming material passes through the primary shear zone. To accommodate such a wide range of strain rates and the corresponding deformation mechanisms, a dislocation drag (σ_d) component is added to the flow stress formulation obtained from thermal activation theory to yield the following constitutive description The effect of dislocation drag is often singled out among other microstructural effects and added as a third component to the formulation derived from thermal activation theory [43-45, 129]:

$$\sigma = \sigma_a + \sigma_{th} + \sigma_d \tag{4.1}$$

Experimental observations suggest that the macroscopic flow stress (σ) typically varies linearly with strain rate over deformation rates where dislocation drag is expected to be the deformation controlling mechanism [42]. Hence, the dislocation drag component (σ_d) of flow stress is formulated as follows:

$$\sigma_d = \alpha_d \dot{\varepsilon} \tag{4.2}$$

where α_d is the dislocation (viscous) drag coefficient.

The athermal component (σ_a) of flow stress is derived from the interaction of mobile dislocations with long range obstacles such as grain boundaries and dislocation forests. This component is formulated as Equations 3.7-3.12 in Chapter 3.

The magnitude of (σ_{th}) depends on the strength of interactions between the mobile dislocations and short-range barriers (e.g. interstitial impurities, substitutional alloying elements, precipitates, other dislocations, etc.), which is formulated as Equation 3.4 in Chapter 3.

4.3 Model Calibration

In this section, the proposed model is calibrated for OFHC copper using stress-strain data available in the literature. The initial grain size, D_0, and dislocation density, ρ_0, were taken to be 62 μm [130] and 10^{10} m^{-2} [131], respectively. The temperature dependent shear modulus of OFHC copper for $T > 100\ K$ is as follows [132]:

$$\mu = 47.095 - \sqrt{0.1429 + (T/60.16)^2} \quad GPa \tag{4.3}$$

In Equation 3.7, the Hall-Petch coefficient, i.e. $\kappa_G = \alpha_G \mu(T)\sqrt{b}$, was taken to be temperature dependent [124] wherein the Burgers vector magnitude (b) is 2.57×10^{-10} m. According to Hou et al. [133] and Smith and Hashemi [134] κ_G is equal to ~100 MPa.$\sqrt{\mu m}$ for annealed OFHC copper at room temperature. Replacing κ_G, μ, and b with appropriate values in the above formulation for the Hall-Petch coefficient, α_G was calculated to be 0.15 and assumed to be temperature independent. The thermal component of flow stress in Equation 3.4 adds five parameters (i.e. $\dot{\varepsilon}_0$, p, q, g_0, and σ_0) to the calibration process. The values for these parameters were taken to be equal to those reported by [3] for annealed OFHC copper and are as follows: $\dot{\varepsilon}_0 = 2 \times 10^{10}/s$, p = 2/3, q = 2.0, σ_0 = 46 MPa, and $k/g_0\mu b^3 = 5 \times 10^{-5}\,K^{-1}$. The strength of dislocation-dislocation forest interactions, α_ρ, is generally temperature and rate dependent and is less than unity (i.e. $0 < \alpha_\rho < 1$). However, the temperature and rate dependency of α_ρ was assumed to be negligible at this stage of the calibration process and initialized to 0.5.

The next step is to calibrate the dislocation density and grain size evolution laws starting with the hardening (A) and recovery (B) parameters of the dislocation density evolution law in Equation 3.9. Following Estrin and Mecking [14], A was considered to be constant and B to be a temperature and strain rate dependent term. This portion of the dislocation density evolution stems from the dislocation production (storage) and annihilation mechanisms in the absence of dynamic recrystallization. This is synonymous with $D = D_0$, $\Delta\rho_{DRX} = 0$, and $\sigma_G = Const.$ To eliminate the effect of DRX on the evolution of dislocation density, only select portions of the experimental stress-strain curves [130] where the plastic strain is less than the critical strain (ε_r) were used. Additionally, since the strain rates in the selected stress-strain data are low, i.e. 0.004 ~ 1/s, the dislocation drag stress component was expected to be negligible, i.e. $\sigma_d = 0$. Moreover, the thermal stress is constant ($\sigma_{th} = Const.$) since it is not strain dependent. For this choice of experimental stress-strain data, the only remaining stress component in the unified model that can vary with strain is σ_ρ. To calibrate A and B_i (i = 1, 2, 3) five stress-strain curves at different temperatures and strain rates were used to obtain the best fit model parameters listed as follow:

$$A = 6.8 \times 10^{8} \quad m^{-1} \tag{4.4}$$

$$B = \left(B_1(T) + B_2(\dot{\varepsilon})\right)^{B_3(T)} \tag{4.5}$$

$$B_1 = 0.052 - 4.87 \times 10^{-5} T \quad (T < 1050\ K) \tag{4.6}$$

$$B_2 = 2.51 \times 10^{-3} \log_{10} \dot{\varepsilon} \tag{4.7}$$

$$B_3 = -0.671 - 8.06 \times 10^{-5} T \tag{4.8}$$

The variation of the final recrystallized grain size, D_f, with temperature and strain rate in Equation 3.11 is modeled as follows [135]:

$$D_f = 10^{(2.64 - 0.17\ \log_{10} Z)}\ \ \mu m \qquad (Z > 10^5\ s^{-1}) \tag{4.9}$$

The activation energy for lattice self-diffusion, Q, and the gas constant, R, were taken as 146.04 kJ/mol [135] and 8.314 J K^{-1} mol^{-1}, respectively, in Equation 3.15 defining the Zener-Hollomon parameter, Z. To calibrate ε_r, the critical strain at which DRX occurs, and u, the DRX rate controlling parameter, in the grain size evolution law, Equation 3.10, the same set of experimental stress-strain curves used in the calibration of the hardening and dynamic recovery parameters were used except that the plastic strain was allowed to exceed the critical strain (ε_r) so that the effect of dynamic recrystallization present in the experimental data would be captured (this is equivalent to $D \neq D_0$, $\Delta\rho_{DRX} \neq 0$, and $\sigma_G \neq Const.$). At the macroscopic scale, dynamic recrystallization manifests itself as a flow softening behavior in the flow stress curves at large plastic strains [136], as shown schematically in Figure 4.1a. The critical strain, ε_r, can be readily determined from the stress-strain curves where the peak stress occurs. Revisiting Equation 3.10, it is seen that for each combination of strain rate and temperature, the DRX rate controlling parameter, u, is the only unknown left in the equation. Knowing ε_f, the strain value at which the dynamic recrystallization effect saturates, u can be uniquely specified using Equation 3.10; ε_f can be determined from the stress-strain curves as the strain at which the flow stress reaches a plateau (see Figure 4.2a). Such a plateau, usually occurring at large strains, is assumed to be associated with saturation of DRX and termination of the grain refinement process (wherein the average grain size is D_f, see Figure 4.2b). Repeating the preceding steps, new sets of ε_r and u can be obtained for different combinations of strain rate and temperature (*see* Figure 4.2c). The data sets thus generated were used to calibrate $\varepsilon_r = \varepsilon_r(\dot{\varepsilon}, T)$ and $u = u(\dot{\varepsilon}, T)$, respectively, by finding a set of ε_i (i = 0…3) and u_j (j = 0…4) parameters that yield the best fit to the ($\dot{\varepsilon}$, T, ε_r) and ($\dot{\varepsilon}$, T, u) data sets (*see* Figure 4.2d). The calibrated results for ε_r and u are as follows:

$$\varepsilon_r = 0.243(\log_{10}\dot{\varepsilon} + 9.5)e^{(-1.86\times10^{-8}/T^{-2.7})} \tag{4.10}$$

$$u = 5.81\times10^{-3}(\log_{10}\dot{\varepsilon} + 20.26)^{2.278}e^{(1.4\times10^{-5}/T^{-1.768})} \tag{4.11}$$

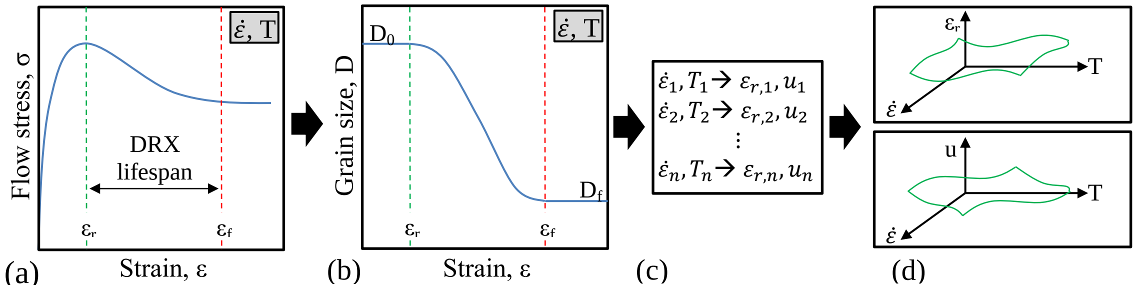

Figure 4.1: Schematic representation of the calibration procedure for the critical strain, ε_r, and the DRX rate controlling parameter, u, in the grain size evolution law.

The viscous drag coefficient, α_d in Equation 4.2, was calibrated using data extracted from the flow stress versus strain curves reported by Tanner and McDowell [130] and Nemat-Nasser and Li [3] (*see* Figure 4.2). Since the data used for calibrating the drag coefficient were obtained from low strain deformations ($\varepsilon<\varepsilon_r$), the effect of DRX on the data is assumed to be negligible. The absence of DRX translates into $D = D_0$ (or $\sigma_G = Const.$) and $\Delta\rho_{DRX} = 0$. Knowing that σ_{th}, σ_ρ, and the dislocation density evolution law in the absence of DRX are all calibrated prior to this step, the dislocation drag stress, σ_d, with only one unknown parameter (i.e. α_d), can be calibrated by tuning the viscous drag coefficient in the modified model to obtain the best fit to the experimental data, which results in α_d = 20 kPa.s. As seen in Figure 4.2, the modification of the unified model by including dislocation drag enables it to capture the intensified strain rate sensitivity above a strain rate of ~10^3/s.

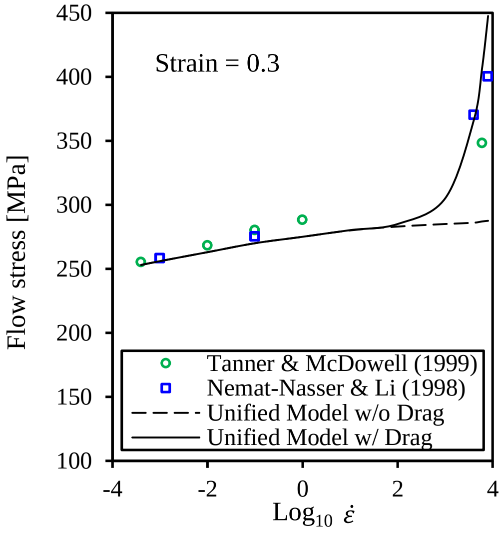

Figure 4.2: Calibration of the dislocation (viscous) drag coefficient in the modified unified model for OFHC Cu using the experimental data obtained from low strain deformations.

The last step is to calibrate the DRX-induced evolution of dislocation density in Equation 3.12. For this, the same set of experimental stress-strain curves used in calibration of the grain size evolution law wherein the plastic strain was allowed to be larger than the critical strain (ε_r) to account for DRX, were used in conjunction with a single cutting force data set obtained from a specific machining condition (v_c = 103.3 m/min, t_u = 213 μm). In fact, the proportionality parameter, *K*, defining the saturation stress level (where hardening, dynamic recovery, and dynamic recrystallization are in equilibrium) could have been calibrated simultaneously with ε_r, the critical strain, and *u*, the DRX rate controlling parameter. However, this calibration was intentionally delayed until this juncture for the following reason. As noted earlier, DRX occurs in large strain deformations (where $\varepsilon > \varepsilon_r$). The strains and strain rates associated with the stress-strain data reported for OFHC Copper are limited to < 1 and ~10^3/s, respectively. However, the deformation in the primary shear zone in high speed cutting operations is characterized by large strains (> 1) and high strain rates (10^4~10^6/s). Experimental observations have confirmed the presence of DRX even under such severe deformation conditions [137]. This suggests that among all the parameters in the unified model, *K* is the one best suited for adjustment in order to capture the evolution of microstructure over the *broad range* of strain rates characteristic of machining. Unfortunately, the stress-strain data generated from dynamic compression experiments (e.g. SHPB) do not replicate the deformation conditions typical of high speed cutting operations, particularly the combination of high strains and high strain rates at which DRX occurs in machining. Therefore, in order to capture the material behavior at high strains and high strain rates, it was decided to use a limited number of cutting force data in conjunction with the available stress-strain data for large strain and low strain rate conditions to calibrate the parameter K in the dislocation density evolution law.

Specifically, the available stress-strain curves corresponding to large strain, low strain rate conditions, used previously for calibration of the grain size evolution law, were used and the parameter K was tuned iteratively to achieve the best fit to the stress-strain data for each combination of strain rate and temperature. In doing so, a set of ($\dot{\varepsilon}$, T, K) data points were generated for the low strain rate deformation regime. Prior to generating similar data points for the large strain, high strain rate deformation regime, the modified material model was implemented as a user-defined material subroutine in the finite element model for orthogonal cutting (details presented in the next section) and cutting forces derived from a single high speed orthogonal cutting simulation were used to tune the parameter K till the predicted forces matched the measured cutting forces. This procedure yielded an extra ($\dot{\varepsilon}$, T, K) data point corresponding to the large strain, high strain rate deformation regime. Next, the generated ($\dot{\varepsilon}$, T, K) data sets were used to calibrate $K = K(\dot{\varepsilon}, T)$ by finding a set of K_j (j = 0…4) parameters that yielded the best fit. The calibrated K_j parameter is given by:

$$K = 31.6 \times 10^{15} (\log_{10} \dot{\varepsilon} + 6.8)^{(-3.86+0.001T)} \quad \mathrm{m}^{-1} \tag{4.12}$$

Figure 4.3 shows a comparison of the calibrated model with and without drag against the experimental flow curves over a range of strains, strain rates, and temperatures. It can be seen that the model with drag follows the experimental data more closely than without drag thereby validating the model.

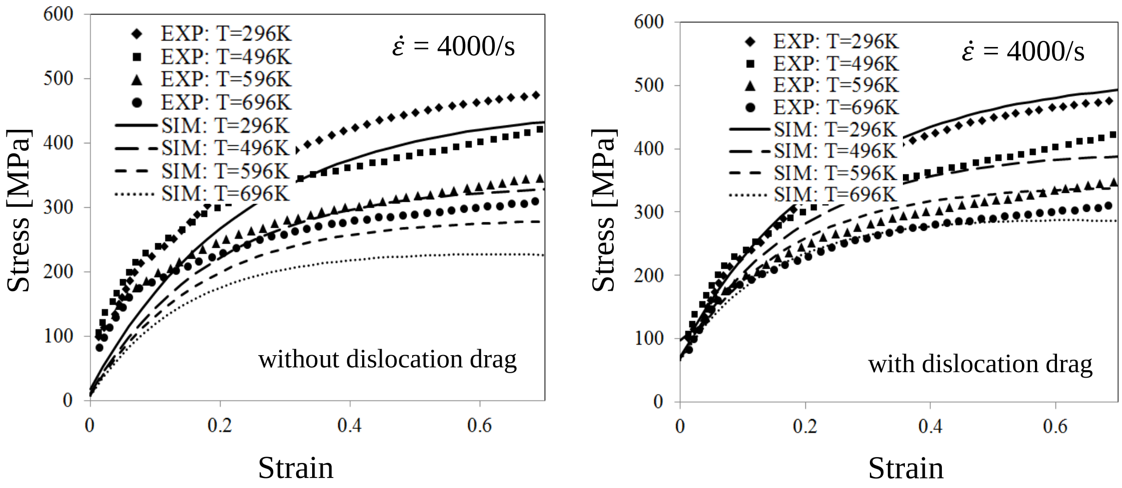

Figure 4.3: Calibrated model (solid and dashed lines) versus experimental data (symbols) taken from Nemat-Nasser and Li [3].

4.4 Finite Element Model of Orthogonal Cutting

To simulate the high speed orthogonal cutting operation, a two-dimensional finite element model was developed in AdvantEdge^{TM}, a specialized commercially available machining simulation software. This software uses a standard Lagrangian formulation combined with a fully automatic adaptive remeshing algorithm to simulate chip formation without any chip separation criterion [74]. The cutting tool was assumed to be rigid and the cutting edge radius was taken to be 20μm, typical of the sharp cutting tools used in the experiments employed for model validation. The contact condition at the tool/chip interface was modeled using the Coulomb friction law. The coefficient of friction, β, at the tool-chip interface was calculated for each simulation case using the measured cutting, F_c, and thrust, F_t, force data and the equation $\beta = (F_t + F_c \tan\alpha)/(F_c - F_t \tan\alpha)$ where α is the rake angle. The simulated length of cut was sufficiently long (L=15mm) to ensure that a steady state cutting condition (*see*

Figure 4.4), defined as unchanging cutting forces and chip morphology, was established. The thermo-mechanical properties of the workpiece material used in the model are listed in Tables 4.1 and 4.2. Constrained by high computation costs, the minimum element size was limited to about 0.02 mm. A user-defined material subroutine was developed using the FORTRAN language to implement the calibrated material model in AdvantEdge^{TM}. Orthogonal cutting simulations were performed to replicate the physical cutting tests carried out by Saldana and Chandrasekar [138] (unpublished data) on high purity copper (99.999%; D_0 = 900μm) with zero rake angle (α), 0.213mm feed (t_u), and a range of cutting speeds (v_c) of 10.3, 26.6, 103.3, 147.6, 265.7 m/min.

Table 4.1: Physical properties of copper [139].

E (GPa)	ν	ρ_m (kg/m^3)	$T_{melting}$ (K)
116	0.34	8960	1356

Table 4.2: Thermal parameters of copper at various temperatures [140, 141].

Temperature (^oK)	Thermal Conductivity (W/m/K)	Specific Heat (J/kg/K)	Thermal Expansion Coefficient (1/K)
200	413	356	15.2×10^{-6}
250	406	374	N/A*
300	401	385	16.5×10^{-6}
350	396	393	N/A*
400	393	399	17.6×10^{-6}
500	386	408	18.3×10^{-6}
600	379	417	18.9×10^{-6}
800	366	433	20.3×10^{-6}

* N/A: Not Available.

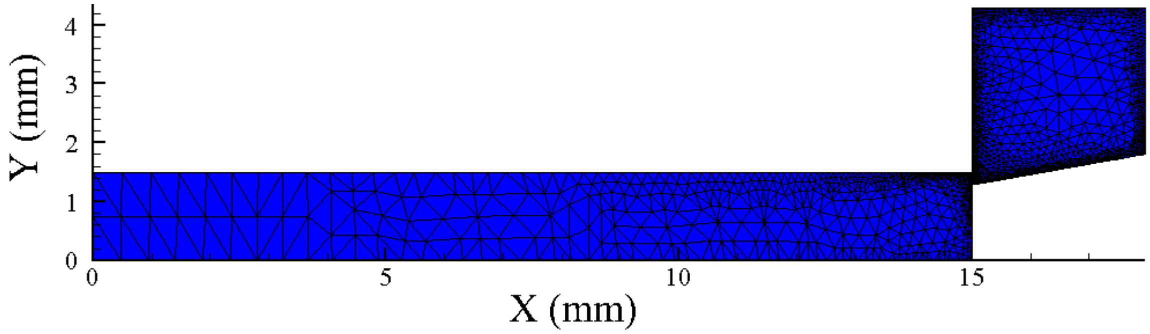

Figure 4.4: Orthogonal cutting model.

4.5 Results and Discussion

4.5.1 Dislocation drag effect on cutting model predictions

Dislocation drag, as discussed before, can have a significant effect on the flow stress at strain rates higher than 10^3-10^4/s, which are common in machining at high cutting speeds. The latter is evident from the simulation results listed in Table 4.3 wherein the cutting force, thrust force, maximum cutting temperature, chip thickness, and shear angle are compared for cases with and without dislocation drag effect. It is seen that model predictions for the case where the dislocation drag effect is taken into account are in better agreement with experimental measurements provided by Chandrasekar and Saldana [138] than the case without dislocation drag. As expected, such difference in cutting model performance with and without dislocation drag effect is negligible for low cutting speed cases.

Table 4.3: Predicted results with and without dislocation drag effect compared with experimental data provided by Chandrasekar and Saldana [138] (cutting speed v_c =103.3 m/min, rake angle α = 0^o and feed t_u = 0.213mm)

	Without Drag	With Drag	Exp. Data
Cutting Force, F_c (N)	2420	1440	1393
Thrust Force, F_t (N)	1380	800	807
Max. Temperature (˚C)	299	244	N/A*
Chip Thickness (mm)	2.5	1.1	1.4
Shear Angle (˚)	4.9	10.9	8.4

* N/A: Not Available.

4.5.2 Predicted vs. measured cutting and thrust forces

Figure 4.5 shows a comparison of the predicted forces with measured values over the range of cutting speeds used in the experiments. Note that the cutting force data for the 103.3 m/min cutting speed was the only one used in calibrating the parameter K in Equation 3.12. It can be seen that the predicted trends and magnitudes of the cutting and thrust forces are in good agreement with the measured values over the entire range of cutting speeds. As expected, the decreasing trend in force magnitudes with cutting speed is due to the increased rate of heat generation associated with higher deformation rates and the accompanying thermal softening effect.

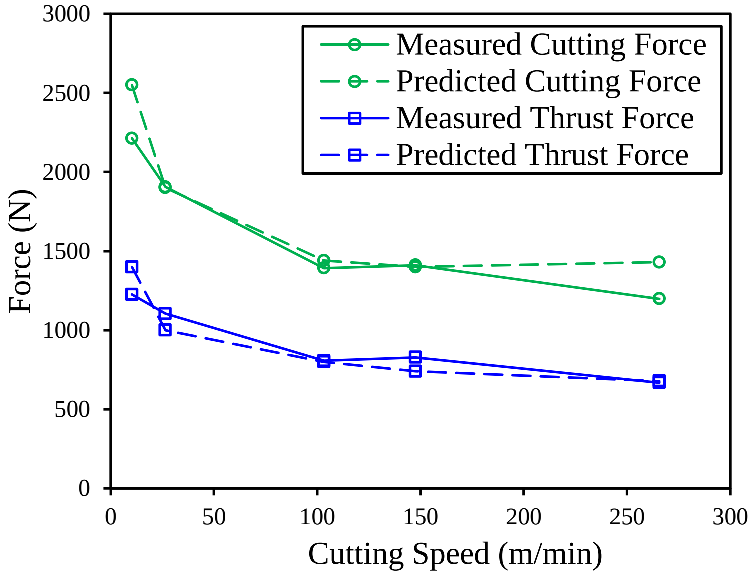

Figure 4.5: Measured [138] and predicted cutting and thrust forces for orthogonal cutting of high purity copper (99.999% pure, D_0 = 900µm) over a broad range of cutting speeds (deformation rates); Rake angle, α, and feed, t_u, are 0^o and 0.213mm, respectively.

It is noted that the unified material model was almost entirely calibrated using stress-strain data for OFHC copper with 99.99% purity level and 62µm initial grain size, D_0. However, the material used in the cutting experiments was a high purity copper (99.999% pure) with 900µm initial grain size. Hence, it seems reasonable to expect the test material to be mechanically softer than the model material. This could explain the higher predicted cutting force value at the lowest cutting speed, where the lower deformation rates and lower cutting temperatures magnify the effect of dislocation interactions with short range barriers such as impurities. However, based on the known physics of continuous DRX and dislocation drag [42], the discrepancy in initial grain size is not expected to have a noticeable effect on DRX or drag.

At the highest cutting speed, the dislocation drag effect is expected to be the dominant deformation controlling mechanism. Since the temperature dependency of dislocation drag [42] can be significant at the high temperatures involved in high speed cutting, the observed discrepancy in the predicted and measured cutting forces at the highest cutting speed may stem from the fact that the drag (viscous) coefficient in Equation 4.2 was taken to be a constant rather than a temperature dependent parameter. Considering the preceding discussion and noticing the broad range of cutting speeds over which the validation was exercised, the fidelity of model predictions appears to be quite good. The chip morphology is another metric used to appraise the validity of the model and the simulations. The model predicts continuous chip morphology, as seen in the contour plots shown in Figures 4.6 and 4.7, which is corroborated by the observations made by Dr. Chandrasekar's group in their experiments on copper [142, 143].

In the following section, the orthogonal cutting model is used to analyze the correlation between process parameters (cutting speed), deformation parameters (strain, strain rate, temperature), and microstructure (grain size and dislocation density) evolution.

4.5.3 Cutting induced evolution of microstructure

The unified material model enables the prediction of microstructure evolution as the deforming material passes through various regions in the deformation field. As seen in Figure 4.6, the model does quite well in predicting the experimentally observed trend [144, 145] of severe grain refinement in machining, ranging from several hundreds of micrometer before the primary shear zone (PSZ) to several tens of micrometer in the PSZ and a few micrometers after the PSZ and well into the chip. Another observation, not readily available through microscopy, is the presence of a gradient in the grain size across the deformed chip thickness. In particular, a deformed layer of submicron (nano-) sized grains is predicted by the model in the secondary shear zone (SSZ) in the vicinity of the tool/chip interface. As the cutting speed increases, the thickness of this highly grain refined layer decreases and the grains become coarser in the chip. At higher deformation rates, the thermally activated annihilation of dislocations is expected to be more pronounced due to the higher cutting temperatures generated, which can explain the predicted grain coarsening. Also shown in Figure 4.6 is the evolution of dislocation density in the deformation field. It is seen that the dislocation density increases as the material approaches the PSZ and, when in the chip, it exhibits a gradient across the thickness. This dislocation density gradient across the chip thickness is consistent with the corresponding gradient in grain size, i.e. the regions with finer grain size are characterized by lower dislocation density due to continuous DRX. The evolutions of grain size and dislocation density are co-occurring events during continuous DRX. The gradient in intensity of DRX from the secondary shear zone to the chip free surface results in comparatively lower dislocation density and finer grains in the secondary shear zone since dislocations are annihilated during DRX leading to grain refinement. This observation is consistent with the underlying physics of continuous DRX [121]. During severe plastic deformation and as DRX occurs, low angle grain boundaries (LABs) nucleate and their misorientation angles grow due to dislocation production and accumulation mechanisms until those LABs transition into high angle grain boundaries (HABs) and form new grains [121].

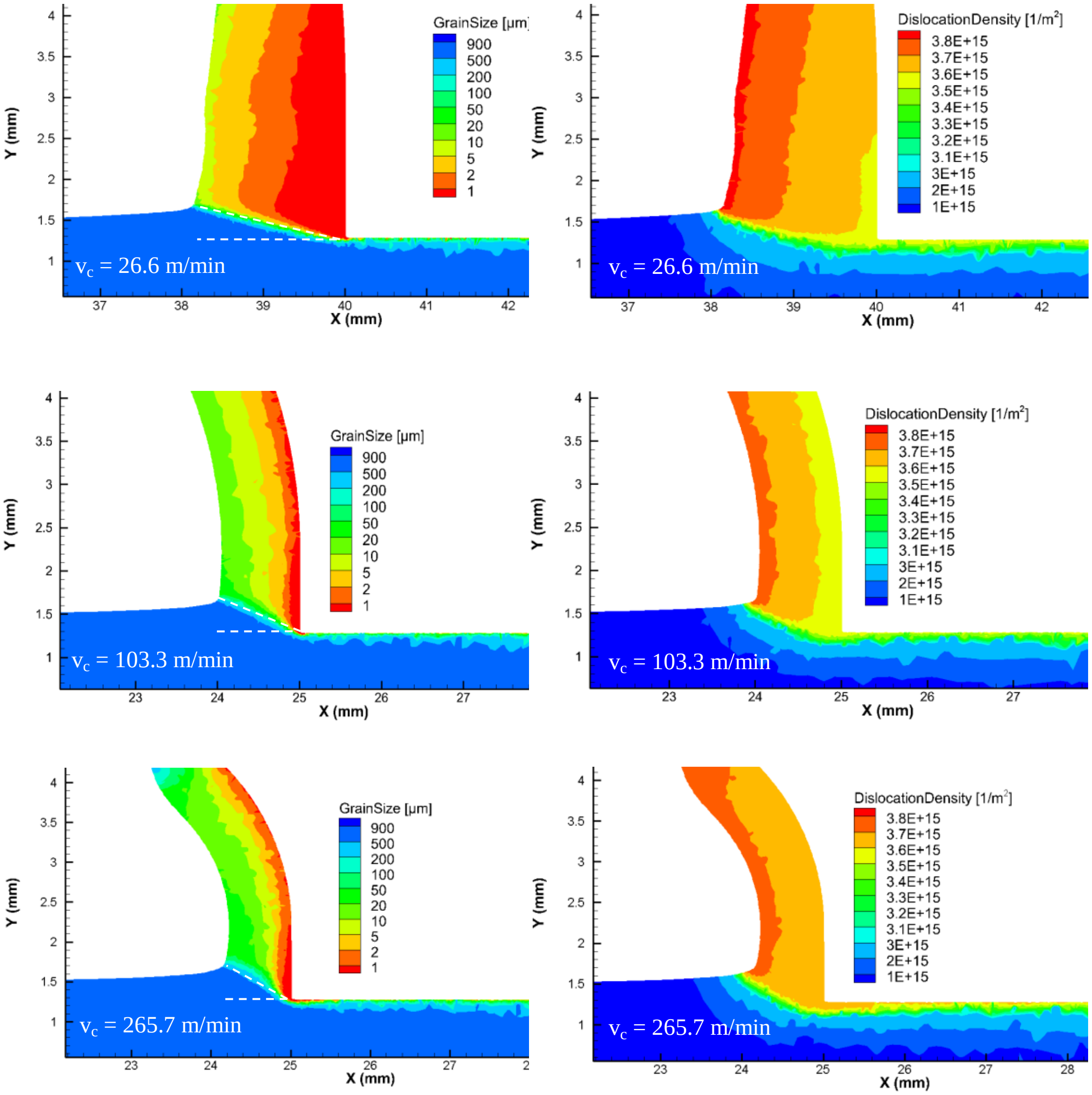

Figure 4.6: Cutting induced evolution of grain size and dislocation density in OFHC copper over a broad range of cutting speeds.

4.5.4 Evolution of deformation parameters in orthogonal cutting

Figures 4.7a, 4.7c, and 4.7e map the strain, strain rate, and temperature evolution in the spatial domain of deformation in orthogonal cutting for a representative case, i.e. 103.3 m/min. The strain field shows that the material is severely deformed as it passes through the PSZ with some additional deformation in the SSZ resulting in a descending gradient in the plastic strain across the chip thickness moving away from the tool/chip interface. The deformation rate peaks at the PSZ, as shown in the strain rate field, while it is not distributed uniformly across this region and reaches its maximum value in the close proximity of the cutting edge. According to the temperature field, the cutting temperature increases as the deforming material passes through the PSZ with additional temperature rise in the proximity of the tool/chip interface in the SSZ due to frictional heat generation. The preceding qualitative observations of the strain, strain rate, and temperature fields are consistent with current understanding of the mechanics of evolution of the deformation field parameters in machining and hence confirm the ability of the complex model to accurately describe expected behavior.

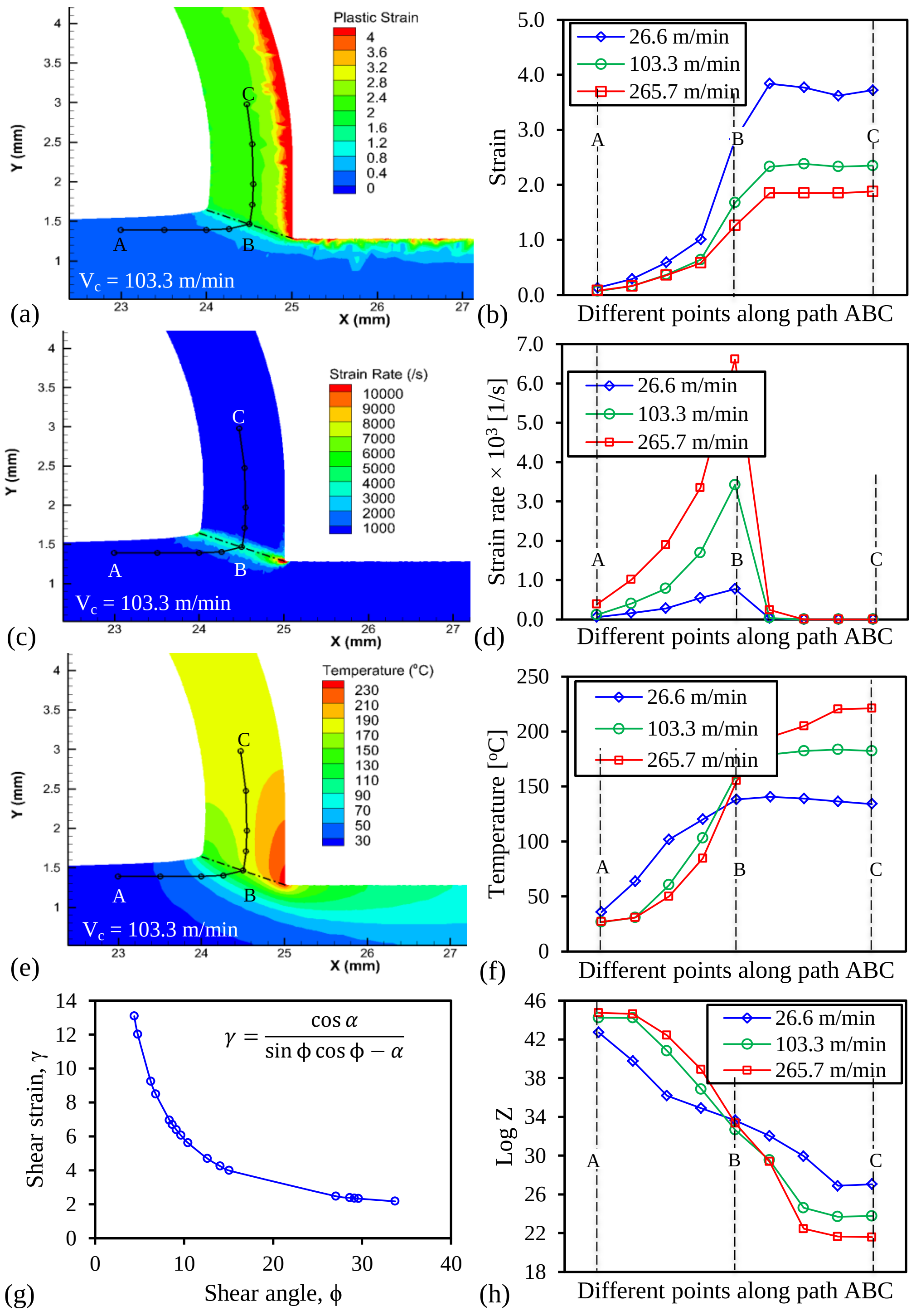

Figure 4.7: Evolution of deformation parameters in orthogonal cutting of high purity copper (rake angle $\alpha = 0^o$ and feed $t_u = 0.213$mm); (a, c, e) representative plastic strain, strain rate, and temperature fields; (b, d, f) evolution of plastic strain, strain rate, and temperature along path ABC for different cutting speeds; (g) shear strain versus shear angle variation according to classical theory of cutting; (h) evolution of Zener-Hollomon parameter along path ABC for different cutting speeds.

It is, however, expected that a quantitative analysis of strain, strain rate, and temperature fields can provide further insight into the evolution of the deformation parameters as the material approaches the PSZ, passes through the PSZ, and enters the chip. To do so and as shown in Figures 4.7a, 4.7c, and 4.7e, an imaginary path *ABC* was defined in the spatial domain of the deformation field and the strain, strain rate, and temperature evolutions from point *A* to point *B* and finally to point *C* were examined. It is seen in Figure 4.7b that the strain gradually increases as it approaches the PSZ, rises sharply as it passes through the PSZ, and, as expected, levels off at an almost constant value in the chip. Another observation made from the model predictions is that the strain level, particularly in the chip, decreases at higher cutting speeds. The latter is also corroborated by the classical theory of cutting mechanics [146] as follows. According to this theory, the average strain, ε, in the chip can be approximated using the following equation

$$\varepsilon = \frac{\gamma}{\sqrt{3}} = \frac{1}{\sqrt{3}} \cdot \frac{\cos \alpha}{\sin \phi \cos(\phi - \alpha)} \tag{4.13}$$

where γ is the average shear strain, α is the tool rake angle, and ϕ is the shear plane angle. For the cases considered here, the rake angle is zero. Hence, the above equation reduces to

$$\varepsilon = \frac{\gamma}{\sqrt{3}} = \frac{1}{\sqrt{3}} \cdot \frac{1}{\sin \phi \cos \phi} \tag{4.14}$$

Plotting the above equation in Figure 4.7g over a wide range of hypothetical shear angles reveals that the average strain in the chip decreases as the shear angle increases. Therefore, it seems that higher cutting speeds should be associated with larger shear angles for the model predictions of the average chip strain in Figure 4.7b to be accurate. Revisiting the contour plots in Figure 4.6 reveals that, indeed, the shear angle is larger for higher cutting speeds. The latter can be explained by noting that higher strain rates and lower cutting temperatures before the PSZ at higher cutting speeds, as seen in Figures 4.7d and 4.7f, render the material mechanically stronger since strain rate hardening is expected to prevail over thermal softening in the region before the PSZ. On the other hand, it is known that mechanically stronger materials deform over larger shear angles in orthogonal cutting. Hence, the higher the cutting speed, the larger the shear angle.

While the presence of higher strain rates in and around the PSZ at higher cutting speeds, as seen in Figure 4.7d, is intuitive, the observed trend in the corresponding temperature gradients, seen in Figure 4.7f, is not and requires further elaboration. According to Figure 4.7f, higher cutting speeds result in lower cutting temperatures before the PSZ while this trend is reversed after the PSZ. A plausible explanation for this observation is as follows. Since the material is severely sheared in the PSZ, a significant amount of heat generation is expected in the PSZ. At low cutting speeds, the heat generated in the PSZ will have more time to diffuse along the *BA* segment of the defined path in Figure 4.7e and hence the temperatures are anticipated to be higher compared to those at high speeds. However, after the PSZ and along the *BC* segment of the defined path, the lack of sufficient time for heat diffusion at high cutting speeds is compensated by more heat generation in the SSZ resulting in higher temperatures over the *BC* segment of the path. Additionally, an inflection point is present in Figure 4.7f. This interesting observation translates into the existence of a location right before the hypothetical shear plane where the cutting temperature does not change, notwithstanding the cutting speed magnitude.

Another interesting observation is the evolution of the Zener-Hollomon (*Z*) parameter in the cutting induced deformation field along the path *ABC*, as shown in Figure 4.7h. This parameter combines the evolution of strain rate and temperature and is larger for lower temperature, higher rate deformation. The latter is obvious from Figure 4.7h where *Log Z* decreases along the path. While higher cutting speeds are associated with larger *Z* values before the PSZ, the corresponding *Z* values are smaller after the PSZ, which is consistent with the observed evolutions of strain rate and the temperature fields along the path in Figures 4.7d and 4.7f and the definition of *Z* in Equation 3.15. It is seen that an inflection point exists on the hypothetical shear plane where the Zener-Hollomon parameter does not change, notwithstanding the cutting speed magnitude. This insight is expected to be beneficial in analyzing the deformed microstructures produced in the deformation zone where an understanding of the combined evolution of strain rate and temperature will be instrumental in explaining the observed microstructures and identifying favorable deformation conditions.

4.5.5 Correlation between cutting induced microstructure and deformation parameters

The generation of maps correlating the process induced microstructure to deformation field parameters is essential for controlled production of a desired microstructure. The cutting process can be used to generate such maps since it can produce a broad range of strains, strain rates, and temperatures in a single pass of the cutting tool [137, 145]. In this context, the model presented in this thesis can be used to easily generate such maps in contrast to costly experiments. As discussed before, the deformation field can be characterized by the set of inelastic strains, ε, and Zener-Hollomon parameter, Z, values at any point in the deformation field. Maps, such as those shown in Figure 4.8, can be produced by tracing the evolution of the deformation parameters, i.e. ε and Z, and the resulting microstructure along imaginary paths, such as *ABC* in Figure 4.7, under different cutting conditions, in this case the cutting speed. It is evident from Figure 4.8 that severe grain refinement occurs in the low Zener-Hollomon and high strain region of the map, which is associated with high dislocation density structure compared to the undeformed material. The versatility of such maps stems from the fact that each value of Zener-Hollomon parameter can be achieved by a wide array of strain rate and temperature combinations, from low strain rate, high temperature deformations to high strain rate, cryogenic processes.

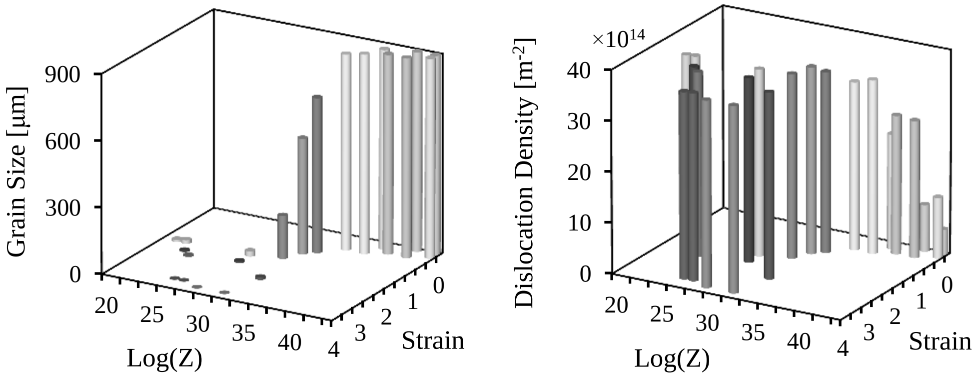

Figure 4.8: Maps correlating the cutting induced microstructure to deformation field parameters.

4.6 Conclusions

A unified material model including the effect of dislocation drag, which is a deformation controlling mechanism at the high strain rates (10^4 - 10^6 s^{-1}) prevalent in high speed cutting operations, was presented and evaluated using orthogonal cutting simulations of OFHC Copper. The model was experimentally validated over a wide range of cutting speeds and shown to yield good results (< 10% error). The model also enabled the prediction of microstructure evolution as the deforming material passes through the deformation field. The model did quite well in predicting the commonly observed trend of severe grain refinement in orthogonal cutting of OFHC Cu. Cutting simulations carried out using the model showed that the strain level in the deforming material decreases, particularly in the chip, as the cutting speed increases, a trend that was found to be in accord with the classical theory of cutting mechanics. It was also shown that higher cutting speeds resulted in lower cutting temperatures in the deforming material before the primary shear zone (PSZ), while this trend is reversed after the PSZ. The latter observation was explained by the mechanics of heat generation and diffusion in and around the PSZ. Additionally, the Zener-Hollomon parameter was found to follow a decreasing trend when moving along a deformation path that passes through the PSZ and into the chip. An inflection point was identified on the shear plane where the Zener-Holloman parameter did not change even with variation in cutting speed. It was also shown that versatile microstructure-deformation maps can be generated from the model. As demonstrated by Chandrasekar and his co-workers [137, 145], such maps can be very useful in identifying the deformation parameters necessary to engineer desired microstructures. In closing, the unified model was developed with the machining application in mind; however, it is expected to be also applicable for other deformation regimes so long as the strains, strain rates, and temperatures do not surpass those seen in machining operations. Moreover, noting that formulations used for the constitutive description and evolution laws are not lattice specific, the unified model should be applicable to other lattice structures so long as the underlying physical mechanisms for inelastic deformation are identical. The applicability of the unified model to other lattice structures remains to be verified.

CHAPTER 5

SIMULATION OF SEGMENTED CHIP FORMATION IN MACHINING OF COMMERCIALLY PURE TITANIUM (CP-Ti)

5.1 Introduction

The objective of this chapter is to implement the unified material model in orthogonal cutting simulations to evaluate the performance of the model in predicting the segmented chip formation in machining of commercially pure titanium (CP-Ti). Comparing with other metals, titanium has the especially low thermal conductivity (< 20 W/m/K) which gives rise to heat accumulation inside the primary shear zone to cause shear band and chip segmentation in machining, which has been observed by Sheikh-Ahmad and Bailey [147]. In order to describe the material behavior of the ultrafine grain structure inside the shear band, the flow stress component due to grain boundary strengthening is modified by introducing the inverse Hall-Petch effect (IHPE) to capture the expected softening of the material below a critical grain size [69].

In this chapter, the unified model is extended to include the inverse Hall-Petch effect. Then the model is calibrated and implemented in a commercial FEM-based machining simulation software AdvantEdge^{TM}, which is used to simulate orthogonal cutting of commercially pure titanium. In order to validate the calibrated unified model, orthogonal cutting experiments are performed to determine the cutting forces and chip morphology, which are compared with the predicted results to evaluate the performance of the proposed unified model in predicting segmented chip formation and associated shear bands.

5.2 The Unified Model with Inverse Hall-Petch Effect

As explained in section 4.2, the flow stress can be formulated as a superposition of an athermal component (σ_a), a thermal component (σ_{th}) and a dislocation drag component (σ_d) as shown in Figure 4.1.

The magnitude of (σ_{th}) depends on the strength of interactions between mobile dislocations and short-range barriers (e.g. interstitial impurities, substitutional alloying elements, precipitates, other dislocations, etc.), which is formulated as Equation 3.4 in Chapter 3.

The athermal component (σ_a) of flow stress is derived from the interaction of mobile dislocations with long range obstacles such as grain boundaries and dislocation forests. This component is formulated as Equations 3.7 in Chapter 3.

For the grain boundary contribution to the athermal component (σ_a), the coefficient, κ_G, in Equation 3.7, is assumed to be independent of grain size in the micron-sized grain structure regime where the conventional Hall-Petch effect dominates. As grain size is smaller than the critical grain size for initiating the IHPE, D_{IHPE}, the flow stress decreases with decreasing grain size. This phenomenon is often termed the Inverse Hall-Petch effect (IHPE). The related experimental evidences and potential physical interpretations about IHPE have been elaborated in Section 2.4.

The coefficient, κ_G, which describes the strength of the dislocation-grain boundary interaction, is modeled using the following function, which replaces Equation 3.14, in order to capture the softening in flow stress due to the IHPE when the grain size is smaller than a critical value:

$$\kappa_G = \alpha_G \mu(T)\sqrt{b}\, tanh\left(\frac{d}{D^{-0.5}}\right)^{v} \tag{5.1}$$

where d and v are temperature dependent fitting parameters controlling the critical grain size, D_{IHPE}, and the softening rate, respectively. The evolution of grain size, D, due to DRX during inelastic deformation is formulated as Equations 3.10 and 3.11. Described by Equation 5.1, the strength of grain boundaries is constant when $D > D_{IHPE}$ and becomes weaker when $D < D_{IHPE}$ due to the IHPE. Based on experimental observations [61, 71] of the influence of temperature on the IHPE, d and v have been modeled as functions of temperature, which will be discussed in the following section.

For the contribution of dislocation forests to the athermal component (σ_a), the evolution law for dislocation density is derived as follows:

$$\rho = \rho_R + (\rho_{H\,\&\,DRV} - \rho_R)\left(\frac{D}{D_o}\right)^{0.5} \tag{5.2}$$

where $\rho_{H\,\&\,DRV}$ is the dislocation density in the absence of DRX and has a closed-form expression (Equation 3.9) for the evolution law. As plastic deformation proceeds, dislocations are consumed to form new grain boundaries during the DRX process, which is expressed by Equation 5.2. ρ_R represents the dislocation density corresponding to the fully recrystallized grain structure.

Finally, the dislocation drag component of flow stress is formulated as Equation 4.2 given in Chapter 4.

5.3 Model Calibration

In this section, the proposed model is calibrated for CP-Ti with initial grain size of ~40 μm using the following procedure. The material parameters for the thermal component of flow stress can be found in literature for CP-Ti with initial grain size of 40 μm [148] and are listed in Table 5.1.

Table 5.1: Material parameters for the thermal component of constitutive model [148].

σ_0 (MPa)	k/g_0 (/K)	b (m)	$\dot{\boldsymbol{\varepsilon}}_{\mathbf{0}}$ (/s)	p	q
140	4.8×10^{-5}	2.95×10^{-10}	4×10^{8}	2/3	2

The variation of the shear modulus μ with temperature was fitted to the available experimental data [149, 150] shown in Figure 5.1 as follows:

$$\mu = 48.66 - 0.03223T \;\; GPa \quad (273\,K < T < 1200\,K) \tag{5.3}$$

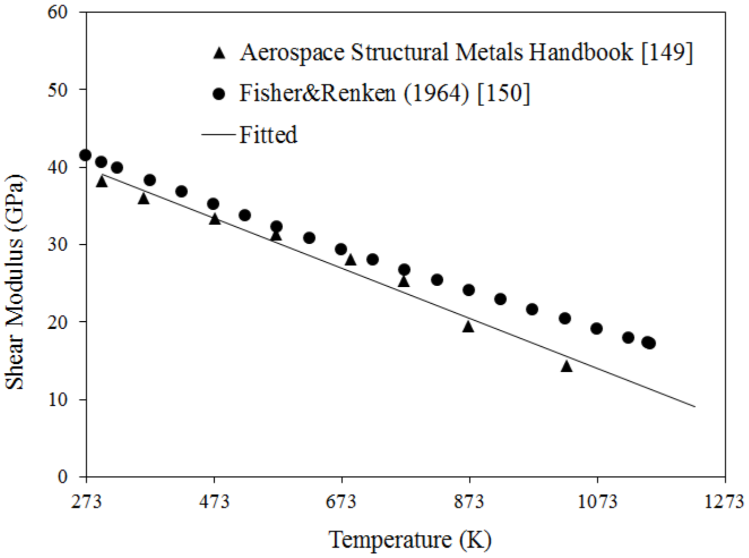

Figure 5.1: Temperature dependent shear modulus (symbols-measured; solid line-fitted).

After fitting the experimental data for CP-Ti [151] shown in Figure 5.2 with Equation 3.10, the variation of final recrystallized grain size, D_f, with the Zener-Hollomon parameter was obtained as,

$$D_f = (5.1 \times Z^{-6.3}) \times 10^7 \ \mu m \quad (Z > 10^{10}\ s^{-1}) \tag{5.4}$$

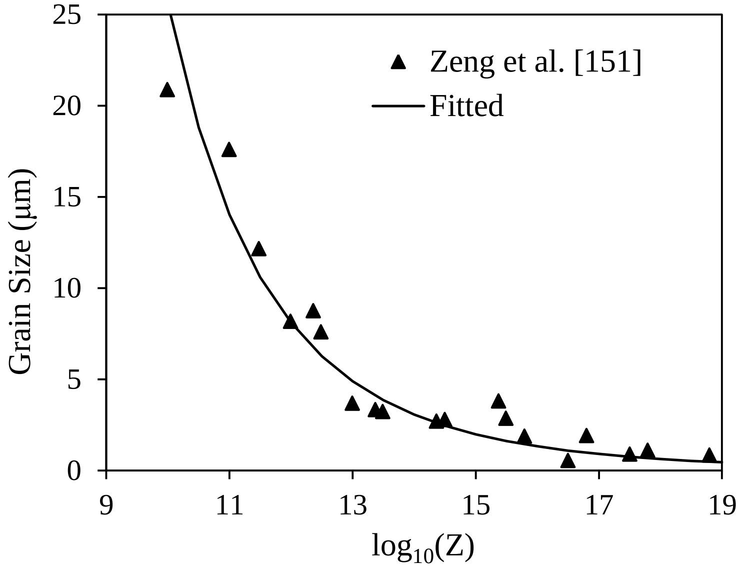

Figure 5.2: Variation of final grain size with Zener-Hollomon parameter (symbols-measured; solid line-fitted).

The activation energy for lattice self-diffusion, Q, and the gas constant, R, in Equation 3.15 defining the Zener-Hollomon parameter, Z, were taken as 146.04 kJ/mol and 8.314 J/K/mol [152], respectively.

To calibrate the parameter, κ_G, which describes the strength of dislocation-grain boundary interaction, the constant coefficient, α_G, in Equation 5.1 was calibrated as 0.4544 using the experimental data prior to the initiation of the IHPE as shown in Figure 5.3. As grains are refined by DRX to be smaller than the critical grain size, D_{IHPE}, the

IHPE dominates as seen in Figure 5.3 and is controlled by the parameters *d* and *v*, which are assumed to have the following forms:

$$d = \frac{1}{0.1 + k_d(T - 293)} \quad \mu m^{-0.5} \quad (T > 293\ K) \tag{5.5}$$

$$v = 2 + k_v(T - 293) \quad (T > 293\ K) \tag{5.6}$$

where k_d and k_v are the fitting parameters that govern the temperature dependency of the parameters *d* and *v*. Due to the limited availability of experimental flow stress curves for CP-Ti with nano-sized grains at elevated temperatures, *d* and *v* were calibrated using machining data as discussed in the next section. Also, considering that the IHPE appears only when the grain size is less than a critical value, the parameters, *d* and *v*, will not influence the following calibration steps.

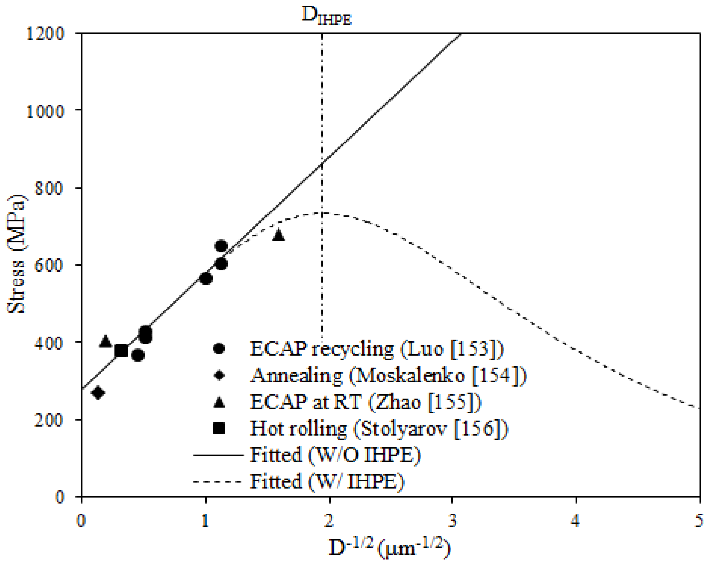

Figure 5.3: Calibrated model (solid straight line) compared with experimental data for CP-Ti (symbols) and schematic representation of IHPE on a flow curve (dashed line) with ultrafine grain structure.

To calibrate the dislocation forest component of the flow stress model, σ_ρ, the dislocation-dislocation forest interaction term, α_ρ, is taken to be 0.5 for most metals [157]. The initial dislocation density, ρ_0, was taken to be 10^{12} m^{-2} for the annealed condition [158]. The next step is to calibrate the hardening (*A*) and recovery (*B*) parameters in the dislocation density evolution law given by Equation 3.9 against the experimental stress-strain curves reported by Zeng et al. [159] (see Figure 5.5). This portion of dislocation density evolution stems from the dislocation production (storage) and annihilation mechanisms that are active in the absence of dynamic recrystallization and is synonymous with $D = D_0$, and $\sigma_G = Constant$. To eliminate the effect of DRX on the evolution of dislocation density, only the portions of the experimental stress-strain curves [159] wherein the inelastic strain is less than the critical strain (ε_r) were used as shown in Figure 3.2. Additionally, since the strain rates in the selected stress-strain data are quite low, i.e. 0.001 ~ 0.1/s, the dislocation drag stress component is expected to be negligible, i.e. $\sigma_d = 0$. Moreover, the thermal stress is constant ($\sigma_{th} = Const.$) since it is not strain dependent. For the experimental stress-strain data selected, the only remaining stress component in the unified model that can vary with strain is σ_ρ. To calibrate *A* and *B*, the five stress-strain curves at different temperatures and strain rates (see Figure 5.5) were used to obtain the best fit to experimental data resulting in the model parameters as follows:

$$A = 1.2 \times 10^{9} \quad m^{-1} \tag{5.7}$$

$$B = (15.66 + 0.09T)\, exp\left[(-0.2879 - 0.00007T)\log_{10}\left(\frac{\dot{\varepsilon}}{10^{-4}}\right)\right] \quad m^{-1} \tag{5.8}$$

To calibrate ε_r, the critical strain above which DRX occurs, and u, the DRX rate controlling parameter, in the grain size evolution law, i.e. Equation 3.10, the same set of experimental stress-strain curves used in the calibration of the hardening and dynamic recovery parameters (A and B) were used except that the inelastic strain was allowed to be larger than the critical strain (ε_r) so that the effect of dynamic recrystallization present in the experimental data would be captured (this is synonymous with $D \neq D_0$ and $\sigma_G \neq$ *Const.*). At a macroscopic scale, the dynamic recrystallization manifests itself as a flow softening effect at large inelastic strains [136] as shown in Figure 5.4a. The critical strain, ε_r, can be readily determined from the stress-strain curves where the peak stress occurs. Considering this aspect and revisiting Equation 3.10, it is seen that for each combination of strain rate and temperature, the DRX rate controlling parameter, u, is the only unknown left in the grain size evolution law. Knowing ε_f, the strain value at and above which the dynamic recrystallization effect saturates, u can be uniquely specified using Equation 3.10. The quantity ε_f can be determined from the stress-strain curves by finding the strain value at which the flow stress reaches a plateau (Figure 5.4a). Such a plateau, occurring at large strains, is associated with DRX saturation and termination of grain refinement (wherein the average grain size is D_f, *see* Figure 5.4b). Based on the above considerations, the parameters, ε_r and u, were calibrated (see Figure 5.5) as follows:

$$\varepsilon_r = 0.237 + 0.000724\left[\log_{10}\left(\frac{\dot{\varepsilon}}{10^{-4}}\right)\right]^{2.72} \tag{5.9}$$

$$u = 7.4 - 2.44\left[\log_{10}\left(\frac{\dot{\varepsilon}}{10^{-4}}\right)\right]^{-1.14} \tag{5.10}$$

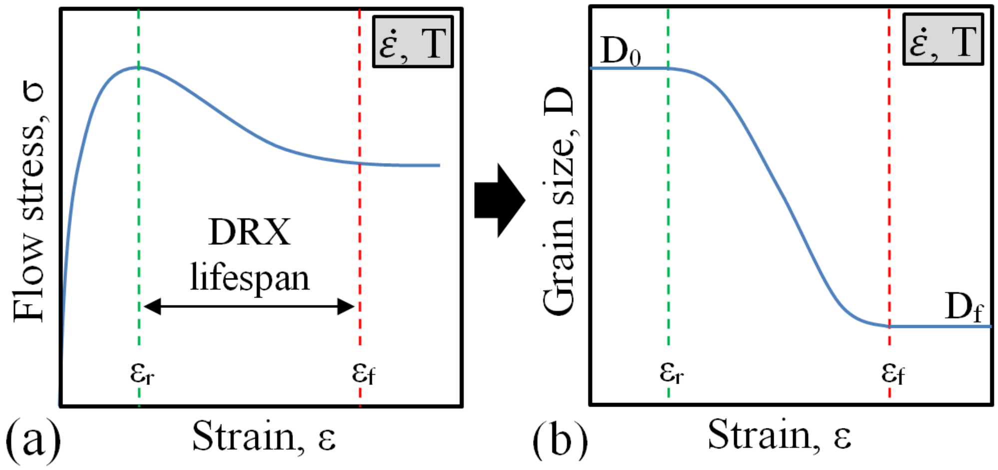

Figure 5.4: Schematic representation of the calibration procedure for the critical strain, ε_r, and the DRX rate controlling parameter, u, in the grain size evolution law.

After calibrating the previous flow stress components, the dislocation density with fully recrystallized grain structure, ρ_R, can be calculated by matching the simulated flow stress with $D = D_f$ and $\rho = \rho_R$ to the experimental data at large strains. Using this procedure, the calibrated ρ_R is found to be an almost constant value of 4×10^{14} m^{-2}.

Figure 5.6 shows the model validation against experimental data [159] where it can be seen that the calibrated unified model is in good agreement with the measured stress-strain response of CP-Ti over a range of strains, strain rates (10^{-3} ~ 0.1 s^{-1}), and temperatures (673 ~ 973 K).

The coefficient of dislocation (viscous) drag, which only operates at high strain rates, α_d, was taken to be 4.5 kPa·s for CP-Ti, as reported by Wulf [160].

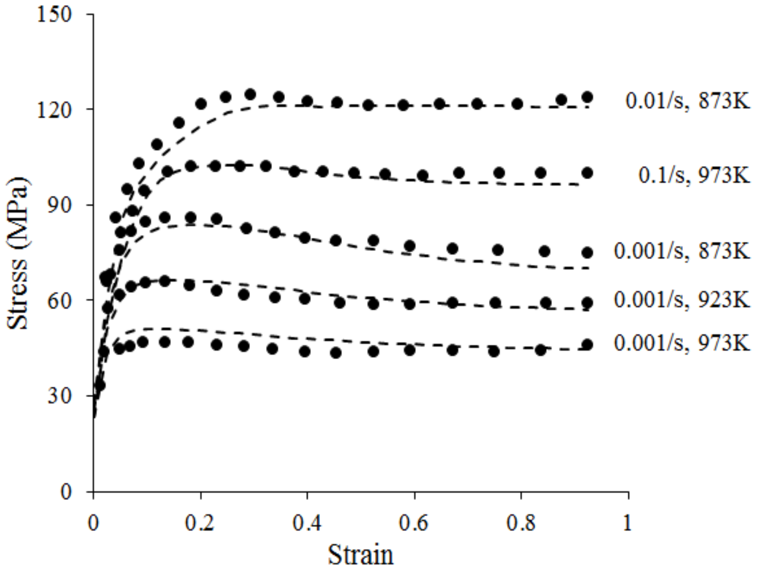

Figure 5.5: Comparison of the calibrated stress-strain curves (dashed lines) and experimental data [159] (symbols) for CP-Ti.

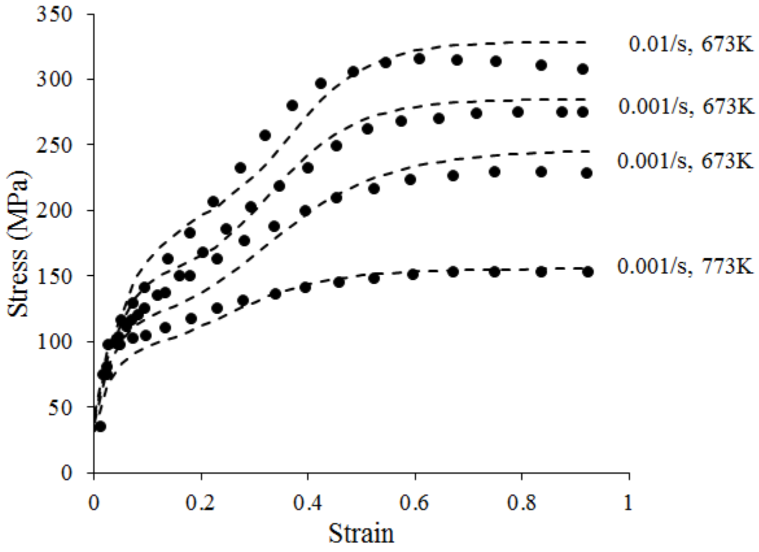

Figure 5.6: Validation of the simulated stress-strain curves (dashed lines) against experimental data [159] (symbols) for CP-Ti.

5.4 Experimental Details

All orthogonal cutting experiments were performed using commercial purity grade 2 titanium (98.9% Ti). The material was acquired from McMaster-Carr as 31.75 mm diameter bar stock in the annealed condition adhering to ASTM B348. The as-received microstructure consisted of an equiaxed α-phase with an average grain diameter of 40 μm as shown in Figure 5.7.

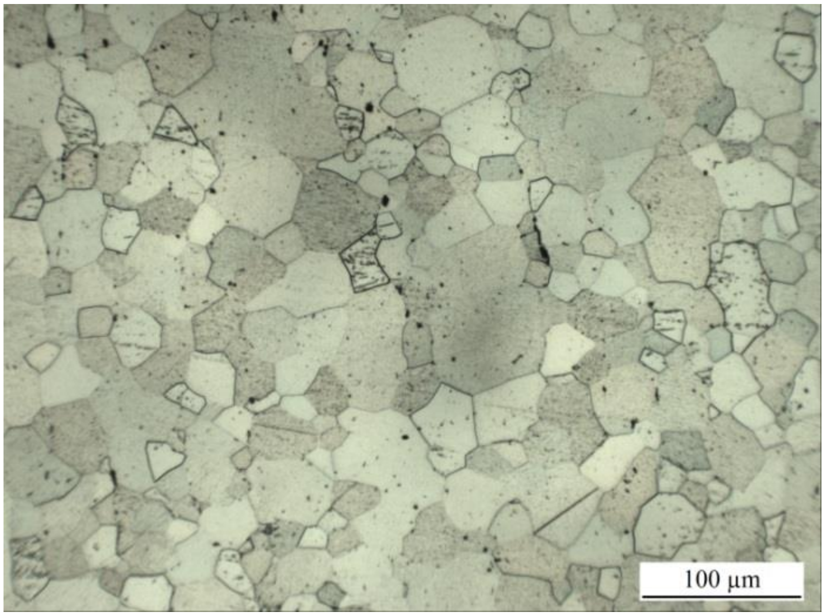

Figure 5.7: Microstructure of as-received CP-Ti (grade 2) workpiece.

Orthogonal cutting experiments were performed on a Hardinge T-42 SP CNC lathe. Tubular specimens were manufactured from bar stock with an outer diameter of 30.48 mm. To establish the plane strain deformation condition, the wall thickness was taken to be 2 mm, which is much larger than the feeds used in the experiments. All experiments were performed using uncoated carbide inserts with an up-sharp cutting edge

(Kennametal TCMW3251). To minimize tool wear effects, a new insert was used in each experiment. A constant rake angle of 0° was used for all experiments. No cutting fluid was applied. After each cut, the tool was retracted from the workpiece at a rate of 16 $m \cdot rev^{-1}$ and the chip was collected in a water tank to preserve the microstructure present soon after cutting. Cutting force, F_c, and thrust force, F_t, were measured using a piezoelectric force dynamometer (Kistler Model 9257B).

To probe a wide range of strains and strain rates, three feeds (0.1, 0.2, 0.3 mm) and five cutting speeds (20, 60, 100, 140, 180 $m \cdot min^{-1}$) were utilized. All experiments were duplicated at least once to ensure repeatability. Conditions producing cutting forces with excessive variation were repeated additionally.

Chips were collected and prepared for metallography. Produced chips were cold mounted longitudinally in epoxy, ground to the chip mid-section and polished to a 0.05μm finish. Kroll's reagent, a mixture of 1 ml hydrofluoric acid (HF, 40%), 2 ml nitric acid (HNO_3, 40%) and 247 ml de-ionized water, was swabbed on each sample for 2 minutes to etch and reveal the microstructure.

5.5 Finite Element Model

To simulate the orthogonal cutting operation, a two-dimensional finite element model was developed in AdvantEdge^{TM}, a specialized commercially available machining simulation software. This software uses a standard Lagrangian formulation combined with a fully automatic adaptive remeshing algorithm to simulate chip formation without any chip separation criterion [74].

The workpiece material behavior is described by the calibrated unified model which was implemented in AdvantEdge^{TM} via a user-defined material subroutine coded in FORTRAN. Moreover, the thermo-mechanical properties of the workpiece material, listed in Tables 5.2 and 5.3, were included in the model.

Table 5.2: Physical properties of CP-Ti [139].

E (GPa)	ν	ρ_m (kg/m^3)	$T_{melting}$ (K)
120	0.361	4507	1977

Table 5.3: Thermal parameters of CP-Ti at various temperatures [161-163].

Temperature (K)	Thermal Conductivity (W/m/K)	Specific Heat (J/kg/K)	Thermal Expansion Coefficient (1/K)
300	21.5	547.7	9.238×10^{-6}
400	20.0	597.4	
500	19.0	618.4	
600	18.3	628.0	
700	17.7	632.4	
800	17.3	633.9	
900	17.0	633.7	

The cutting tool material and geometry used in the experiments are listed in Table 5.4 and were input to the model. Additionally, the cutting tool was assumed to be rigid in the model due to its higher stiffness compared to the workpiece. The contact condition at the tool/chip interface was modeled using the Coulomb friction law. As shown in Table 5.5, the coefficient of friction, β, at the tool-chip interface for each simulation was calculated using the measured F_c and F_t and the classic equation $\beta = (F_t + F_c \tan\alpha)/(F_c - F_t \tan\alpha)$ where α is the rake angle.

Table 5.4: Cutting tool material and geometry.

Material	Uncoated carbide
Rake angle (˚)	0
Clearance angle (˚)	7
Cutting edge radius (μm)	10

Table 5.5: Friction coefficients used in the simulations.

	t_u=0.1 mm	t_u=0.2 mm	t_u=0.3 mm
v_c=20 m/min	0.63	0.50	0.44
v_c=60 m/min	0.52	0.40	0.34
v_c=100 m/min	0.49	0.37	0.30
v_c=140 m/min	0.46	0.31	0.28
v_c=180 m/min	0.42	0.29	0.27

The length of cut was long enough to ensure that the steady state cutting condition, wherein the cutting forces and chip morphology do not change with further progress of cutting, is established. A sensitivity analysis was conducted to ensure that the number of elements (50,000) is sufficient and the minimum element size (0.002mm) is fine enough to yield accurate predictions.

5.6 Experimental and Numerical Results

5.6.1 Inverse Hall-Petch Effect (IHPE) model calibration

In order to calibrate the temperature dependent parameters d and v, seven finite element simulations were set up with different values for the parameters k_d and k_v in Equations 5.5 and 5.6, according to Table 5.6. Figure 5.8 shows the grain boundary components of flow stress with different combinations of k_d and k_v at an elevated temperature of 600K. It shows that the critical grain size for initiating the IHPE, D_{IHPE}, is controlled by k_d while the softening rate changes with k_v. Such variation induced by IHPE decreases with decreasing temperature as shown in Figure 5.9. At room temperature, D_{IHPE} is at 10 nm for any combination of k_d and k_v, which is in agreement with Conrad and Narayan's study [51] for various metals. It is also noted that D_{IHPE} for Simulation-1 is independent of temperature and is always equal to 10 nm. Considering that the grain size in machining can rarely be refined to 10 nm, Simulation-1 can be considered to represent the case without IHPE.

The cutting speed and feed used in the seven numerical simulation cases specified in Table 5.6 were 100 m/min and 0.2 mm, respectively. Simulation results are evaluated by comparing the predicted forces and chip geometries to the corresponding experimental results. The combination of k_d and k_v yielding the best overall results is selected to complete the model calibration procedure.

Table 5.6: Configurations of the numerical simulations.

Simulation	k_d	k_v
1	0	0
2	0.0002	0
3	0.0002	0.005
4	0.0002	0.01
5	0.0004	0
6	0.0004	0.005
7	0.0004	0.01

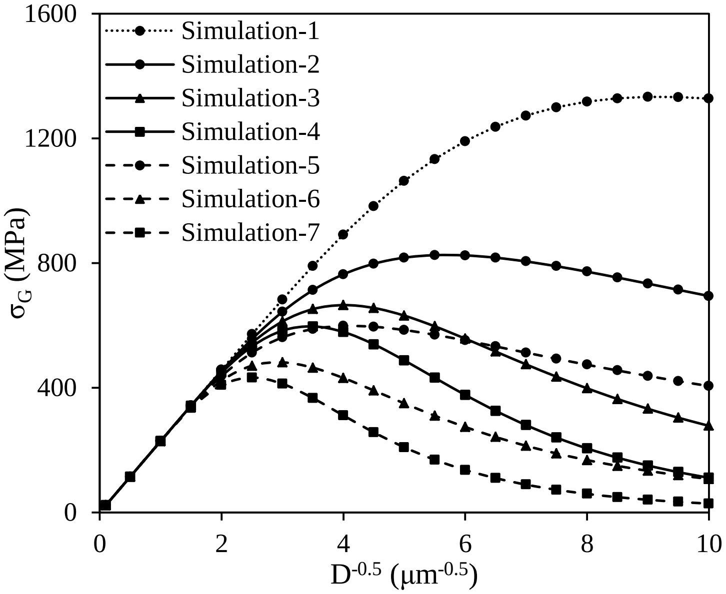

Figure 5.8: Grain boundary components of flow stress, σ_G, depicting the effects of parameters k_d and k_v at 600K.

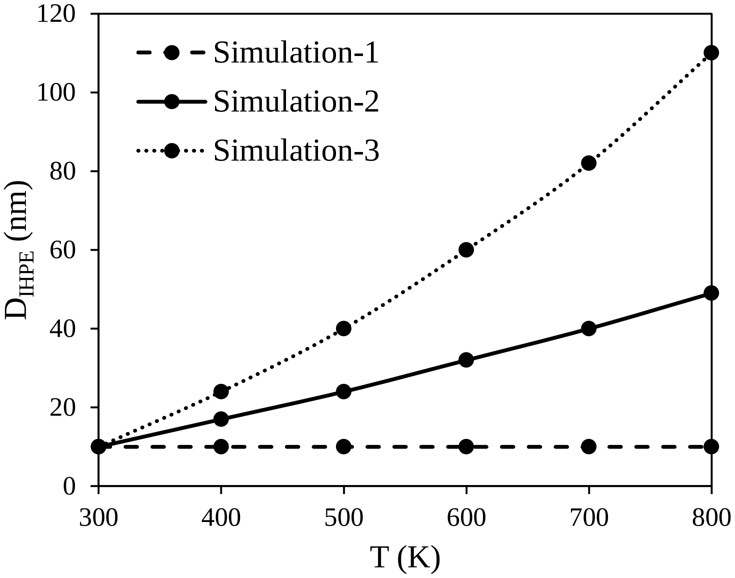

Figure 5.9: Critical grain size for initiation of IHPE, D_{IHPE}, at different temperatures for Simulations-1, 2, 3.

5.6.1.1 Cutting and thrust forces

The cutting and thrust forces are the principal measurements used to evaluate the quality of the simulation results for the different combinations of k_d and k_v. A sample temporal history of the simulated cutting and thrust forces with their variations due to chip segmentation is shown in Figure 5.10. A comparison of the simulated and experimental results for the selected cutting condition (cutting speed = 100 m/min; feed = 0.2 mm) is shown in Figure 5.11. The variations in the simulated F_c and F_t are very significant due to chip segmentation. By varying k_d from 0 to 0.0004 (Simulations-1, 2, 5), the corresponding critical grain sizes for the IHPE at elevated temperatures cause a decreasing trend in the simulated force magnitudes and an increasing trend in the force variation. The parameter k_d, varied from 0 to 0.01 (Simulations-2, 3, 4), also produces a similar influence on the force magnitudes and their variation by changing the flow stress softening rate due to the IHPE. From Figure 5.11, it can be seen that Simulations-2 and 3 give the best predictions for the cutting and thrust forces.

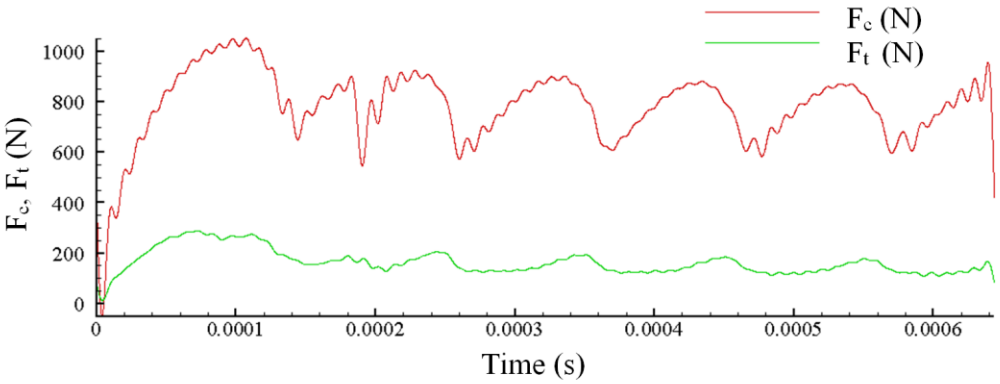

Figure 5.10: Sample temporal history of the simulated cutting and thrust forces at a cutting speed of 180 m/min and a feed of 0.3 mm.

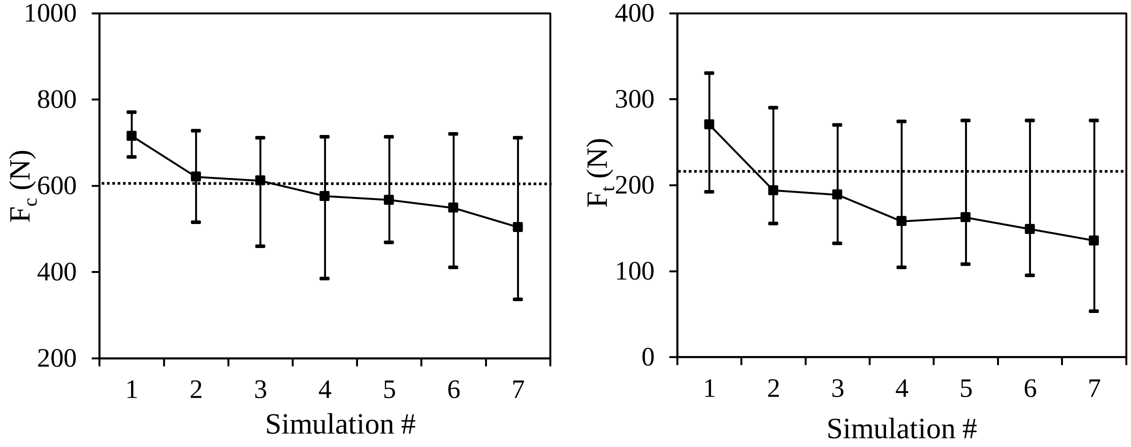

Figure 5.11: Experimental (dotted line) and simulated (symbols) cutting forces (F_c) and thrust forces (F_t) at a cutting speed of 100 m/min and a feed of 0.2 mm.

5.6.1.2 Chip geometry

As the one of most significant characteristics in machining of CP-Ti, chip segmentation and associated shear localization are successfully predicted by the developed unified model as shown in Figure 5.12 (b). In order to compare the simulation results with the measured chip geometry, the segmented chip morphology is characterized by its geometrical characteristics including the peak thickness (S_1), the valley thickness (S_2) and the banding distance (S_3) as shown in Figure 5.12 (a). Because the chip does not retain the same curvature during the dimensional measurements as during machining, the parameter S_3, which is influenced by the curvature of the machined chip, is replaced by the shear band frequency (f), which is defined as the number of shear bands produced per second.

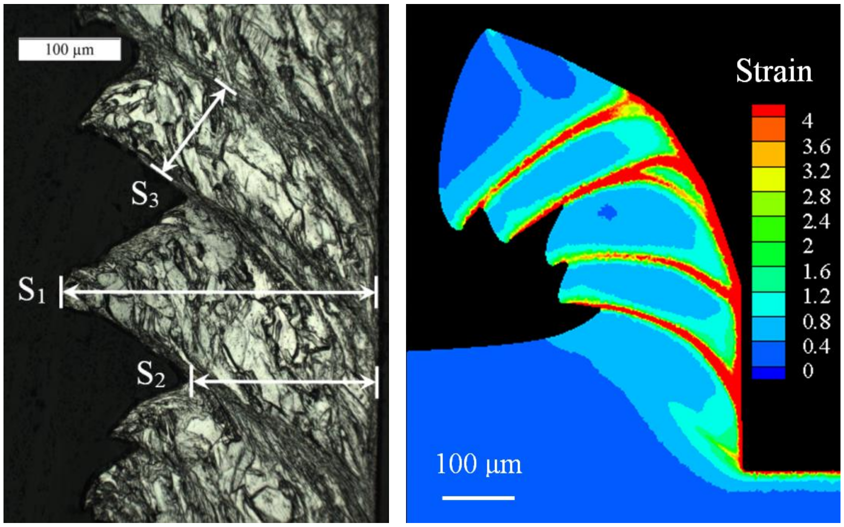

Figure 5.12: Experimental (left) and simulated (right) chip at a cutting speed of 100 m/min and a feed of 0.2 mm.

In addition to the cutting and thrust forces, the simulation results 1-7 are also evaluated by comparing with the measured chip geometry parameters S_1, S_2 and f, as shown in Figures 5.13 and 5.15. It is seen that the simulated values for S_1 and S_2 decrease with decreasing flow stress due to the IHPE. It can be seen that simulations 2 to 7 give reasonably good values for S_1. Except for simulations 6 and 7, most of the simulations overestimate the valley thickness S_2. One reason for the overestimation of S_2 is that the damage (e.g. cracks) on the free machined surface, shown in Figure 5.14, is not taken into consideration in this study. Calamaz et al. [96] have pointed out that implementing a fracture criterion into the simulation can improve the prediction of S_2 in machining of titanium alloys.

Chip segmentation becomes more evident as the thickness difference between the peaks and valleys increases in going from simulation 1 to 7.

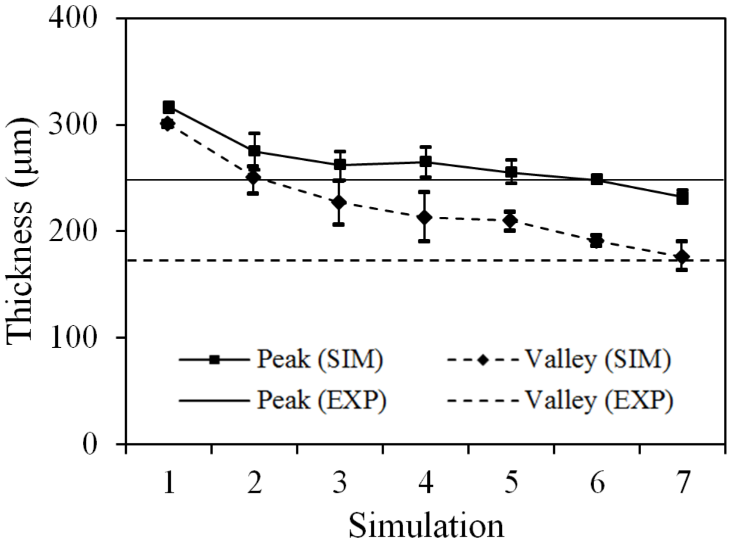

Figure 5.13: Experimental and simulated chip geometry (Peak: S_1; Valley: S_2) at a cutting speed of 100 m/min and a feed of 0.2 mm.

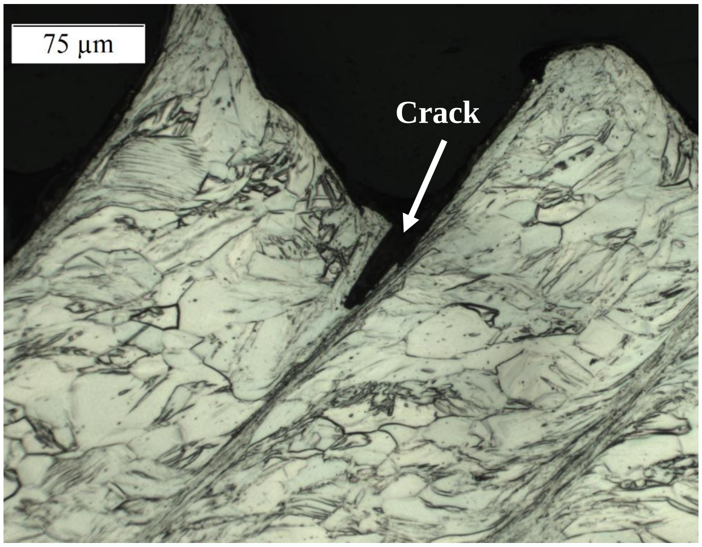

Figure 5.14: Cracks on the free surface of the machined chip at a cutting speed of 140 m/min and a feed of 0.3 mm.

5.6.1.3 Shear band frequency

A comparison of the experimental and simulated shear band frequencies for the different combinations of k_d and k_v at the specific cutting condition chosen for calibrating k_d and k_v is shown in Figure 5.15. For simulations 1 to 5, the shear band frequency is correctly captured with an error less than 15% while it is largely underestimated by simulations 6 and 7.

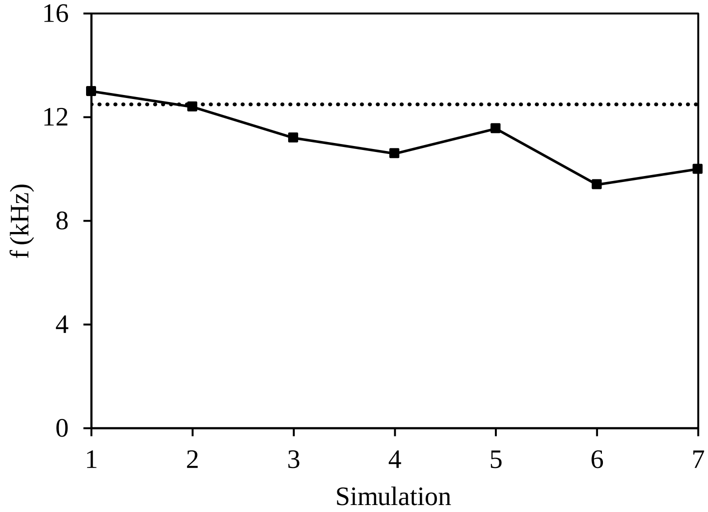

Figure 5.15: Experimental (dotted line) and simulated (solid line) chip segmentation frequency (*f*) at a cutting speed of 100 m/min and a feed of 0.2 mm.

5.6.2 Model validation

After systematically considering the performance of the IHPE model parameters k_d and k_v, the parameter combination used in simulation 3 ($k_d = 0.0002$; $k_v = 0.005$) is chosen as the most suitable for the specific cutting condition ($v_c = 100$ m/min; $t_u = 0.2$ mm). Note that greater emphasis is placed on the force prediction accuracy of the model in machining, this selection for k_d and k_v in conjunction with the rest of the parameters fitted in Section 5.3, the unified model is considered fully-calibrated. The calibrated model is then implemented in AdvantEdge^{TM} to validate it against experimental data for other cutting conditions (v_c = 20, 60, 100, 140, 180 m/min; t_u = 0.1, 0.2, 0.3 mm) and to assess the ability of the model to predict the cutting and thrust forces, machined chip geometry parameters and the shear band frequency. Additionally, the unified model is used to investigate the effects of strain, strain rate, and temperature on the machining simulations. The average grain size and dislocation density evolutions are also simulated and discussed.

5.6.2.1 Cutting and thrust forces

The simulated cutting (F_c) and (F_t) thrust forces are compared with the experimental results as shown in Figure 5.16. The experimental cutting and thrust forces decrease with increasing cutting speed and decreasing feed. The simulated results show a similar trend with less than 5% prediction error for the cutting force and 10-20% prediction error for the thrust force. The higher discrepancy in the thrust force predictions is attributed to the simple Coulomb friction model used and the absence of the effects of cutting tool wear, which is not included in this study.

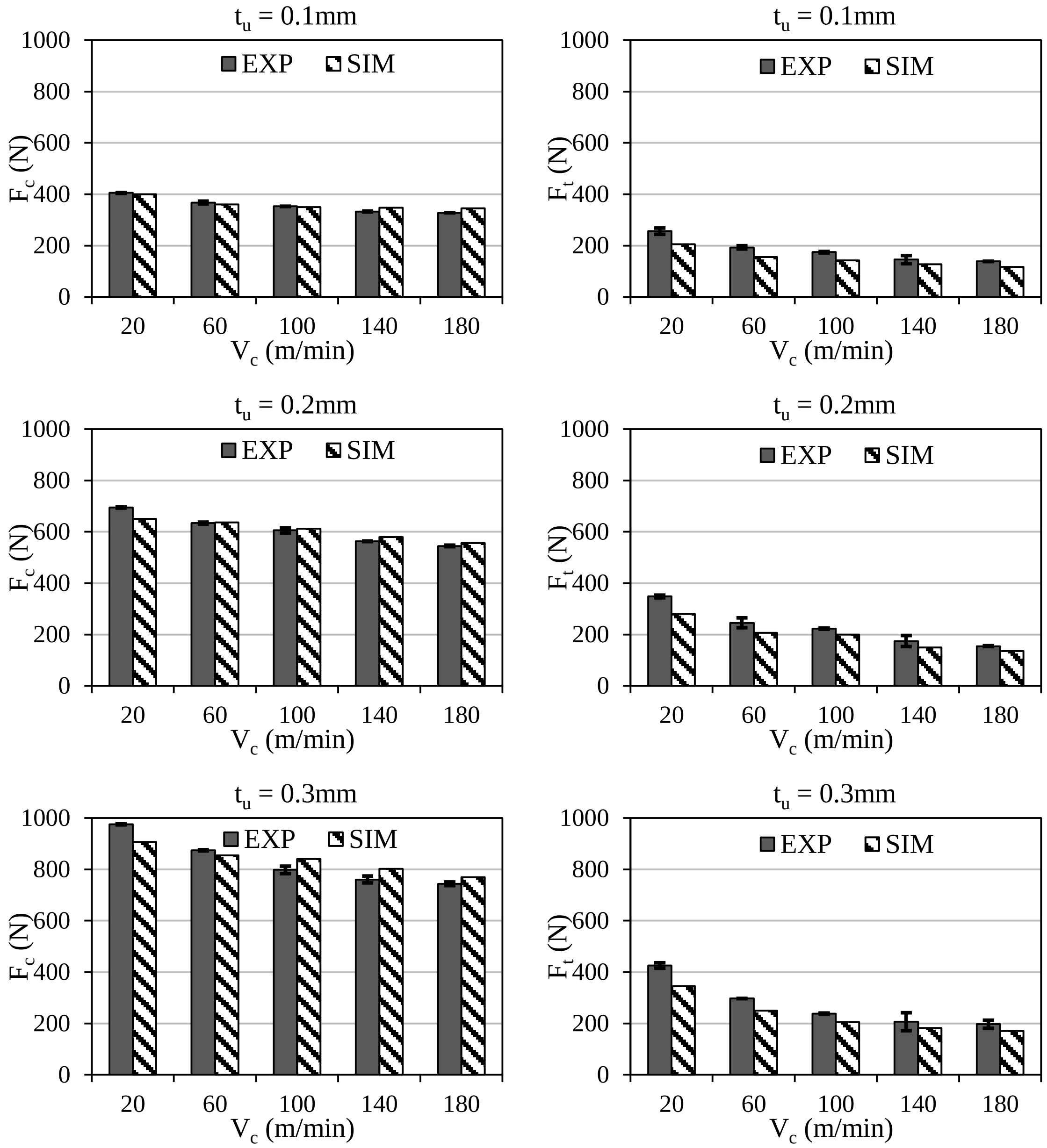

Figure 5.16: Experimental (EXP) and simulated (SIM) cutting (F_c) and thrust (F_t) forces at different cutting conditions.

5.6.2.2 Chip geometry and shear band frequency

The simulated peak (S_1) and valley (S_2) thicknesses of the segmented chips are compared with experimental measurements as shown in Figure 5.17. Generally, the measured chip thickness decreases with increasing cutting speed and decreasing feed. In addition, the difference between S_1 and S_2 also increases with increasing cutting speed. A possible reason for this phenomenon is that the higher cutting speed leads to greater softening due to the increased microstructure-related softening at elevated temperatures (due to DRV, DRX and IHPE), which is much greater than the effect of strain rate hardening. The simulated thicknesses (S_1 and S_2) show a similar trend as the experimental measurements, but overestimate the thicknesses, especially S_2, for most of the cutting conditions. As noted earlier, a possible reason for the overestimation of S_2 is the lack of inclusion of damage (cracks) on the free surface of the machined chip. Additionally, detailed comparisons of the chip morphology are shown in Figure 5.18. It can be seen that the major features of the segmented chip are mostly correctly predicted by the simulations. It is also noted that the machined chip serration and evidence of shear banding becomes more obvious as the cutting speed increases, which is also captured by the simulation results.

Figure 5.19 shows a comparison of the experimental (EXP) and simulated (SIM) frequencies of chip segmentation under different cutting conditions. The simulation results capture the experimental trend, which shows that the segmentation frequency increases almost linearly with cutting speed and decreases with increasing feed.

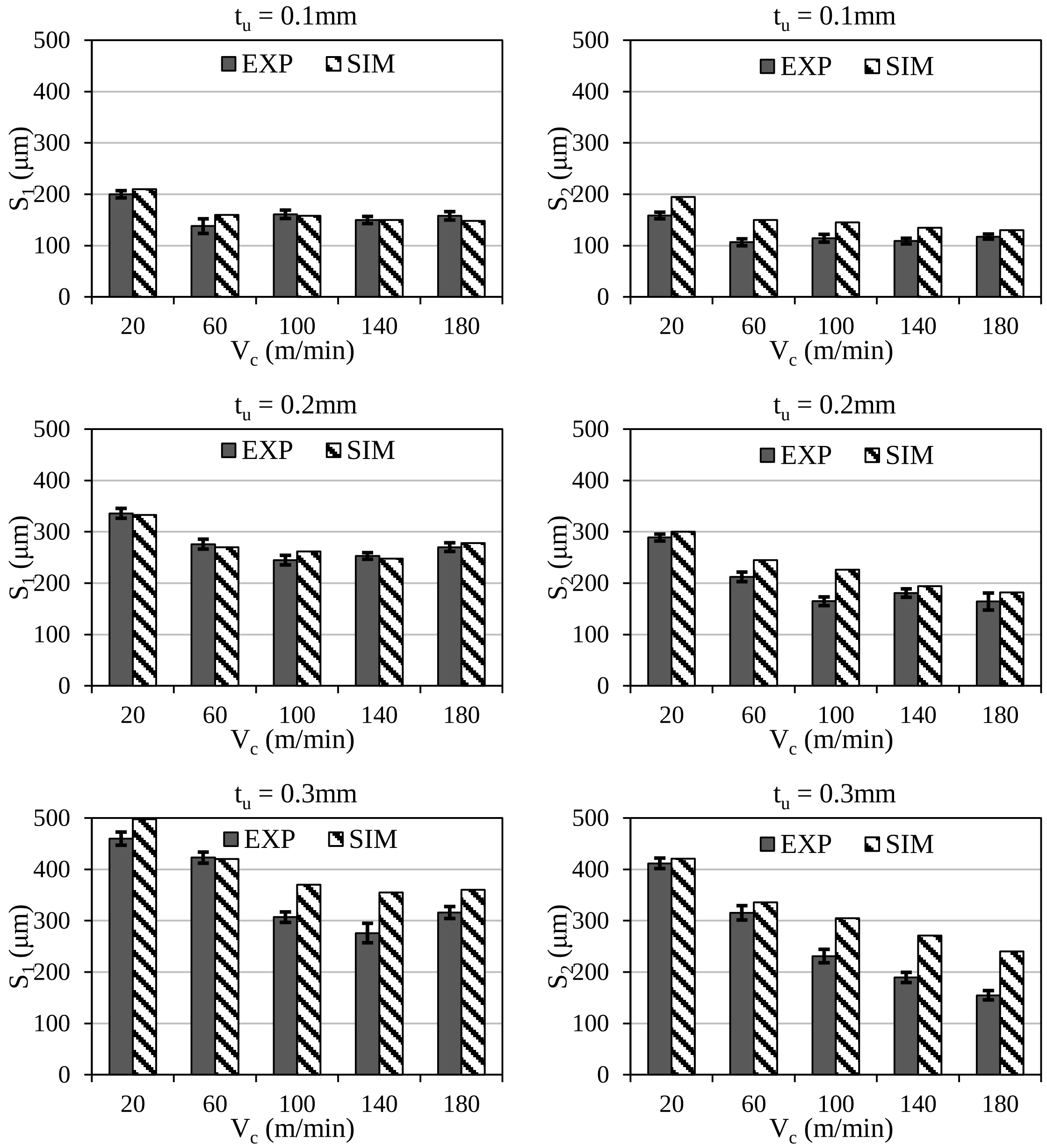

Figure 5.17: Experimental and simulated peak (S_1) and valley (S_2) thicknesses of machined chip at different cutting conditions.

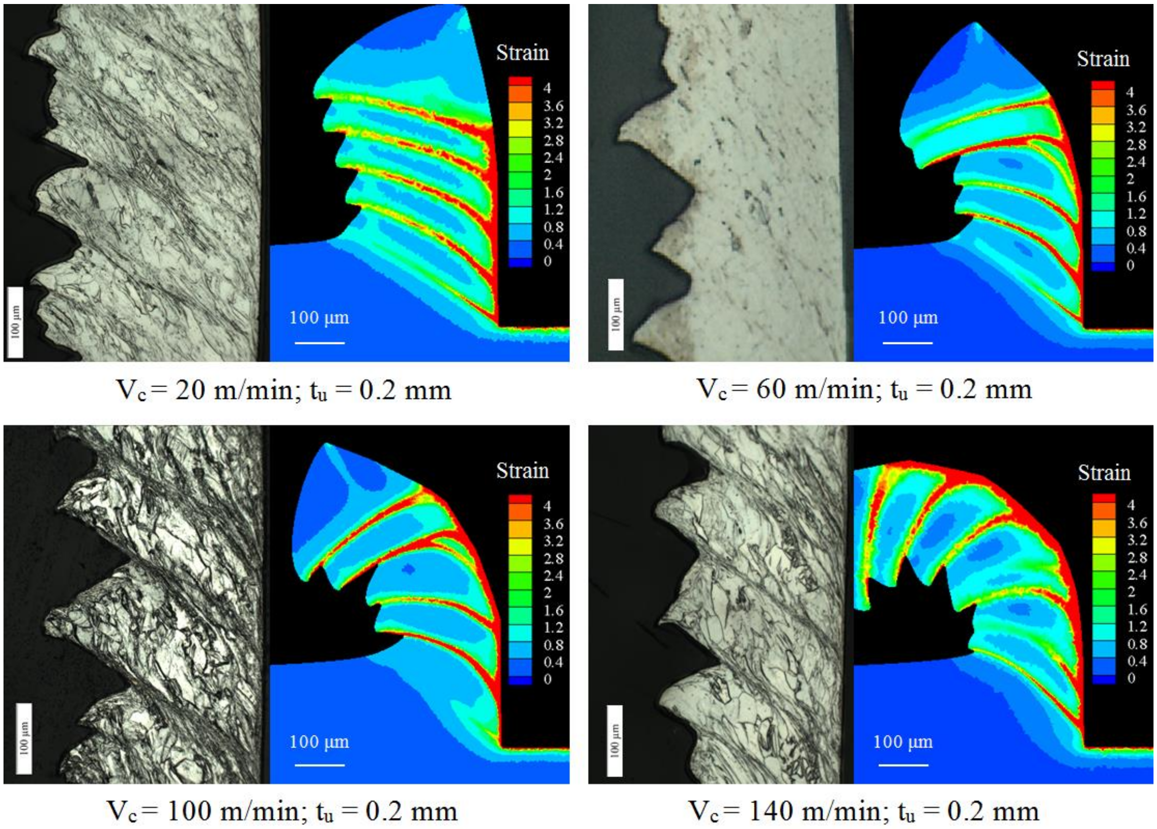

$V_c = 20$ m/min; $t_u = 0.2$ mm

$V_c = 60$ m/min; $t_u = 0.2$ mm

$V_c = 100$ m/min; $t_u = 0.2$ mm

$V_c = 140$ m/min; $t_u = 0.2$ mm

Figure 5.18: Comparison of measured chip images and simulated chip shapes.

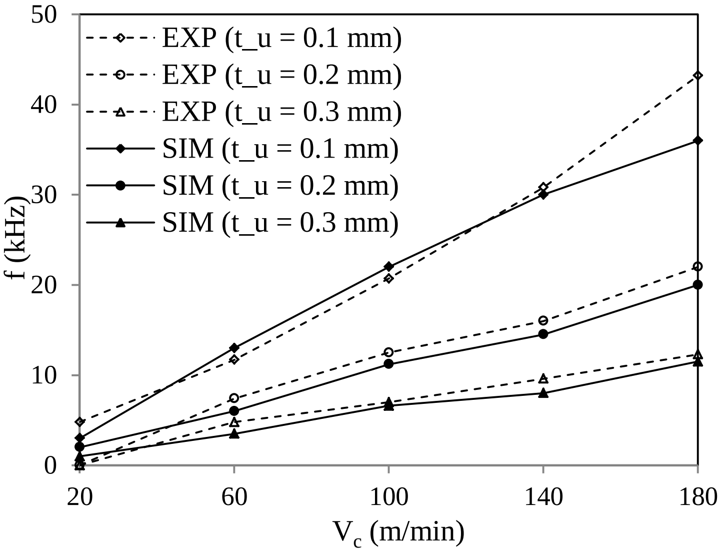

Figure 5.19: Comparison of experimental and simulated frequencies (*f*) of chip segmentation.

5.6.2.3 Temperature and strain distributions

Within the segmented chip, strain localization is observed inside the shear band and at the tool-chip interface as shown in Figure 5.20 (a). This observation is successfully predicted by the unified model as shown in Figure 5.20 (b). For chosen cutting condition (V_c = 100 m/min, t_u = 0.2 mm), the equivalent plastic strain inside the shear band is estimated to be ~ 7.3 using the calculation method (Equation 5.10) proposed by Turley and Doyle [164] as shown in Figure 5.21 and the width of the shear band, which is approximately 10 μm in this case. In comparison, the simulated equivalent plastic strain inside the shear band is around 6.0, which is smaller than the calculated value due to the overestimation of the valley chip thickness (S_2).

$$\varepsilon = \frac{\gamma}{\sqrt{3}} = \frac{1}{\sqrt{3}}\left(\frac{ae}{ad} + \frac{cb}{t}\right) \tag{5.10}$$

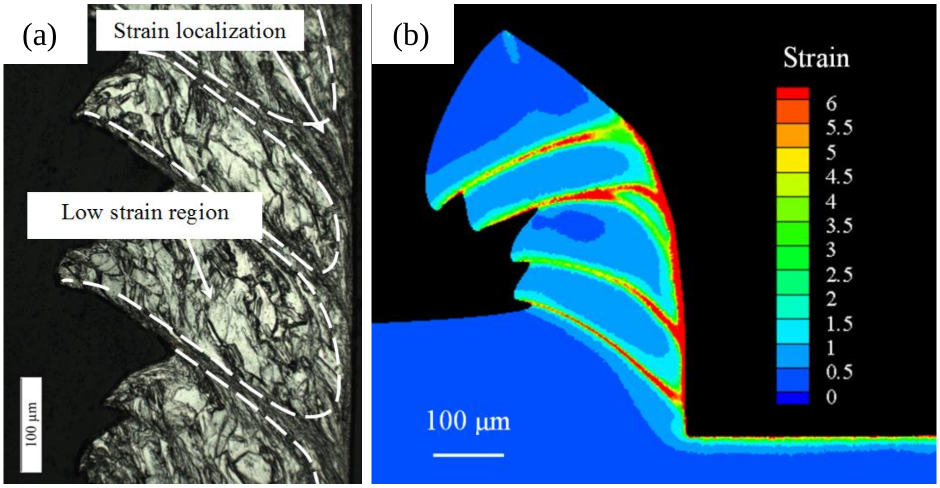

Figure 5.20: Strain field in: (a) experimental and (b) simulated chips at a cutting speed of 100 m/min and a feed of 0.2 mm.

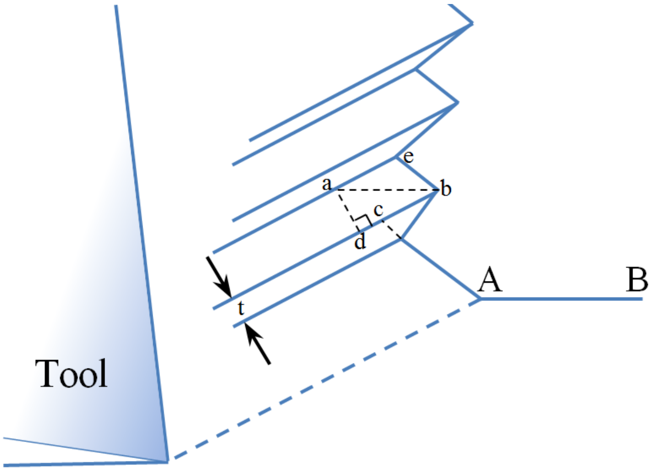

Figure 5.21: Illustration showing how to calculate the shear strain in the shear band [164].

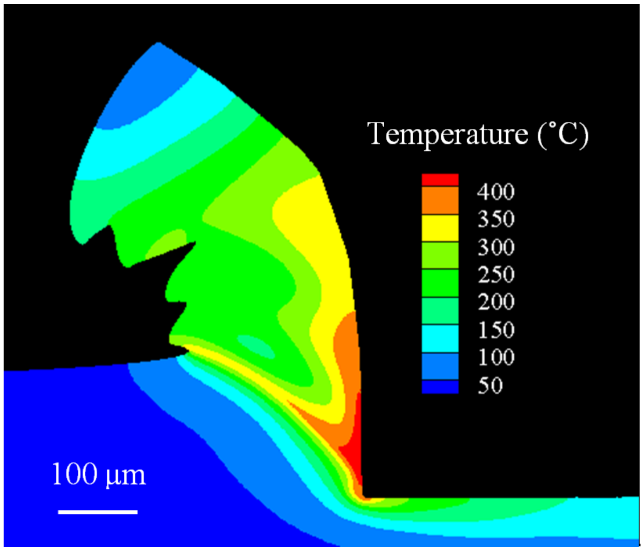

Figure 5.22: Temperature distribution in the simulated chip at a cutting speed of 100 m/min and a feed of 0.2 mm.

Figure 5.22 shows the simulated temperature distribution in the machined chip. It is noted that relatively high temperatures (~ 350˚C) are predicted in the primary shear zone due to severe plastic deformation in this region. The low thermal conductivity of the workpiece leads to high temperature concentration in the narrow band and consequent thermal softening, which is responsible for shear localization. High temperature is also predicted at the tool-chip interface and is mainly due to friction. The highly concentrated temperature in this region can cause rapid tool wear.

5.6.2.4 Microstructure in the shear band region

In order to evaluate the ability of the model to predict the microstructure characteristics of the machined chip, four special locations in the chip, marked *A* to *D* in Figure 5.23, are selected to investigate the model behavior. Position *A* is away from the shear band, *B* is on the boundary, *C* is inside the shear band, and *D* is at the tip of the shear band. The corresponding distribution of the microstructure parameters, namely grain size and dislocation density, in the four locations are shown in Figure 5.23.

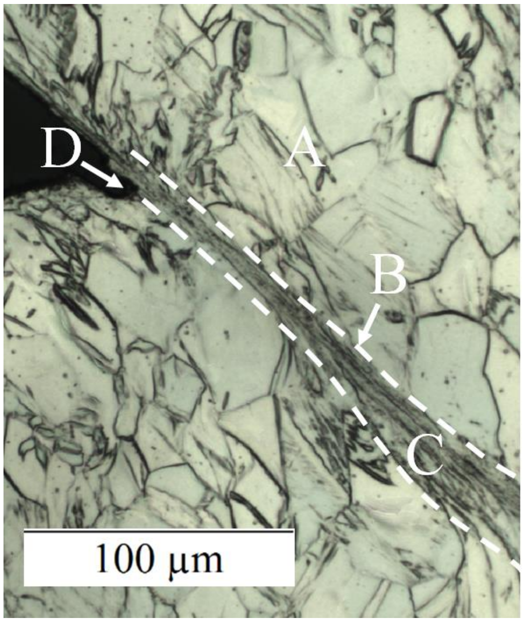

Figure 5.23: Optical micrograph showing the region along the shear band at four locations marked *A* to *D* (V_c = 100 m/min, t_u = 0.2 mm).

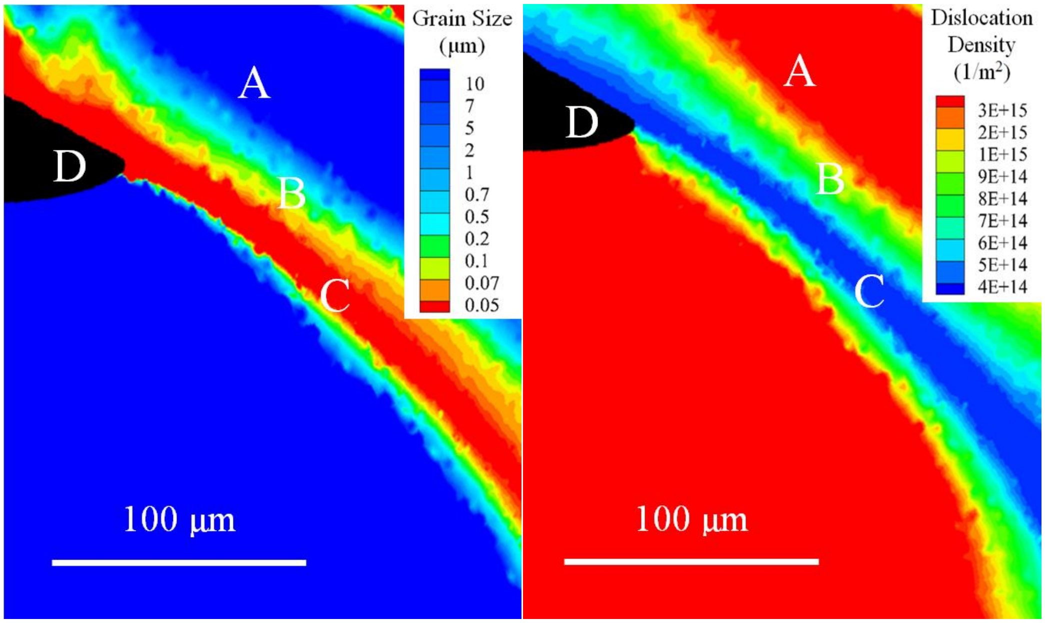

(a) (b)

Figure 5.24: Simulated (a) grain size and (b) dislocation density distributions with four locations marked *A* to *D* (V_c = 100 m/min, t_u = 0.2 mm).

In location *A*, which is away from the shear band in Figure 5.23, the grains are nearly of the same size as in the as-received microstructure, ~ 40 μm (shown in Figure 5.7). In addition, the presence of the twin structures observed in location *A* in the actual chip is indicative of the small plastic deformation in this area. The simulation result in Figure 5.24 (a) predicts a similar microstructure with large grain sizes at the same location due to the relatively lower plastic strains seen earlier in Figure 5.20 (b). The small plastic strain (less than 1) in this region still produces higher dislocation density, compared to the undeformed material with the initial dislocation density, as shown in Figure 5.24 (b).

Location *B* is on the boundary of the shear band. The observed elongated grain structure (Figure 5.23) indicates that sufficiently large plastic deformation occurred in this region as can be seen in Figure 5.20 (b). The severe plastic deformation causes grain refinement (due to DRX), which is captured by the model as seen in Figure 5.24 (a).

Inside the shear band (location *C*), the simulation result yields an ultrafine grain size as shown in Figure 5.24 (a), which indicates the highly refined grain structure caused by DRX. The predicted grain size (50 ~ 70 nm) within the shear band was found to be in reasonable agreement with the measured grain sizes (50 ~ 150 nm) reported by Chichili et al. [111], who analyzed shear banding in a compression-torsion Kolsky bar test conducted on CP-Ti material. At elevated temperatures (> 300 ˚C) within the primary shear zone (see Figure 5.22), the ultrafine grains can give rise to the IHPE, which causes softening of the material. Additionally, low dislocation density is predicted inside the shear band as shown in Figure 5.24 (b), which is consistent with the ultrafine grain structure seen in Figure 5.24 (a). These trends agree with the experimental observations of DRX by Meyers et al. [165]. In this study, the low dislocation density within the shear band can be explained by dislocation annihilation during DRX leading to grain refinement, which is consistent with the underlying physics of DRX [121]. During severe plastic deformation and as DRX occurs, low angle grain boundaries (LABs) nucleate and their misorientation angles grow due to dislocation production and accumulation mechanisms until those LABs transition into high angle grain boundaries (HABs) and form new grains.

Position *D* is at the end of the shear band on the free surface of the machined chip. It is noted that some cracks are often observed at this location at high cutting speeds, as shown in Figure 5.23. As discussed before, the fracture mechanism is not considered in this study and therefore the simulation is unable to reproduce this observation.

5.7 Conclusions

In this section, the performance of the unified material model explicitly integrating microstructure evolution (particularly due to DRX) into the constitutive law in order to describe the macro-scale material behavior during severe plastic deformation is evaluated in predicting chip segmentation in orthogonal machining of commercially pure titanium. The model incorporates the Inverse Hall-Petch Effect (IHPE) to describe the effect of ultrafine grain structure inside the shear band on the flow strength of the material. In order to validate the simulation results, orthogonal cutting experiments were performed using uncoated carbide cutting tools over a wide range of feeds and cutting speeds. Cutting and thrust forces and chip morphology parameters were measured. When compared with experimental results, the model simulations show good prediction capability in terms of the cutting force (less than 10% error), thrust force (less than 20% error), segmentation frequency, and chip morphology parameters. Additionally, the plastic strain predicted by the model is found to agree (on an order of magnitude basis) with the strain calculated from the measured chip geometry. Moreover, the simulations also enable the prediction of the distribution of microstructure parameters, namely the grain size and dislocation density, which are shown to in reasonable agreement with the measured microstructure and the underlying deformation physics.

CHAPTER 6

SUMMARY, CONCLUSIONS AND RECOMMENDATIONS

This chapter includes the summary and major conclusions of this thesis and suggests related research areas for further studies.

6.1 Summary

The main aspects of this thesis are summarized as follows:

6.1.1 Development of a unified constitutive model

- A unified model explicitly integrating grain size and dislocation density evolution in the constitutive description was developed using basic understanding of the underlying mechanics of dislocation interaction with short range and long range obstacles during inelastic deformation in conjunction with thermal activation theory.
- A phenomenological model was introduced in this study to capture the grain size evolution during severe plastic deformation accompanying metal machining.
- The effects of hardening, dynamic recovery and dynamic recrystallization were collectively captured in the evolution laws for dislocation density and grain size.
- A new model calibration procedure was developed to calibrate the different components of the model using different parts of the stress-strain curves of the material undergoing deformation.

- The model was calibrated and validated against experimental flow stress-strain curves for SS304 over a range of strain rates and temperatures.
- The model was used to analyze the individual contributions of the long and short range barriers on the overall flow stress and the variation of the corresponding stress components with strain, strain rate, and temperature.

6.1.2 Simulation of continuous chip formation in machining of OFHC copper

- In order to make the unified model applicable in the extremely high strain rate ($10^4 - 10^6$ /s) deformation regime commonly encountered in machining, a dislocation drag component was added to the flow stress formulation derived from thermal activation theory.
- The model was calibrated and validated against experimental flow stress-strain curves for OFHC copper over a range of strain rates and temperatures.
- The model predictions were experimentally validated in orthogonal cutting of OFHC copper over a wide range of cutting speeds in terms of cutting and thrust forces.
- The model predictions were used to investigate the evolution of deformation parameters and microstructure parameters during machining process.

6.1.3 Simulation of segmented chip formation in machining of commercially pure titanium

- In order to describe the behavior of nano-scale grains within the shear bands, the inverse Hall-Petch effect was incorporated into the unified constitutive model.

- The model was calibrated and validated against experimental flow stress-strain curves for CP-Ti over a range of strain rates and temperatures.
- The model predictions were experimentally validated in orthogonal cutting of CP-Ti over a wide range of cutting speeds and feeds in terms of the cutting and thrust forces, chip segmentation frequency, and chip geometry parameters.
- The model simulations predicted the distribution of microstructure parameters, namely grain size and dislocation density, during chip segmentation.

6.2 Major Conclusions

The major conclusions of this thesis can be summarized as follows:

- The model predictions were found to be in reasonable agreement with the experimental flow stress-strain curves for SS304, OFHC copper, and CP-Ti over a range of strain rates and temperatures.
- The unified model can be used to analyze the individual contributions of the long and short range barriers on the overall flow stress and the variation of the corresponding stress components with strain, strain rate, and temperature.
- The prediction capability of the model at high strain rates can be improved by incorporating the dislocation drag effect.
- The continuous chip formation in orthogonal cutting of OFHC copper was successfully predicted by the finite element simulations obtained using the developed unified constitutive model.

- The model was found to yield good predictions of the cutting and thrust forces with errors less than 10% in orthogonal cutting of OFHC copper.
- The model successfully predicted the commonly observed trend of severe grain refinement due to DRX in orthogonal cutting of OFHC copper.
- The segmented chip formation in orthogonal cutting of CP-Ti was shown to be successfully predicted by the finite element simulations obtained using the developed unified model incorporating the inverse Hall-Petch effect.
- The model simulations showed good prediction accuracy for the cutting force (< 10% error) and thrust force (< 20% error), segmentation frequency, and chip geometry parameters in orthogonal cutting of CP-Ti.
- The model simulations enabled the prediction of the distribution of microstructure parameters, namely grain size and dislocation density, during chip segmentation in orthogonal cutting of CP-Ti, which agreed (on an order of magnitude basis) with the reported microstructure observations and the underlying physics.

6.3 Recommendations and Future Work

This study investigated the fundamental material behavior and microstructure evolution during the metal machining process. The developed unified material model can be optimized or generalized in following directions:

6.3.1 Constitutive material model

- In this study, the plastic deformation of the workpiece in machining has been explained by several underlying physical mechanisms. However, some important mechanisms, such as deformation twining and grain size elongation, have not been considered. Under specific cutting conditions, these mechanisms can have a strong influence on the material behavior of the workpiece in machining.

- In this thesis, the developed unified model is only applied to investigate the machining response of pure metals (OFHC copper, CP-Ti). In order to extend the applicability of the model to machining of alloys, the associated physical mechanisms, such as precipitation hardening, solution strengthening, and phase transformation need to be further investigated.
- Although a new model calibration procedure has been established to calibrate the unified model, a more systematic and simplified calibration method using statistical data guided approaches (see [166]) are desirable.

6.3.2 Finite element modeling

- Frictional interaction at the chip-tool interface is modeled using a simple Coulomb friction law with constant friction coefficient, which influences the accuracy of the machining simulation, especially the thrust force prediction. The error caused by the simplified friction model can be further reduced by defining variable friction regions at the tool-chip interface (e.g. stick, slip).
- Thermal properties, such as the thermal conductivity of the workpiece material, are very critical for estimating the temperature rise in the deformation zone. In this study, the thermal properties are considered to be a function of temperature only. Further investigation of the influence of microstructure evolution on these

parameters is lacking. For example, grain boundaries, which act as thermal resistors, can influence the thermal conductivity [167].

6.3.3 Machining experiments

- Due to limited availability of experimental data for the microstructure of machined chips, the validation of the unified model is insufficient. Further experimental investigation of the deformed microstructure in the chip (especially for segmented/shear localized chips) is needed.
- In order to investigate the material behavior in the primary shear zone, a quick stop device used to freeze the cutting action is needed and can yield useful physical insight and data for model development and validation.
- In machining experiments, severe side flow of the machined chip is often observed, especially in machining of ductile metals such as OFHC copper. Side flow can influence the chip geometry and cutting force measurements. The error caused by material side flow can be reduced by considering side flow in the machining simulation or by optimizing the experimental setup to eliminate this effect.

APPENDIX A

EXPERIMENTAL DATA FOR MACHINING OF CP-TI

A.1 Cutting Force

t_u (mm)	v_c (m/min)	F_c (N)			
		Run-1	Run-2	Mean	Range
0.1	20	406.57	404.66	405.62	1.91
0.1	60	370.33	365.29	367.81	5.04
0.1	100	352.83	352.91	352.87	0.09
0.1	140	331.82	334.09	332.96	2.26
0.1	180	327.75	327.52	327.63	0.24
0.2	20	695.68	693.22	694.45	2.47
0.2	60	631.91	635.79	633.85	3.88
0.2	100	611.09	601.13	606.11	9.96
0.2	140	563.55	562.43	562.99	1.11
0.2	180	543.65	546.27	544.96	2.63
0.3	20	977.35	974.96	976.15	2.39
0.3	60	875.20	872.81	874.01	2.40
0.3	100	805.29	790.92	798.10	14.37
0.3	140	767.36	753.71	760.53	13.66
0.3	180	747.16	740.39	743.78	6.76

A.2 Thrust Force

t_u (mm)	v_c (m/min)	F_c (N)			
		Run-1	Run-2	Mean	Range
0.1	20	262.10	250.31	256.21	11.80
0.1	60	196.32	189.97	193.15	6.35
0.1	100	175.95	173.32	174.64	2.63
0.1	140	137.53	153.61	145.57	16.08
0.1	180	138.63	138.24	138.44	0.39
0.2	20	345.50	350.95	348.23	5.45
0.2	60	235.59	254.94	245.27	19.35
0.2	100	223.79	221.52	222.65	2.27
0.2	140	184.89	163.64	174.27	21.25
0.2	180	155.54	153.70	154.62	1.84
0.3	20	431.09	420.71	425.90	10.38
0.3	60	297.11	297.61	297.36	0.49
0.3	100	237.28	238.98	238.13	1.69
0.3	140	224.40	189.48	206.94	34.92
0.3	180	204.46	188.87	196.66	15.59

A.3 Chip Geometry

t_u (mm)	v_c (m/min)	S1 (μm)		S2 (μm)		*f* (kHz)
		Mean	SD*	Mean	SD*	
0.1	20	200	6.99	158.55	6.6	4.8
0.1	60	138	14.11	106.69	6.63	11.7
0.1	100	161	7.92	114.32	7.57	20.7
0.1	140	150	6.87	108.83	5.52	30.8
0.1	180	158	8.2	117.49	4.76	43.2
0.2	20	336	9.67	288.93	6.65	**
0.2	60	276	9.39	212.1	9.21	7.4
0.2	100	245	9.4	164.78	8.19	12.5
0.2	140	253	6.56	180.83	8.06	16
0.2	180	270	8.46	164.24	16.72	22
0.3	20	460	12.73	411.72	10.32	**
0.3	60	423	10.69	315.27	13.93	4.8
0.3	100	307	10	231.1	13.28	7
0.3	140	276	18.84	189.53	9.65	9.6
0.3	180	316	11.46	154.83	8.8	12.3

* Standard deviation of 10~15 measurements

** Almost indistinguishable

APPENDIX B

SIMULATION RESULTS FOR MACHINING OF CP-TI

B.1 Cutting and Thrust Forces

t_u (mm)	v_c (m/min)	F_c (N)		F_t (N)	
		Mean	Error* (%)	Mean	Error* (%)
0.1	20	400	-1.39	205	-19.99
0.1	60	360	-2.12	155	-19.75
0.1	100	350	-0.81	142	-18.69
0.1	140	348	4.52	127	-12.76
0.1	180	345	5.30	117	-15.49
0.2	20	650	-6.40	280	-19.59
0.2	60	636	0.34	207	-15.60
0.2	100	612	0.97	199	-10.62
0.2	140	579	2.84	150	-13.93
0.2	180	556	2.03	135	-12.69
0.3	20	907	-7.08	345	-19.00
0.3	60	855	-2.17	250	-15.93
0.3	100	840	5.25	205	-13.91
0.3	140	802	5.45	182	-12.05
0.3	180	769	3.39	170	-13.56

* w. r. t. the mean value of experimental data

B.2 Chip Geometry

t_u (mm)	v_c (m/min)	S1 (µm)	S2 (µm)	f (kHz)
0.1	20	210	195	3
0.1	60	160	150	13
0.1	100	158	145	22
0.1	140	150	135	30
0.1	180	148	130	36
0.2	20	333	300	2
0.2	60	270	245	6
0.2	100	262	226	11.2
0.2	140	248	194	14.5
0.2	180	278	182	20
0.3	20	498	421	1
0.3	60	420	336	3.5
0.3	100	370	305	6.6
0.3	140	355	271	8
0.3	180	360	240	11.5

REFERENCES

1. Johnson, G.R. and W.H. Cook, *A constitutive model and data for metals subjected to large strains, high strain rates and high temperatures.* Proceedings of the 7th International Symposium on Ballistics, 1983. **54**: p. 1-7.

2. Zerilli, F.J. and R.W. Armstrong, *Dislocation-mechanics-based constitutive relations for material dynamics calculations.* J. Appl. Phys., 1987. **61**(5): p. 1816-1825.

3. Nemat-Nasser, S. and Y. Li, *Flow stress of f.c.c. polycrystals with application to OFHC Cu.* Acta Mater., 1998. **46**: p. 565-577.

4. Strenkowski, J.S. and J.T. Carroll, *A finite element model of orthogonal metal cutting.* J. Manuf. Sci. Eng., 1985. **107**(4): p. 349-354.

5. Guo, Y.B., *An integral method to determine the mechanical behavior of materials in metal cutting.* J. Mater. Process. Tech., 2003. **142**(1): p. 72-81.

6. Mecking, H. and U.F. Kocks, *Kinetics of flow and strain-hardening.* Acta Metall., 1981. **29**: p. 1865-1875.

7. Stout, M.G. and P.S. Follansbee, *Strain rate sensitivity, strain hardening, and yield behavior of 304L stainless steel.* J. Eng. Mater. Technol., 1986. **108**(4): p. 344-353.

8. Voce, E., *The relationship between stress and strain for homogeneous deformation.* J. Inst. Met., 1948. **74**: p. 537-562.

9. Swift, H.W., *Plastic instability under plane stress.* J. Mech. Phys. Solids, 1952. **1**(1): p. 1-18.

10. Ludwik, P., *Elemente der technologischen Mechanik.* J. Springer, 1909.

11. Hollomon, J.H., *Tensile deformation.* Trans. AIME, 1945. **162**: p. 268-290.

12. Kocks, U.F., *Laws for work-hardening and low-temperature creep.* J. Eng. Mater.Technol.-T. ASME, 1976. **98**: p. 76-85.

13. Johnston, W.G. and J.J. Gilman, *Dislocation velocities, dislocation densities, and plastic flow in Lithium Fluoride crystals.* J. Appl. Phys., 1959. **30**: p. 129-144.

14. Estrin, Y. and H. Mecking, *A unified phenomenological description of work hardening and creep based on one parameter models.* Acta Metall., 1984. **32**: p. 57-70.

15. Zerilli, F.J. and R.W. Armstrong, *Constitutive relations for titanium and Ti-6Al-4V.* AIP Conf. Proc., 1996. **370**: p. 315-318.

16. Zerilli, F.J. and R.W. Armstrong. *Dislocation mechanics based constitutive equation incorporating dynamic recovery and applied to thermomechanical shear instability*. in *AIP Conf. Proc.* . 1998.

17. Voyiadjis, G.Z. and F.H. Abed, *Microstructural based models for bcc and fcc metals with temperature and strain rate dependency.* Mech. Mater., 2005. **37**(2): p. 355-378.

18. Meyers, M.A., et al., *Constitutive description of dynamic deformation: physically-based mechanisms.* Mater. Sci. Eng. A, 2002. **322**(1): p. 194-216.

19. Follansbee, P.S. and U.F. Kocks, *A constitutive description of the deformation of copper based on the use of the mechanical threshold stress as an internal state variable.* Acta Metall., 1988. **36**(1): p. 81-93.

20. Follansbee, P.S. and G.T. Gray III, *An analysis of the low temperature, low and high strain-rate deformation of Ti-6Al-4V.* Metall. Trans. A, 1989. **20**(5): p. 863-874.

21. Follansbee, P.S., et al., *A lower-bound temperature and strain-rate dependent strength model for AISI 304 SS*, in *ASME 2011 pressure vessels and piping conference* 2011, American Society of Mechanical Engineers: Baltimore, Maryland, USA. p. 113-120.

22. Follansbee, P.S., *An internal state variable constitutive model for deformation of austenitic stainless steels.* J. Eng. Mater. Technol., 2012. **134**(4): p. 1-10.

23. Nemat-Nasser, S. and J.B. Isaacs, *Direct measurement of isothermal flow stress of metals at elevated temperatures and high strain rates with application to Ta and Ta-W alloys.* Acta Mater., 1997. **45**(3): p. 907-919.

24. Kocks, U.F., A.S. Argon, and M.F. Ashby, *Thermal Activation.* Prog. Mater. Sci., 1975. **19**: p. 139-143.

25. Luton, M.J. and C.M. Sellars, *Dynamic recrystallization in nickel and nickel-iron alloys during high temperature deformation.* Acta Metall., 1969. **17**(8): p. 1033-1043.

26. Sah, J.P., G.J. Richardson, and C.M. Sellars, *Grain-size effects during dynamic recrystallization of Nickel.* Metal Sci., 1974. **8**: p. 325-331.

27. Rollett, A.D., M.J. Luton, and D.J. Srolovitz, *Microstructural simulation of dynamic recrystallization.* acta Metall. Mater., 1992. **40**(1): p. 43-55.

28. Peczak, P. and M.J. Luton, *A Monte Carlo study of the influence of dynamic recovery on dynamic recrystallization.* Acta Metall. Mater., 1993. **41**(1): p. 59-71.

29. Ding, R. and Z.X. Guo, *Coupled quantitative simulation of microstructural evolution and plastic flow during dynamic recrystallization.* Acta Mater., 2001. **49**: p. 3163-3175.

30. Yazdipour, N., C.H.J. Davies, and P.D. Hodgson, *Microstructural modeling of dynamic recrystallization using irregular cellular automata.* Comput. Mater. Sci., 2008. **44**(2): p. 566-576.

31. Hallberg, H., M. Wallin, and M. Ristinmaa, *Modeling of continuous dynamic recrystallization in commercial-purity aluminum.* Mater. Sci. Eng. A, 2010. **527**(4): p. 1126-1134.

32. Taylor, G., *Mechanism of plastic deformation of crystals: Part i. Theoretical.* Proceedings of the Royal Society, 1934. **145**: p. 362-387.

33. Picu, R.C. and A. Majorell, *Mechanical behavior of Ti–6Al–4V at high and moderate temperatures—Part II: constitutive modeling.* Mater. Sci. Eng. A, 2002. **326**: p. 306-316.

34. Fan, X.G. and H. Yang, *Internal-state-variable based self-consistent constitutive modeling for hot working of two-phase titanium alloys coupling microstructure evolution.* Int. J. Plasticity, 2011. **27**(11): p. 1833-1852.

35. Tóth, L.S., A. Molinari, and Y. Estrin, *Strain hardening at large strains as predicted by dislocation based polycrystal plasticity model.* J. Eng. Mater.Technol.-T. ASME, 2002. **124**: p. 71-77.

36. Lemiale, V., et al., *Grain refinement under high strain rate impact: a numerical approach.* Comp. Mater. Sci., 2010. **48**: p. 124-132.

37. Estrin, Y. and H.S. Kim, *Modelling microstructure evolution toward ultrafine crystallinity produced by severe plastic deformation.* J. Mater. Sci., 2007. **42**: p. 1512-1516.

38. Shaw, M.C., *Metal Cutting Principles* 1984, Clarendon: Oxford University Press.

39. Zerilli, F.J. and R.W. Armstrong, *The effect of dislocation drag on the stress-strain behavior of f.c.c. metals.* Acta Metall. Mater., 1992. **40**: p. 1803-1808.

40. Follansbee, P.S. and U.F. Kocks, *A constitutive description of the deformation of copper based on the use of the mechanical threshold stress as an internal state variable.* Acta Metall., 1988. **36**: p. 81-93.

41. Follansbee, P.S. and J. Weertman, *On the question of flow stress at high strain rates controlled by dislocation viscous flow.* Mech. Mater., 1982. **1**: p. 345-350.

42. Regazzoni, G., U.F. Kocks, and P.S. Follansbee, *Dislocation kinetics at high strain rates.* Acta Metall., 1987. **35**: p. 2865-2875.

43. Nemat-Nasser, S. and W. Guo, *High strain-rate response of commercially pure vanadium.* Mech. Mater., 2000. **32**: p. 243-260.

44. Guo, W. and S. Nemat-Nasser, *Flow stress of nitronic-50 stainless steel over a wide range of strain rates and temperatures.* Mech. Mater., 2006. **38**: p. 1090-1103.

45. Wedberg, D., A. Svoboda, and L.E. Lindgren, *Modelling high strain rate phenomena in metal cutting simulation.* Model. Simul. Mater. Sci. Eng., 2012. **20**: p. 19.

46. Lindgren, L.E., K. Domkin, and S. Hanson, *Dislocations, vacancies and solute diffusion in a physically based plasticity model for AISI 316L.* Mech. Mater., 2008. **40**: p. 907-919.

47. Hall, E.O., *The deformation and ageing of mild steel: III discussion of results.* Proc. Phys. Soc. B, 1951. **64**(9): p. 747-753.

48. Petch, N.J., *The Cleavage Strength of Polycrystals.* J. Iron Steel Inst., 1953. **174**: p. 25-28.

49. Meyers, M.A., A. Mishra, and D.J. Benson, *Mechanical properties of nanocrystalline materials.* Prog. Mater. Sci., 2006. **51**(4): p. 427-556.

50. Chokshi, A.H., et al., *On the validity of the Hall-Petch relationship in nanocrystalline materials.* Scripta metall., 1989. **23**(10): p. 1679-1683.

51. Conrad, H. and J. Narayan, *On the grain size softening in nanocrystalline materials.* Scripta Mater., 2000. **42**(11): p. 1025-1030.

52. Li, J.C., *Petch relation and grain boundary sources.* TMS-AIME, 1963. **227**(1): p. 239.

53. Scattergood, R.O. and C.C. Koch, *A modified model for Hall-Petch behavior in nanocrystalline materials.* Scripta Metall. Mater., 1992. **27**(9): p. 1195-1200.

54. Meyers, M.A. and K.K. Chawla, *Mechanical Metallurgy: Principles and Applications* 1984: Prentice-Hall.

55. Thomas, G.J., R.W. Siegel, and J.A. Eastman, *Grain boundaries in nanophase palladium: high resolution electron microscopy and image simulation.* Scripta Metall. Mater., 1990. **24**(1): p. 201-206.

56. Wunderlich, W., Y. Ishida, and R. Maurer, *HREM-studies of the microstructure of nanocrystalline palladium.* Scripta Metall. Mater., 1990. **24**(2): p. 403-408.

57. Rabukhin, V.B., *Influence of triple grain junctions on ductility in the absence of diffusional mobility*. Phys. Met. Metallogr., 1986. **61**(5): p. 149-154.

58. Palumbo, G., U. Erb, and K.T. Aust, *Triple line disclination effects on the mechanical behaviour of materials.* Scripta Metall. Mater., 1990. **24**(12): p. 2347-2350.

59. Suryanarayana, C., et al., *Grain size effects in nanocrystalline materials.* J. Mater. Res., 1992. **7**(8): p. 2114-2118.

60. Masumura, R.A., P.M. Hazzledine, and C.S. Pande, *Yield stress of fine grained materials.* Acta Mater., 1998. **46**(13): p. 4527-4534.

61. Rao, V.K., D.M.R. Taplin, and P.R. Rao, *The grain size dependence of flow and fracture in a Cr-Mn-N austenitic steel from 300 to 1300K.* Metall. Trans. A, 1975. **6**(1): p. 77-86.

62. Van Swygenhoven, H. and A. Caro, *Plastic behavior of nanophase Ni: a molecular dynamics computer simulation.* Appl. Phys. Lett., 1997. **71**(12): p. 1652-1654.

63. Van Swygenhoven, H. and A. Caro, *Plastic behavior of nanophase metals studied by molecular dynamics.* Phys. Rev. B, 1998. **58**(17): p. 11246.

64. Hahn, H. and K.A. Padmanabhan, *A model for the deformation of nanocrystalline materials.* Phil. Mag., 1997. **76**(4): p. 559-571.

65. Takeuchi, S., *The mechanism of the inverse Hall-Petch relation of nanocrystals.* Scripta Mater., 2001. **44**(8): p. 1483-1487.

66. Fan, G.J., H. Choo, and P.K.L. Liaw, E.J., *A model for the inverse Hall–Petch relation of nanocrystalline materials.* Mater. Sci. Eng. A, 2005. **409**: p. 243-248.

67. Morris, D.G. and M.A. Morris, *Microstructure and strength of nanocrystalline copper alloy prepared by mechanical alloying.* Acta Metall. Mater., 1991. **39**(8): p. 1763-1770.

68. Langdon, T.G., *The significance of grain boundaries in the flow of polycrystalline materials.* Mater. Sci. Forum, 1995. **189**: p. 31-42.

69. Carlton, C.E. and P.J. Ferreira, *What is behind the inverse Hall–Petch effect in nanocrystalline materials?* Acta Mater., 2007. **55**: p. 3749-3756.

70. Li, Y.J., X.H. Zeng, and W. Blum, *Transition from strengthening to softening by grain boundaries in ultrafine-grained Cu.* Acta Mater., 2004. **52**(17): p. 5009-5018.

71. Blum, W., et al., *On the Hall–Petch relation between flow stress and grain size.* Int. J. Mater. Res., 2006. **97**(12): p. 1661-1666.

72. Dirikolu, M.H., T.H.C. Childs, and K. Maekawa, *Finite element simulation of chip flow in metal machining.* Int. J. Mech. Sci., 2001. **43**(11): p. 2699-2713.

73. Mamalis, A.G., et al., *Finite element simulation of chip formation in orthogonal metal cutting.* J. Mater. Process. Tech., 2001. **110**(1): p. 19-27.

74. Marusich, T.D. and M. Ortiz, *Modeling and simulation of high-speed machining.* Int. J. Numer. Meth. Eng., 1995. **38**: p. 3675-3694.

75. Shih, A.J., *Finite element simulation of orthogonal metal cutting.* J. Manuf. Sci. Eng., 1995. **117**(1): p. 84-93.

76. Ng, E.G., et al., *Modelling of temperature and forces when orthogonally machining hardened steel.* Int. J. Mach. Tool Manu., 1999. **39**(6): p. 885-903.

77. Childs, T.H.C., *Material property needs in modeling metal machining.* Mach. Sci. Technol., 1998. **2**(2): p. 303-316.

78. Childs, T.H.C. and K. Maekawa, *Computer-aided simulation and experimental studies of chip flow and tool wear in the turning of low alloy steels by cemented carbide tools.* Wear, 1990. **139**(2): p. 235-250.

79. Childs, T.H.C., *Friction modelling in metal cutting.* Wear, 2006. **260**(3): p. 310-318.

80. Childs, T.H.C., K. Maekawa, and P. Maulik, *Effects of coolant on temperature distribution in metal machining.* Mater. Sci. Tech., 1988. **4**(11): p. 1006-1019.

81. Moufki, A., A. Molinari, and D. Dudzinski, *Modelling of orthogonal cutting with a temperature dependent friction law.* J. Mech. Phys. Solids, 1998. **46**(10): p. 2103-2138.

82. Lei, S., Y.C. Shin, and F.P. Incropera, *Thermo-mechanical modeling of orthogonal machining process by finite element analysis.* Int. J. Mach. Tool Manu., 1999. **39**(5): p. 731-750.

83. Lei, S., Y.C. Shin, and F.P. Incropera, *Material constitutive modeling under high strain rates and temperatures through orthogonal machining tests.* J. Manuf. Sci. Eng., 1999. **121**(4): p. 577-585.

84. Shatla, M., C. Kerk, and T. Altan, *Process modeling in machining. Part I: determination of flow stress data.* Int. J. Mach. Tool Manu., 2001. **41**(10): p. 1511-1534.

85. Shatla, M., C. Kerk, and T. Altan, *Process modeling in machining. Part II: validation and applications of the determined flow stress data.* Int. J. Mach. Tool Manu., 2001. **41**(11): p. 1659-1680.

86. Shi, J. and C.R. Liu, *The influence of material models on finite element simulation of machining.* J. Manuf. Sci. Eng., 2004. **126**(4): p. 849-857.

87. Litonski, J., *Plastic flow of a tube under adiabatic torsion.* Bull. Acad. Pol. Sci., 1977. **Ser. Sci. Tech.**(XXV): p. 7.

88. Batra, R.C., *Steady state penetration of thermoviscoplastic targets.* Comp. Mech., 1988. **3**(1): p. 1-12.

89. Bodner, S.R. and Y. Partom, *Constitutive equations for elastic-viscoplastic strain-hardening materials.* J. Appl. Mech., 1975. **42**(2): p. 385-389.

90. Estrin, Y., et al., *A dislocation-based model for all hardening stages in large strain deformation.* Acta Mater., 1998. **46**: p. 5509-5522.

91. Ding, H., N. Shen, and Y.C. Shin, *Modeling of grain refinement in aluminum and copper subjected to cutting.* Comp. Mater. Sci., 2011. **50**: p. 3016-3025.

92. Ding, H. and Y.C. Shin. *Dislocation density-based grain refinement modeling of orthogonal cutting of commercially pure Titanium*. in *Proceedings of the 2011 ASME International Manufacturing Science and Engineering Conference*. 2011. Corvallis, Oregon, USA: MSEC2011-50220.

93. Ding, H. and Y.C. Shin, *Multi-physics modeling and simulations of surface microstructure alteration in hard turning.* J. Mater. Process. Tech., 2013. **213**: p. 877-886.

94. Ding, L., X. Zhang, and C.R. Liu. *Finite element modeling on dislocation density and grain size evolution in machined surface*. in *Proceedings of the 2013 ASME International Manufacturing Science and Engineering Conference*. 2013. Madison, Wisconsin, USA: MSEC2013-1130.

95. Svoboda, A., D. Wedberg, and L.E. Lindgren, *Simulation of metal cutting using a physically based plasticity model.* Model. Simul. Mater. Sci. Eng., 2010. **18**: p. 075005/1-19.

96. Calamaz, M., D. Coupard, and F. Girot, *A new material model for 2D numerical simulation of serrated chip formation when machining titanium alloy Ti–6Al–4V.* Int. J. Mach. Tool Manu., 2008. **48**: p. 275-288.

97. Elmadagli, M. and A.T. Alpas, *Metallographic analysis of the deformation microstructure of copper subjected to orthogonal cutting.* Mater. Sci. Eng. A, 2003. **355**(1-2): p. 249-259.

98. Gente, A., H.W. Hoffmeister, and C.J. Evans, *Chip formation in machining Ti6Al4V at extremely high cutting speeds.* CIRP Annals-Manuf. Tech., 2001. **50**(1): p. 49-52.

99. Komanduri, R. and R.H. Brown, *On the mechanics of chip segmentation in machining.* J. Manuf. Sci. Eng., 1981. **103**(1): p. 33-51.

100. Usui, E., T. Obikawa, and T. Shirakashi. *Study on chip segmentation in machining titanium alloy*. in *Proc. 5th Inter. Conf. Pro. Eng.* . 1984. Tokyo.

101. Cockcroft, M.G. and D.J. Latham, *Ductility and the workability of metals.* J. Inst. Metals, 1968. **96**(1): p. 33-39.

102. Hua, J. and R. Shivpuri, *Prediction of chip morphology and segmentation during the machining of titanium alloys.* J. Mater. Process. Tech., 2004. **150**: p. 124-133.

103. Umbrello, D., R. M'Saoubi, and J.C. Outeiro, *The Influence of Johnson–Cook Material Constants on Finite Element Simulation of Machining of AISI 316L Steel.* Int. J. Mach. Tool Manu., 2007. **47**: p. 462-470.

104. Umbrello, D., *Finite element simulation of conventional and high speed machining of Ti6Al4V alloy.* J. Mater. Process. Tech., 2008. **196**(1): p. 79-87.

105. Ceretti, E., M. Lucchi, and T. Altan, *FEM simulation of orthogonal cutting: serrated chip formation.* J. Mater. Process. Tech., 1999. **95**(1-3): p. 17-26.

106. Johnson, G.R., *Material characterization for computations involving severe dynamic loading.* Proc. Army Symp. on Solid Mechanics, 1980: p. 62-67.

107. Guo, Y.B. and D.W. Yen, *A FEM study on mechanisms of discontinuous chip formation in hard machining.* J. Mater. Process. Tech., 2004. **155-156**: p. 1350-1356.

108. Barge, M., et al., *Numerical modelling of orthogonal cutting: influence of numerical parameters.* J. Mater. Process. Tech., 2005. **164**: p. 1148-1153.

109. Obikawa, T. and E. Usui, *Computational machining of titanium alloy—finite element modeling and a few results.* J. Manuf. Sci. Eng., 1996. **118**: p. 208-215.

110. Liu, R., et al., *An enhanced constitutive material model for machining of Ti–6Al–4V alloy.* J. Mater. Process. Tech., 2013. **213**(12): p. 2238-2246.

111. Chichili, D.R., K.T. Ramesh, and K.J. Hemker, *Adiabatic shear localization in α-titanium: experiments, modeling and microstructural evolution.* J. Mech. Phys. Solids, 2004. **52**(8): p. 1889-1909.

112. Hua, J. and R. Shivpuri, *Prediction of chip morphology and segmentation during the machining of titanium alloys.* J. Mater. Process. Tech., 2004. **150**(1-2): p. 124-133.

113. Calamaz, M., D. Coupard, and F. Girot, *Numerical simulation of titanium alloy dry machining with a strain softening constitutive law.* Mach. Sci. Technol., 2010. **14**: p. 244-257.

114. Calamaz, M., et al., *Numerical analysis of chip formation and shear localisation processes in Machining the Ti-6Al-4V Titanium Alloy.* Int. J. Adv. Manuf. Tech., 2011. **52**: p. 887-895.

115. Sima, M. and T. Özel, *Modified material constitutive models for serrated chip formation simulations and experimental validation in machining of titanium alloy Ti–6Al–4V.* Int. J. Mach. Tool Manu., 2010. **50**: p. 943-960.

116. Krausz, A.S. and K. Krausz, *Unified constitutive laws of plastic deformation*. 1 ed1996: Academic Press.

117. Nes, E. and K. Marthinsen, *Modeling the evolution in microstructure and properties during plastic deformation of fcc-metals and alloys–an approach towards a unified model.* Mater. Sci. Eng. A, 2002. **322**(1): p. 176-193.

118. Holmedal, B., K. Marthinsen, and E. Nes, *A unified microstructural metal plasticity model applied in testing, processing, and forming of aluminium alloys.* Zeitschrift für Metallkunde, 2005. **96**(6): p. 532-545.

119. Varshni, Y.P., *Temperature dependence of the elastic constants.* Phys. Rev. B, 1970. **2**(10): p. 3952-3958.

120. Doherty, R.D., et al., *Current issues in recrystallization: a review.* Mater. Sci. Eng. A, 1997. **238**(2): p. 219-274.

121. Gourdet, S. and F. Montheillet, *A model of continuous dynamic recrystallization.* Acta Mater., 2003. **51**: p. 2685-2699.

122. McQueen, H.J., *Development of dynamic recrystallization theory.* Mater. Sci. Eng. A, 2004. **387-389**: p. 203-208.

123. Kassner, M.E. and S.R. Barrabes, *New developments in geometric dynamic recrystallization.* Mater. Sci. Eng. A, 2005. **410**: p. 152-155.

124. Fu, E.G., et al., *Mechanical properties of sputtered Cu/V and Al/Nb multilayer films.* Mater. Sci. Eng. A, 2008. **493**(1-2): p. 283-287.

125. Di Schino, A. and J.M. Kenny, *Grain size dependence of the fatigue behaviour of a ultrafine-grained AISI 304 stainless steel.* Mater. Lett., 2003. **57**(21): p. 3182-3185.

126. Ryan, N.D. and H.J. McQueen, *Dynamic softening mechanisms in 304 austenitic stainless steel.* Can. Metall. Quart., 1990. **29**(2): p. 147-162.

127. Byun, T.S., N. Hashimoto, and K. Farrell, *Temperature dependence of strain hardening and plastic instability behaviors in austenitic stainless steels.* Acta Mater., 2004. **52**(13): p. 3889-3899.

128. Kocks, U.F., A.S. Argon, and M.F. Ashby, *Thermodynamics and kinetics of slip.* Prog. Mater. Sci., 1975. **19**: p. 139-143.

129. Kapoor, R. and S. Nemat-Nasser, *Comparison between high and low strain-rate deformation of tantalum.* Metall. Mater. Trans. A 2000. **31**(13): p. 815-823.

130. Tanner, A.B. and D.L. McDowell, *Deformation, temperature and strain rate sequence experiments on OFHC Cu.* Int. J. Plasticity, 1999. **15**: p. 375-399.

131. Kitajima, S., M. Ohta, and H. Tonda, *Production of highly perfect copper crystals with thermal cyclic annealing.* J. Cryst. Growth, 1974. **24-25**: p. 521-526.

132. Follansbee, P.S. and G.T. Gray, III, *Dynamic deformation of shock prestrained copper.* Mater. Sci. Eng. A, 1991. **138**: p. 23-31.

133. Hou, X.D., A.J. Bushby, and N.M. Jennett, *Study of the interaction between the indentation size effect and Hall-Petch effect with spherical indenters on annealed polycrystalline copper.* J. Phys. D: Appl. Phys., 2008. **41**: p. 074006/1-7.

134. Smith, W. and J. Hashemi, *Foundations of Materials Science and Engineering*. 4 ed2006: McGraw-Hill.

135. Kim, Y., et al., *Characterization of hot deformation behaviors of wrought and P/M oxygen free Coppers (OFCs) using processing maps.* Mater. Sci. Eng. A, 2012. **552**: p. 276-282.

136. Blaz, L., T. Sakai, and J.J. Jonas, *Effect of initial grain size on dynamic recrystallization of copper.* Metal Sci., 1983. **17**: p. 609-616.

137. Brown, T.L., et al., *A study of the interactive effects of strain, strain rate and temperature in severe plastic deformation of copper.* Acta Mater., 2009. **57**: p. 5491-5500.

138. Chandrasekar, S. and C. Saldana, *unpublished data*.

139. Lampman, S., *ASM Handbook*1990: ASM International.

140. Touloukian, Y.S., *Thermophysical Properties of Matter, TPRC data series*1970, New York.

141. Lide, D.R., *Handbook of Chemistry and Physics*2010: CRC Press.

142. Brown, T.L., et al., *Low-cost manufacturing process for nanostructured metals and alloys.* J. Mater. Res., 2002. **17**(10): p. 2484-2488.

143. Lee, S., et al., *Large strain deformation field in machining.* Metall. Mater. Trans. A, 2005. **37**(5): p. 1633-1643.

144. Ni, H. and A.T. Alpas, *Sub-micrometer structures generated during dry machining of copper.* Mater. Sci. Eng. A, 2003. **361**: p. 338-349.

145. Swaminathan, S., et al., *Large strain deformation and ultra-fine grained materials by machining.* Mater. Sci. Eng. A, 2005. **410-411**: p. 358-363.

146. Merchant, M.E., *Mechanics of the metal cutting process. I. orthogonal cutting and a type 2 chip.* J. Appl. Phys., 1945. **16**: p. 267-275.

147. Sheikh-Ahmad, J. and J.A. Bailey, *Flow instability in the orthogonal machining of CP titanium.* J. Manuf. Sci. Eng., 1997. **119**(3): p. 307-313.

148. Nemat-Nasser, S., W.G. Guo, and J.Y. Cheng, *Mechanical properties and deformation mechanisms of a commercially pure titanium.* Acta Mater., 1999. **47**(13): p. 3705-3720.

149. *Aerospace structural metals handbook*1963, Traverse City, Mich.: Proterties Data Center.

150. Fisher, E.S. and C.J. Renken, *Physical Review*. Vol. 135. 1964.

151. Zeng, Z., S. Jonsson, and H.J. Roven, *The effects of deformation conditions on microstructure and texture of commercially pure Ti.* Acta Mater., 2009. **57**(19): p. 5822-5833.

152. Frost, H.J. and M.F. Ashby, *Deformation mechanism maps*1982, Oxford: Pergamon Press.

153. Luo, P., et al., *Recycling of titanium machining chips by severe plastic deformation consolidation.* J. Mater. Sci., 2010. **45**(17): p. 4606-4612.

154. Moskalenko, V.A. and A.R. Smirnov, *Temperature effect on formation of reorientation bands in α-Ti.* Mater. Sci. Eng. A, 1998. **246**(1-2): p. 282-288.

155. Zhao, X., et al., *Microstructure and properties of pure titanium processed by equal-channel angular pressing at room temperature.* Scripta Mater., 2008. **59**(5): p. 542-545.

156. Stolyarov, V.V., et al., *Grain refinement and properties of pure Ti processed by warm ECAP and cold rolling.* Mater. Sci. Eng. A, 2003. **343**(1): p. 43-50.

157. Ding, R. and Z.X. Guo, *Microstructural evolution of a Ti–6Al–4V alloy during β-phase processing: experimental and simulative investigations.* Mater. Sci. Eng. A, 2004. **365**(1-2): p. 172-179.

158. Ashby, M.F. and D.R. Jones, *Engineering Materials 2, Third Edition: An Introduction to Microstructures, Processing and Design*2005: Butterworth-Heinemann.

159. Zeng, Z., S. Jonsson, and Y. Zhang, *Constitutive equations for pure titanium at elevated temperatures.* Mater. Sci. Eng. A, 2009. **505**: p. 116-119.

160. Wulf, G.L., *High strain rate compression of titanium and some titanium alloys.* Int. J. Mech. Sci., 1979. **21**(12): p. 713-718.

161. Welsch, G., R. Boyer, and E.W. Collings, *Materials Properties Handbook: Titanium Alloys*1993: ASM International.

162. Lepkowski, W.J. and J.W. Holladay, *TML Report No. 73*1957.

163. *Thermophysical Properties of Solid Materials, Vol 1-Elements, WADC Technical Report 58-747*1960: Wright Air Development Division.

164. Turley, D.M. and E.D. Doyle, *Calculation of shear strains in chip formation in titanium.* Mater. Sci. Eng., 1982. **55**(1): p. 45-48.

165. Meyers, M.A., U.R. Andrade, and A.H. Chokshi, *The effect of grain size on the high-strain, high-strain-rate behavior of copper.* Metall. Mater. Trans. A, 1995. **26**(11): p. 2881-2893.

166. Joseph, V.R. and H. Yan, *Engineering-driven statistical adjustment and calibration.* Technometrics, 2014: p. to be published.

167. Goddard, W.A., et al., *Handbook of Nanoscience, Engineering, and Technology*. Third ed2008: CRC Press.

VITA

RUI LIU

LIU was born in Tianjin, China. He received a B.A. in Jet Propulsion from Beijing University of Aeronautics & Astronautics (BUAA), Bejing, China in 2005 and a M.A. in Mechanical Engineering from Northeastern University, Boston, Massachusetts in 2010 before coming to Georgia Tech to pursue a doctorate in Mechanical Engineering.